

2012

NMR study of paramagnetic nano-checkerboard superlattices

Christopher Andrew Maher
College of William & Mary - Arts & Sciences

Follow this and additional works at: <https://scholarworks.wm.edu/etd>

Recommended Citation

Maher, Christopher Andrew, "NMR study of paramagnetic nano-checkerboard superlattices" (2012).
Dissertations, Theses, and Masters Projects. Paper 1539623592.
<https://dx.doi.org/doi:10.21220/s2-fhpw-qh95>

This Dissertation is brought to you for free and open access by the Theses, Dissertations, & Master Projects at W&M ScholarWorks. It has been accepted for inclusion in Dissertations, Theses, and Masters Projects by an authorized administrator of W&M ScholarWorks. For more information, please contact scholarworks@wm.edu.

**NMR STUDY OF PARAMAGNETIC NANO-CHECKERBOARD
SUPERLATTICES**

Christopher Andrew Maher

Portsmouth, New Hampshire

Master of Science, College of William and Mary, 2006
Bachelor of Science, University of New Hampshire, Durham NH, 2005

A Dissertation presented to the Graduate Faculty
of the College of William and Mary in Candidacy for the Degree of
Doctor of Philosophy

Department of Physics

The College of William and Mary
January 2012

©2011
Christopher Andrew Maher
All rights reserved.

APPROVAL PAGE

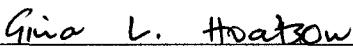
This Dissertation is submitted in partial fulfillment of
the requirements for the degree of

Doctor of Philosophy




Christopher Andrew Maher

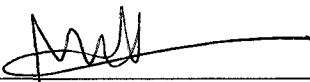
Approved by the Committee, October, 2011



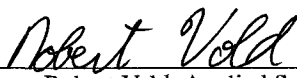
Committee Chair
Professor Gina Hoatson, Physics
The College of William and Mary



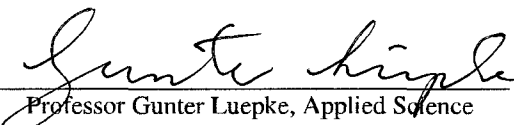
Professor Henry Krakauer, Physics
The College of William and Mary



Assistant Professor Mumtaz Qazilbash, Physics
The College of William and Mary



Professor Robert Vold, Applied Science
The College of William and Mary



Professor Gunter Luepke, Applied Science
The College of William & Mary

ABSTRACT PAGE

With the ubiquity of electronic devices, finding ways to improve quality or fabrication methods of components is an important area of study. This dissertation looks at two sets of materials that may be used to address this need. The first is a series of disordered perovskites of the form $\text{Nd}_{\frac{2}{3}-x}\text{Li}_{3x}\text{TiO}_3$. These materials are notable for the way the lithium becomes spontaneously patterned during synthesis into square planar regions, the dimensions of which are only dependent upon the initial concentration of lithium. Through the use of point-charge calculations, the paramagnetic and first-order quadrupole interaction tensors for each of the 28 unique lithium sites of the $x = 0.083$ concentration were calculated and used to accurately simulate the experimental spectra. From this, it was observed that the 28 crystallographically distinct sites present in that particular concentration could be grouped into three sets based on the principal values of the paramagnetic interaction tensors. Qualitative analysis of spectra from the other concentrations suggests that this grouping holds for other concentrations, with only the relative number of sites in each group changing. Additionally, jump dynamics were incorporated into the simulations of one of the sites in order to explain the broadening that occurs at lower temperatures.

The second study included in this dissertation is focused on lithium in a pair of high-dielectric microwave ceramics, $\text{Ca}(\text{Li}_{1/3}\text{Nb}_{2/3})\text{O}_3$ and $(\text{Ca}_{2/3}\text{La}_{1/3})(\text{Li}_{1/3}\text{Nb}_{2/3})\text{O}_3$. Experimental results are reported for the temperature-dependence of both the spin-lattice relaxation rate and the isotropic chemical shift for each material. For both samples, the isotropic shift was linear with temperature, with the isotropic shift of $\text{Ca}(\text{Li}_{1/3}\text{Nb}_{2/3})\text{O}_3$ having a stronger temperature dependence ($3.53 \text{ Hz} \cdot \text{K}^{-1}$ compared to $2.65 \text{ Hz} \cdot \text{K}^{-1}$). The spin-lattice relaxation rates of both samples follow an Arrhenius relationship with temperature, with $\text{Ca}(\text{Li}_{1/3}\text{Nb}_{2/3})\text{O}_3$ having an activation energy of $5.08 \text{ kJ} \cdot (\text{mol} \cdot \text{K})^{-1}$ and $(\text{Ca}_{2/3}\text{La}_{1/3})(\text{Li}_{1/3}\text{Nb}_{2/3})\text{O}_3$ having an activation energy of $2.21 \text{ kJ} \cdot (\text{mol} \cdot \text{K})^{-1}$. In addition to the lithium study, there were also spectra acquired that observed the niobium nucleus in each material, which has a noticeably more complex spectrum. For the $(\text{Ca}_{2/3}\text{La}_{1/3})(\text{Li}_{1/3}\text{Nb}_{2/3})\text{O}_3$ sample, a double-quantum satellite-transition magic angle spinning pulse sequence was used to determine the isotropic chemical shift as well as the quadrupole product of each of the five resolved sites.

TABLE OF CONTENTS

	Page
Acknowledgments	iv
List of Tables	v
List of Figures	vii
CHAPTER	
1 Introduction	2
2 Nuclear Magnetic Resonance Spectroscopy	7
2.1 The Zeeman Interaction	7
2.2 Free Precession and Relaxation	10
2.2.1 Free Precession	10
2.2.2 Spin-Lattice and Spin-Spin Relaxation	12
2.2.3 The Density Matrix	14
2.3 Magic Angle Spinning	15
2.4 NMR Tensor Interactions	22
2.4.1 The Chemical Shielding Interaction	22
2.4.2 The Paramagnetic Interaction	25
2.4.3 The Quadrupole Interaction	29
3 Experimental Methods	32
3.1 Experimental Equipment Overview	32
3.2 Pulse Sequences	39

3.2.1	Zero-Go Pulse Sequence	39
3.2.2	Hahn-Echo Pulse Sequence	41
3.2.3	T_{1z} Saturation-Recovery Pulse Sequence	43
3.3	Signal Processing	44
4	A Study of Complex Paramagnetic Oxides: $\text{Nd}_{\frac{2}{3}-x}\text{Li}_{3x}\text{TiO}_3$	49
4.1	An Overview of $\text{Nd}_{\frac{2}{3}-x}\text{Li}_{3x}\text{TiO}_3$	49
4.2	Summary of Experiments	53
4.3	Qualitative Results	55
4.4	Simulating the NMR Spectra	60
4.5	Fitting the Simulations to Experiment	68
4.6	Quantitative Results of $x=0.083$	73
4.7	Lithium Dynamics in $\text{Nd}_{\frac{2}{3}-x}\text{Li}_{3x}\text{TiO}_3$	79
4.8	Conclusion	87
5	Study of High-Dielectric Microwave Ceramics	89
5.1	Overview of High-Dielectric Microwave Ceramics	89
5.2	Summary of Experiments	90
5.3	Results and Interpretation	92
5.3.1	Analysis of the Isotropic Shift and T_{1z} Relaxation of ^7Li	92
5.3.2	Analysis of ^{93}Nb Results	98
5.4	Conclusion	101
6	Conclusion	103
APPENDIX A		
	Point Charge EFG Calculations of Lithium Niobate	106
APPENDIX B		
	Temperature Calibration Using Lead Nitrate	113
APPENDIX C		
	$\text{Nd}_{.58}\text{Li}_{.25}\text{TiO}_3$ Interaction Tensors	118

APPENDIX D

Matlab Source Code	124
D.1 Simulation of Paramagnetic & Quadrupolar FID for Spin-3/2 Nucleus	124
D.2 Calculation of EFG at a Site Due to One Nucleus	128
D.3 Calculation of Complete EFG Tensor	130
D.4 Calculation of Paramagnetic Tensor Due to a Single Nucleus	132
Bibliography	134
Vita	138

ACKNOWLEDGMENTS

I would first like to express my gratitude to my advisors, Professors Gina Hoatson and Robert Vold, for their patience, guidance, and instruction over the years. They both helped to make seemingly impossible projects manageable. I would also like to thank the other members of my dissertation committee for taking the time to read and critique this thesis. The other students who have passed through the lab over the years have been crucial in helping me to understand the intricacies of successfully performing NMR experiments as well as helping me to learn more than I ever thought there was to know about equipment maintenance. Specifically, I would like to thank Murugesan Vijayakumar and Yuanyuan Huang for their guidance early on and for showing me how instruction manuals and specs are best taken as suggestions.

Much of the work discussed in this thesis would not be possible without the cooperation of individuals outside the lab. The materials studied were provided by the group led by Peter Davies at the University of Pennsylvania, with much of the structural information of the paramagnetic materials provided by Beth Guiton. I would also like to thank Eric Walter for taking the time to perform the DFT calculations used to help determine the validity of my point-charge calculations.

I would like to thank all of the friends I've met throughout my time in graduate school for making school about more than just physics. Whether gathering for weekly TV viewing parties or spending innumerable hours discussing the intricacies of fantasy sports, the fun times spent away from physics helped to make the time spent on physics that much more productive.

Last but not least, I would like to thank my family for the years of support they have given me. It's allowed me to get where I am today.

LIST OF TABLES

Table	Page
4.1 ^7Li tensor components of $\text{Nd}_{.58}\text{Li}_{.25}\text{TiO}_3$	74
4.2 Parameters for paramagnetic tensors of displaced ^7Li in $\text{Nd}_{\frac{2}{3}-x}\text{Li}_{3x}\text{TiO}_3$.	84
4.3 Parameters for quadrupole tensors of displaced ^7Li in $\text{Nd}_{\frac{2}{3}-x}\text{Li}_{3x}\text{TiO}_3$. .	84
4.4 Parameters for a heuristic model of tensor interactions in a distorted perovskite lattice	85
5.1 DQ-STMAS results of ^{93}Nb in $(\text{Ca}_{2/3}\text{La}_{1/3})(\text{Li}_{1/3}\text{Nb}_{2/3})\text{O}_3$	101
A.1 Paraelectric LiNbO_3 unit cell positions	107
A.2 Ferroelectric LiNbO_3 unit cell positions	109
A.3 EFG tensor components of atom sites in paraelectric LiNbO_3	111
A.4 EFG tensor components of atom sites in ferroelectric LiNbO_3	111
B.1 Temperature calibration for MAS experiments	116
C.1 ^7Li tensors of $\text{Nd}_{.58}\text{Li}_{.25}\text{TiO}_3$ (Sites 1-10)	119
C.2 ^7Li tensors of $\text{Nd}_{.58}\text{Li}_{.25}\text{TiO}_3$ (Sites 11-20)	120
C.3 ^7Li tensors of $\text{Nd}_{.58}\text{Li}_{.25}\text{TiO}_3$ (Sites 21-28)	121
C.4 Displaced ^7Li quadrupole principal values of $\text{Nd}_{.58}\text{Li}_{.25}\text{TiO}_3$	122

C.5	Displaced ${}^7\text{Li}$ quadrupole principal values of $\text{Nd}_{.58}\text{Li}_{.25}\text{TiO}_3$	123
-----	---	-----

LIST OF FIGURES

Figure	Page
2.1 Energy level diagram of a nuclear spin in a magnetic field	8
2.2 Evolution of a nuclear spin during an NMR experiment	11
2.3 Static and MAS spectra of PbNO_3	16
2.4 Diagram of a Magic Angle Spinning experiment	17
3.1 NMR spectrometer receiver circuit overview	34
3.2 Photograph of 2.5 mm MAS probe and rotor	37
3.3 MAS stator cross-section	38
3.4 Pulse sequence diagram of a ZG (Zero-Go) experiment	41
3.5 Pulse sequence diagram of a Hahn-Echo experiment	42
3.6 Spin evolution during an echo experiment	43
3.7 Pulse sequence diagram of a T_{1z} Saturation-Recovery experiment	44
3.8 ^2H NMR experiment of D_2O	47
4.1 Perovskite crystal structure	50
4.2 $\text{Nd}_{.58}\text{Li}_{.25}\text{TiO}_3$ structure	51
4.3 TEM images of $\text{Nd}_{\frac{2}{3}-x}\text{Li}_{3x}\text{TiO}_3$	52
4.4 Pulse coverage determination using aqueous LiCl	54

4.5	^7Li spectra of $\text{Nd}_{\frac{2}{3}-x}\text{Li}_{3x}\text{TiO}_3$	56
4.6	EPR spectrum of $\text{Nd}_{58}\text{Li}_{25}\text{TiO}_3$ at 70 K	58
4.7	Magnetic susceptibility measurements of $\text{Nd}_{\frac{2}{3}-x}\text{Li}_{3x}\text{TiO}_3$	58
4.8	M vs H loop of $\text{Nd}_{\frac{2}{3}-x}\text{Li}_{3x}\text{TiO}_3$	59
4.9	^6Li fit of $\text{Nd}_{58}\text{Li}_{25}\text{TiO}_3$ at T= 320 K	71
4.10	^7Li fit of $\text{Nd}_{58}\text{Li}_{25}\text{TiO}_3$ at T= 331 K	71
4.11	^7Li fit of $\text{Nd}_{58}\text{Li}_{25}\text{TiO}_3$ at T= 277 K	72
4.12	^7Li fit of $\text{Nd}_{58}\text{Li}_{25}\text{TiO}_3$ at T= 360 K	72
4.13	Labels for lithium sites in $\text{Nd}_{58}\text{Li}_{25}\text{TiO}_3$	73
4.14	$\text{Nd}_{58}\text{Li}_{25}\text{TiO}_3$ site assignments	75
4.15	Temperature dependence of $\text{Nd}_{58}\text{Li}_{25}\text{TiO}_3$ anisotropy	76
4.16	Temperature dependence of $\text{Nd}_{58}\text{Li}_{25}\text{TiO}_3$ isotropic shift	76
4.17	Temperature dependence of P_{zz} in $\text{Nd}_{58}\text{Li}_{25}\text{TiO}_3$	77
4.18	Temperature dependence of P_{yy} in $\text{Nd}_{58}\text{Li}_{25}\text{TiO}_3$	77
4.19	Temperature dependence of P_{xx} in $\text{Nd}_{58}\text{Li}_{25}\text{TiO}_3$	78
4.20	Dynamics simulation of single site in $\text{Nd}_{58}\text{Li}_{25}\text{TiO}_3$	82
4.21	Dynamics simulation of single site in $\text{Nd}_{\frac{2}{3}-x}\text{Li}_{3x}\text{TiO}_3$ with small-angle jumps	86
5.1	T_{1z} recovery curve from saturation-recovery sequence	91
5.2	$\text{Ca}(\text{Li}_{1/3}\text{Nb}_{2/3})\text{O}_3$ ^7Li MAS spectrum	93
5.3	Center peak of $\text{Ca}(\text{Li}_{1/3}\text{Nb}_{2/3})\text{O}_3$ ^7Li MAS spectrum	93
5.4	$(\text{Ca}_{2/3}\text{La}_{1/3})(\text{Li}_{1/3}\text{Nb}_{2/3})\text{O}_3$ ^7Li MAS spectrum	94
5.5	Center peak of $(\text{Ca}_{2/3}\text{La}_{1/3})(\text{Li}_{1/3}\text{Nb}_{2/3})\text{O}_3$ ^7Li MAS spectrum	94
5.6	$\text{Ca}(\text{Li}_{1/3}\text{Nb}_{2/3})\text{O}_3$ isotropic shift	95

5.7	$\text{Ca}(\text{Li}_{1/3}\text{Nb}_{2/3})\text{O}_3$ relaxation rate	95
5.8	$(\text{Ca}_{2/3}\text{La}_{1/3})(\text{Li}_{1/3}\text{Nb}_{2/3})\text{O}_3$ isotropic shift	96
5.9	$(\text{Ca}_{2/3}\text{La}_{1/3})(\text{Li}_{1/3}\text{Nb}_{2/3})\text{O}_3$ relaxation rate	97
5.10	$\text{Ca}(\text{Li}_{1/3}\text{Nb}_{2/3})\text{O}_3$ ^{93}Nb MAS spectrum	98
5.11	$(\text{Ca}_{2/3}\text{La}_{1/3})(\text{Li}_{1/3}\text{Nb}_{2/3})\text{O}_3$ ^{93}Nb MAS spectrum	99
5.12	^{93}Nb Double-Quantum STMAS spectrum of $(\text{Ca}_{2/3}\text{La}_{1/3})(\text{Li}_{1/3}\text{Nb}_{2/3})\text{O}_3$	100
5.13	^{93}Nb Double-Quantum STMAS slices of $(\text{Ca}_{2/3}\text{La}_{1/3})(\text{Li}_{1/3}\text{Nb}_{2/3})\text{O}_3$. .	100
A.1	Paraelectric LiNbO_3 structure	107
A.2	Paraelectric LiNbO_3 basis vectors	108
A.3	Ferroelectric LiNbO_3 structure	109
A.4	Ferroelectric LiNbO_3 basis vectors	110
B.1	Stearic acid melting point spectra	115
B.2	Temperature calibration for 2.5 mm MAS probe	117
B.3	Temperature calibration for 4 mm MAS probe	117

NMR STUDY OF PARAMAGNETIC NANO-CHECKERBOARD SUPERLATTICES

CHAPTER 1

Introduction

Determining the small-scale structure of materials is often a crucial step in understanding their properties. When effects such as electronic properties (conductivity, dielectric constant, etc.) or physical properties (strength, malleability, etc.) can be correlated with composition and structure, it becomes possible to design better materials to obtain the desired results. Many methods are available for studying these structures: electron microscopy, X-ray or neutron diffraction, and mass spectroscopy, to name a few.

Nuclear Magnetic Resonance (NMR) spectroscopy is yet another technique available for studying the structure and properties of materials. With its high degree of sensitivity to the local structure surrounding the nuclei, it complements other techniques by providing information on the local structure, as well as the dynamics, of the material. The resulting NMR spectra can provide direct information about the interactions of the nuclei being observed, such as the number of unique sites or the values of interaction tensor components (such as the quadrupole coupling constant).

When the interactions affecting the observed nuclei are well understood, further information can be obtained by attempting to simulate the experimental spectra. Least-squares fitting routines can result in highly accurate simulations that can provide precise

values for not only the interaction tensor components but also information on the dynamics of the system, such as nuclei jumping between possible displacements, or even jumping from site to site in the case of conductive materials.

This dissertation will discuss a pair of studies that focus on materials of particular importance to the production and performance of electronic devices. Both sets of experiments observe the lithium nuclei present in disordered perovskites, but with very different neighboring atoms. The first set of materials, with the structure $\text{Nd}_{\frac{2}{3}-x}\text{Li}_{3x}\text{TiO}_3$, contains strongly paramagnetic neodymium, which produces the largest effects on the lithium atoms in the material. These materials are notable for the way in which the lithium spontaneously orders into square planar regions, forming a checkerboard-like bulk structure, whose nano-scale dimensions are directly related to the bulk lithium concentration [1, 2]. It is this ordering that makes the materials potentially useful in the electronic nano-fabrication process. Being able to finely adjust the nano-scale structure of the material allows it to be used as a template material for applications such as creating very small-scale electronic circuits.

The microwave ceramics discussed in Chapter 5 have a more uniform distribution of atoms, and are more interesting for their electronic properties. The two materials studied here, $\text{Ca}(\text{Li}_{1/3}\text{Nb}_{2/3})\text{O}_3$ and $(\text{Ca}_{2/3}\text{La}_{1/3})(\text{Li}_{1/3}\text{Nb}_{2/3})\text{O}_3$, are a subset of a series of materials produced by Peter Davies of the University of Pennsylvania [3–5]. These microwave ceramics have high dielectric constants and are low-loss. This makes them most useful in applications such as frequency filters and oscillators. In this case, NMR can be useful in determining how well the materials respond to temperature changes.

Immediately following this introduction, Chapter 2 will cover the NMR theory necessary to understand the interactions that are relevant to the work described in later chapters. This begins with a basic overview of what NMR experiments are actually seeing, describing the Zeeman interaction that is present in all NMR experiments. The technique of magic angle spinning (MAS) will also be detailed, explaining both why it works

and what advantages it provides, as well as explaining the presence of spinning sidebands. The last section of Chapter 2 will cover each of the interactions that play a role in the projects covered in later chapters. This includes the chemical shielding interaction, quadrupole coupling, and the paramagnetic interaction. The physical mechanisms that produce these interactions, as well as the mathematics of how they actually manifest in the NMR spectrum, will be discussed.

Chapter 3 will focus on the experimental setup common to both projects and used by most solid state NMR experiments in general. This begins with an overview of the magnet and spectrometer system, detailing what components were used and briefly describing how they operate. After this is an overview of how the NMR signal generated by a sample is processed by the receiver circuit in order to obtain the final signal that is recorded by the computer workstation. Following this are detailed descriptions of the specific pulse sequences used, namely the Zero-Go, Hahn-Echo, and T_{1z} Saturation-Recovery sequences. Each of these has specific uses, as well as inherent advantages and disadvantages which will be discussed in detail.

The first of the two major projects will be discussed in Chapter 4. This study focuses on lithium in a series of materials with the structure $\text{Nd}_{\frac{2}{3}-x}\text{Li}_{3x}\text{TiO}_3$. As previously mentioned, these materials have a perovskite crystal structure, but what makes them so interesting is that the lithium spontaneously isolates itself into nanometer-dimension square regions in the material during synthesis. The project itself studied both the temperature- and lithium concentration-dependence of the NMR MAS spectra. A total of four different samples were studied, each with a different concentration of lithium, defined by x in the stoichiometry. Additionally, the spectra of the $x=0.083$ sample were interpreted by comparing them to simulations that were calculated through the use of a point-charge approximation that determined the paramagnetic and quadrupolar interaction tensors based on crystal data obtained by previous studies [1, 2].

The second project, detailed in Chapter 5, is the study of the two high-dielectric

perovskites, $\text{Ca}(\text{Li}_{1/3}\text{Nb}_{2/3})\text{O}_3$ and $(\text{Ca}_{2/3}\text{La}_{1/3})(\text{Li}_{1/3}\text{Nb}_{2/3})\text{O}_3$. The majority of the experiments focused on the lithium nucleus, examining the temperature dependence of the $T_{1\rho}$ relaxation rate as well as the isotropic chemical shift. In addition, several experiments were performed observing the niobium nucleus, which features noticeably more complicated spectra. For the $(\text{Ca}_{2/3}\text{La}_{1/3})(\text{Li}_{1/3}\text{Nb}_{2/3})\text{O}_3$ material, a double-quantum satellite-transition magic angle spinning (STMAS) experiment was used in order to extract the values of the isotropic chemical shift and the quadrupole product for each of the sites.

At the end of the main body of the dissertation are several appendices. Appendix A discusses the point-charge approximation used to calculate the quadrupole interaction in Chapter 4. This discussion focuses on the accuracy of the calculations by looking at a much simpler pair of materials, two different forms of lithium niobate (LiNbO_3). The quadrupole tensor components are calculated using a point-charge approximation as well as several density functional theory (DFT) methods. The results are then compared against one another in order to determine the usefulness of the point-charge model.

The second appendix details the process of using lead nitrate [$\text{Pb}(\text{NO}_3)_2$] in order to calibrate the sample temperature used for the other experiments. Lead nitrate is known to have a very strong and very consistent temperature-dependent isotropic chemical shift [6, 7]. This allows it to be used to calibrate the true sample temperature when placed under identical conditions. This calibration is crucial to the temperature-dependent studies performed in Chapters 4 and 5 since the process of magic angle spinning can result in frictional heating of the sample, up to 30 K above the target temperature.

Appendix C contains the values for the interaction tensors resulting from point-charge calculations of ^7Li in the $\text{Nd}_{\frac{2}{3}-x}\text{Li}_{3x}\text{TiO}_3$ materials under different conditions. The first set of tables shows the full interaction tensors for each of the 28 lithium sites as they are located in the proposed crystal structure of the $x = 0.083$ sample. The remaining tables list the principal values of the quadrupole tensor of each site when shifted by

various displacements.

Appendix D includes some of the MatlabTM code that was written for the purpose of simulating the lithium spectra of the $\text{Nd}_{\frac{2}{3}-x}\text{Li}_{3x}\text{TiO}_3$ samples discussed in Chapter 4. This includes the calculation of the paramagnetic and quadrupolar interaction tensors based on known atom positions, as well as the actual simulation of the NMR line shape using these tensors. The simulation itself was developed as a module for the EXPRESS software developed by Professors Robert Vold and Gina Hoatson [8], in order to take advantage of already existing front-end and processing routines.

CHAPTER 2

Nuclear Magnetic Resonance

Spectroscopy

This chapter will give an overview of nuclear magnetic resonance (NMR) spectroscopy: what is observed and the physical origin of the phenomenon. The discussion includes the relevant interactions that determine how NMR-active nuclei respond to external conditions during experiments- specifically, the chemical shielding, paramagnetic, and quadrupolar interactions. In addition, the technique of magic angle spinning will also be described, explaining how it leads to spectra in which major sources of inhomogeneous line broadening are greatly reduced and why it is essential to perform MAS in solid materials.

2.1 The Zeeman Interaction

Nuclear magnetic resonance is the process of manipulating the spins of the nuclei in a sample and observing the resulting evolution of the system as the spins precess and relax back to their thermal equilibrium state. First, the sample (with nuclear spin I) is

placed in a strong static magnetic field, B_0 . This static field causes the magnetization in the sample, defined as

$$\mu = \gamma \hbar I, \quad (2.1)$$

to align along the direction of the B_0 field in proportion to the nucleus' gyromagnetic ratio (γ), resulting in the Hamiltonian,

$$\hat{H} = -\hat{\mu} \cdot \mathbf{B}_0 = -\gamma \hbar \hat{I}_z B_0. \quad (2.2)$$

The direction of the static field is used to define the z -axis in the lab frame of reference. In the presence of the magnetic field, previously degenerate spin-states are now separated in energy and level according to their component quantum numbers (m) relative to B_0 according to

$$E_{I,m} = -\gamma \hbar B_0 m = h\nu_0. \quad (2.3)$$

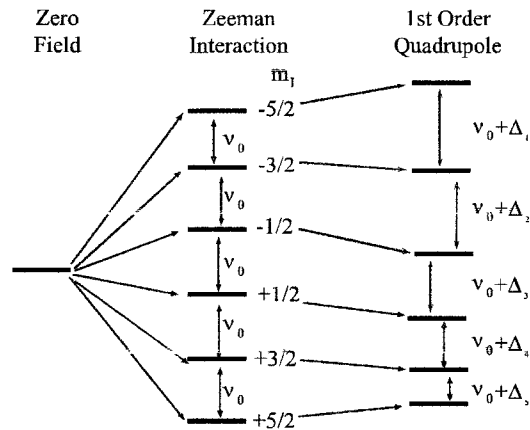


FIG. 2.1: Energy level diagram of a spin-5/2 nucleus in a magnetic field with a first-order quadrupole interaction included in addition to the basic Zeeman interaction. Δ_i represents the different shifts for each energy level. Not drawn to scale.

The total number of available energy levels is equal to $(2I + 1)$. With the energy

levels separated in this manner, the total number of quantum mechanically allowed transitions, $\Delta m = \pm 1$, is $2I$. The splitting of energy levels due to the magnetic field is referred to as the Zeeman interaction, and is usually the largest contribution of the energy level shifts that results in the transition frequencies observed during an NMR experiment. In general, it is several orders of magnitude stronger than any local interactions in the vicinity of the nucleus. In a 17.6 T field for instance, the transition frequency due to the static field is on the order of hundreds of MHz (750 MHz for protons), while dipolar, paramagnetic, and quadrupolar interactions are on the order of tens to hundreds of kHz.

While the spins aligned parallel with the static field will have the lowest energy, the total populations of energy levels $[p(E_i)]$ follow a normal Boltzmann distribution, as shown by [9]

$$p(E_i) = \frac{e^{-E_i/kT}}{\sum_j e^{-E_j/kT}}, \quad (2.4)$$

where k is the Boltzmann constant. There are two ways to think about this distribution. One is as a number of individual spins, with each in one of the available spin states. This is essentially a classical interpretation and is easy to visualize. Another view is to take a quantum mechanical approach, considering each individual spin to exist in a linear combination of Zeeman states, such that at thermal equilibrium the ensemble average expectation value of the any observable property matches the result predicted by an appropriate Boltzmann average.

The frequency of the transition between energy levels is dependent upon the static field and is given as

$$\nu_0 = \frac{\gamma B_0}{2\pi}. \quad (2.5)$$

This frequency is referred to as the Larmor frequency, and in the absence of any other

fields or interactions, the transitions between any two adjacent energy levels will have exactly the same frequencies. It is only through perturbations (other interactions) that the different transitions become distinguishable in the NMR spectra.

These perturbations are a result of interactions with other nuclei and electrons. Some of these interactions (e.g. chemical shielding, paramagnetic, and quadrupole effects) will be discussed in detail in subsequent sections of this chapter. Figure 2.1 shows how the energy levels can be shifted due to these types of perturbations. With these perturbations taken into account, the different energy level transitions will be shifted by differing amounts, leading to the transition frequencies between adjacent energy levels no longer being equal. These differences in transition frequency allow for various NMR experiments to manipulate the energy level distribution of the system depending on what interaction is being studied. A series of radio frequency (rf) pulses, applied transverse to B_0 , at the resonance frequency can be used to manipulate the spins. This is the basis of all NMR experiments. Pulse sequences can be designed to enhance the populations of particular energy levels in order to increase the observed signal to noise, or to eliminate those transitions from appearing in order to better isolate some portion of the spectrum [10, 11]. The nature of several relevant pulse sequences, as well as how the NMR signal is actually recorded, will be detailed in the experimental methods chapter.

2.2 Free Precession and Relaxation

2.2.1 Free Precession

A simple classical picture of the evolution of a single spin as a result of a single transverse rf pulse in a strong static field is shown in Figure 2.2. The spin is initially aligned with the B_0 field, defined here as the z -axis. An rf pulse, with a frequency close to the Larmor frequency of the nucleus, is applied along the $-x$ -axis.

The rf pulse causes the spin to precess away from the z -axis and towards the y -axis. In the case of a 90° pulse commonly used in NMR, the pulse is turned off once the spin is aligned along the y -axis. In the absence of rf pulses, the only field acting on the nucleus is the static field, B_0 . The spin then precesses in the x - y plane and also relaxes to align itself back along the z -axis. This is the basis for the simplest of NMR experiments. The precession of the spin as it is relaxing is what produces a voltage in an induction coil, which is the recorded free induction decay signal.

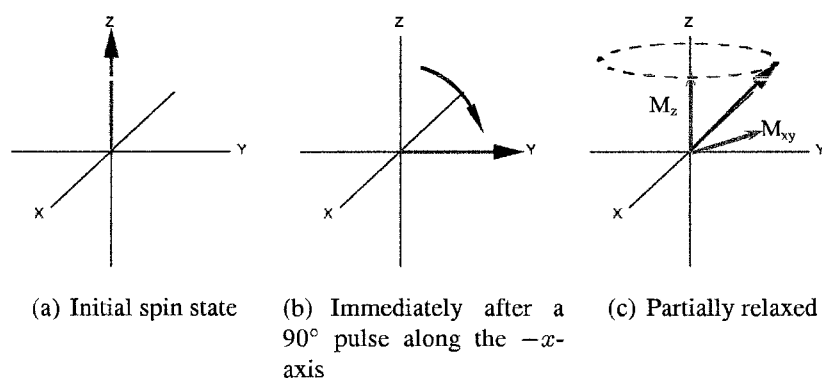


FIG. 2.2: The evolution of a single nuclear spin during the course of 90° single-pulse NMR experiment. The 90° pulse rotates the magnetization to the x - y plane. It then precesses around the z -axis as it relaxes back to equilibrium.

The rate at which the spin precesses around the z -axis is equal to 2π times the Larmor frequency, and is referred to here as ω_0 , defined as

$$\omega_0 = -\gamma B_0 = 2\pi\nu_0. \quad (2.6)$$

The Larmor frequency is different for different nuclei, and is further affected as a result of perturbations that result from the local structure around the nucleus as mentioned earlier. Some of these effects will be discussed in detail in Section 2.4.

2.2.2 Spin-Lattice and Spin-Spin Relaxation

As already mentioned, in the absence of an rf pulse, the spins will relax to realign with the static field, with the energy level populations settling into a Boltzmann distribution at thermal equilibrium (Equation 2.4). This relaxation process can be broken down into two components, longitudinal and transverse; both of which are affected by various interactions in the sample. The transverse relaxation is governed by spin-spin exchanges, and the longitudinal relaxation by spin-lattice exchanges. Therefore, studying the various relaxation processes of the nuclei can provide a substantial amount of information about the dynamics of the system. It is also necessary to have some understanding of both components of the relaxation in order to successfully optimize NMR experiments on the sample.

Longitudinal magnetization, in a process termed “spin-lattice relaxation”, evolves exponentially towards equilibrium,

$$M(\tau) = M(\infty) + (M(0) - M(\infty))e^{-\tau/T_{1z}}. \quad (2.7)$$

This equation is the result of solving the z-component of the Bloch equations [12],

$$\frac{dM_z}{dt} = \frac{M_0 - M_z}{T_1} + \gamma(\mathbf{M} \times \mathbf{H})_z, \quad (2.8)$$

that describe how the various components of the net magnetization evolve with time. T_{1z} is the time constant used to describe the rate at which the spins return to equilibrium. The relaxation is a result of the individual spins exchanging energy with the lattice, which is assumed to remain at thermal equilibrium at all times. The actual mechanism through which the nuclei exchange energy with the lattice depends on the material. For instance in metals, the nuclei relax by coupling to the spin magnetic moments of the conduction electrons [13], while in organic crystalline materials and other insulators, dipolar coupling

is often a dominant source of relaxation [12].

It is useful to have some knowledge of the T_{1z} value of a sample when performing an NMR experiment. Since it is usually desirable to have the system at equilibrium at the start of each acquisition, T_{1z} determines how frequently scans can occur without loss of sensitivity. Most commonly, a recycle delay of three to five times the relaxation time is used between scans. This is longer than the $\sim 1.5T_{1z}$ recycle delay recommended [14] for the maximum signal-to-noise ratio for a given experimental time but avoids saturation and line shape distortion due to site- or orientation-dependant T_{1z} .

Depending on the sample, the value of T_{1z} can vary significantly and is affected by factors such as sample temperature or magnetic field strength. For the purpose of this thesis, short T_{1z} values would be on the order of milliseconds, while some materials have T_{1z} values that are minutes long. For samples with excessively long T_{1z} values, some types of NMR experiments may be impractical simply due to the amount of time it would take to obtain a reasonable signal-to-noise ratio. An approximate value of T_{1z} is usually determined as part of optimizing any NMR experiment. An estimated value can be determined by varying the recycle delay and choosing a time that shows no difference in the spectrum compared with longer times.

Transverse magnetization, in a process referred to as “spin-spin relaxation”, decays exponentially to zero following an initial excitation. This can be described by the x - and y - components of the Bloch equations given by,

$$\frac{dM_i}{dt} = \gamma(\mathbf{M} \times \mathbf{H})_i - \frac{M_i}{T_2}, i = x, y. \quad (2.9)$$

In this case, T_2 is the exponential time constant describing the transverse relaxation rate, $R_2 = T_2^{-1}$. One cause for T_2 relaxation in solids is the dipole-dipole interaction between neighboring nuclei resulting in a distribution of spin precession rates, the dephasing of which is the cause of the spin-spin relaxation. Each nucleus experiences a local field

generated by neighboring nuclei, and this local field can either shield or deshield the static field in the vicinity of the nucleus. Because of this, even if all nuclei begin in phase, over time they would get out of sync, leading to a decrease in the net magnitude of the transverse magnetization and eventually resulting in the transverse component of the net magnetization being reduced to zero. During an experiment, the value of T_2 governs how long the resulting signal will last after each pulse sequence. In liquids, the random isotropic motion causes T_{1z} and T_2 to be equal, however in solids, it is most often the case that T_2 is orders of magnitude shorter than T_{1z} [9], on the order of tens of microseconds.

2.2.3 The Density Matrix

A convenient way to represent the evolution of a system in an NMR experiment is through the use of spin density matrix theory. The density matrix ρ , which has the form of

$$\rho = \begin{pmatrix} \rho_{11} & \rho_{12} & \rho_{13} \\ \rho_{12}^* & \rho_{22} & \rho_{23} \\ \rho_{13}^* & \rho_{23}^* & \rho_{33} \end{pmatrix}, \quad (2.10)$$

represents the energy level populations and transitions with the diagonal elements representing the population of each energy level, while the off-diagonal elements indicate coherent superpositions of energy levels. The matrix itself is Hermitian, with the size of the matrix determined by the spin of the nucleus. The 3x3 matrix shown in Equation 2.10 represents the three-level system of a spin-1 nucleus. The way that the density matrix evolves with time depends on the Hamiltonian and is determined by the Liouville-Von Neuman relation,

$$\dot{\rho} = i[\rho, H]. \quad (2.11)$$

Solving this differential equation allows the time-domain signal, which is the ensemble average expectation value of transverse magnetic moment (either I^- or I^+), to be calculated through the use of

$$s(t) = \langle I^- \rangle = \text{trace}(\rho(t)[I_x - iI_y]). \quad (2.12)$$

Depending on the complexity of the Hamiltonian of the system, it may be possible to solve Equation 2.11 analytically in closed form, but in most cases numerical solutions are required. When solving the differential equations directly isn't practical, there are various approximations that can be used that make it possible to solve even many-site systems with complicated Hamiltonians, such as Floquet Theory [15]. Regardless of the method used, once the time-domain spectrum has been calculated, a Fourier transform puts it into the familiar frequency-domain, where it can then be easily compared with experimental results. Further details of the calculation of NMR line shapes will be discussed in Chapter 4.

2.3 Magic Angle Spinning

Magic Angle Spinning (MAS) is a technique commonly used in solid state NMR experiments to help simplify complicated spectra and make interpretation and analysis easier. It is mostly used to remove, or at least reduce, the effects of chemical shift anisotropy as well as heteronuclear dipolar coupling. It also has the added benefit of narrowing lines from quadrupolar nuclei [16].

In a liquid sample, the orientation-dependence of the interaction tensors usually average to zero, removing any effects of chemical shift anisotropy or dipolar coupling. This is due to the rapid isotropic tumbling of the molecules. The rate of motion is much faster than the magnitude of the effects due to chemical shift anisotropy and dipole-dipole cou-

pling in frequency units.

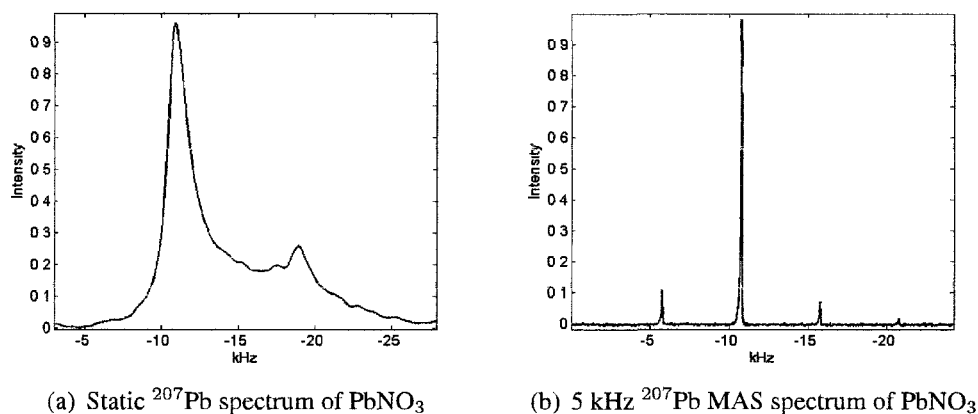


FIG. 2.3: Using MAS to simplify the results of solid-state NMR. The broad powder-pattern of a static ^{207}Pb spectrum of PbNO_3 is reduced to a series of narrow peaks through the process of magic angle spinning.

In powdered solid samples, the molecules or ions in the lattice are fixed, which determines the direction of the interaction tensors. This leads to an angular distribution of directions that results in a broad powder NMR spectrum. For example, the results of a ^{207}Pb spectrum of lead nitrate [$\text{Pb}(\text{NO}_3)_2$] without MAS is shown in Figure 2.3(a).

This is a typical chemical shift anisotropy (CSA) powder pattern spectrum, with the total signal intensity distributed over a 10 kHz range. This example has a single unique site for the lead nuclei, making it relatively easy to analyze. It is possible to obtain the principal values of the chemical shielding tensor without too much difficulty. In the case of materials with multiple sites, the resulting overlapping powder patterns can be very difficult to interpret, with no obvious or unique way to deconvolute the spectrum.

One approach to dealing with the broad inhomogeneous distributions that arise in complex solid samples is to utilize MAS, which entails spinning the sample around a specific axis at a constant speed while the NMR experiment is performed. An overview of the setup for a magic angle spinning experiment is shown in Figure 2.4. The sample is contained in a rotor that is spun about an axis that is 54.7° from the direction of the static field. The actual mechanics of how an MAS experiment is performed will be more

thoroughly discussed in Chapter 3.1.

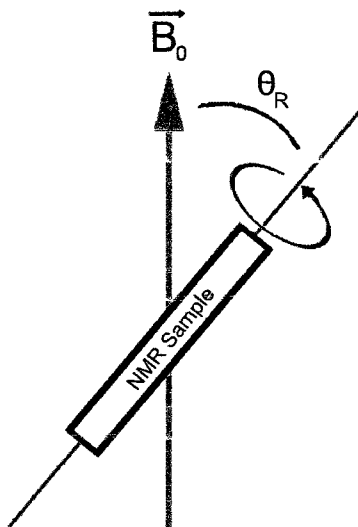


FIG. 2.4: Diagram of a Magic Angle Spinning experiment. During an MAS experiment, the sample is spun around the direction θ_R in order to reduce the effect of anisotropy.

Since the orientation-dependent part of most interactions can be shown to be proportional to $(3 \cos^2 \theta - 1)$ [13, 16], where θ is the angle between the principal z -axis of the interaction tensor and the static field, it is possible to eliminate that portion of the interaction by getting the average value of $(3 \cos^2 \theta - 1)$ to be zero. It can be shown [9] that the average value is determined as in

$$\langle 3 \cos^2 \theta - 1 \rangle = \frac{1}{2} (3 \cos^2 \theta_R - 1) (3 \cos^2 \beta - 1), \quad (2.13)$$

where θ is the principal z -axis of the shielding tensor with respect to the static field, θ_R is the direction of the axis of rotation for the spinning rotor, and β is the angle between the largest principal component of the shielding tensor and the axis of rotation. By rotating the sample sufficiently fast around θ_R , the average value of $(3 \cos^2 \theta - 1)$ goes to zero if angle θ_R is set precisely to the “magic angle” of 54.7° , where $\arccos \theta_R = 1/\sqrt{3}$. “Sufficiently fast” is when the spin rate is comparable to the strength of the interaction (in kHz). A spin rate of three to four times the interaction strength will completely eliminate

the anisotropic component of the interaction, reducing the spectrum to a single line at the isotropic chemical shift. In addition, since the total signal intensity will remain constant, the apparent signal-to-noise will appear significantly better since the intensity is now concentrated in a single peak and not distributed across an entire powder pattern. Most of the experiments described in later chapters were performed at spinning speeds of 30 kHz. The latest high-speed spinning probes available are capable of approximately twice that speed. With the strength of the interactions discussed in later chapters (on the order of several hundred kHz), this means that it is not always possible to completely eliminate the anisotropic component of the interactions.

In the case of an MAS experiment where the spin rate is not fast enough to completely eliminate the anisotropic component, spinning sidebands result. The spinning sidebands are sharp peaks that occur at multiples of the spinning speed, spaced symmetrically around the isotropic peak [17]. The actual widths of each of the peaks is dependent upon the T_2 relaxation of the nucleus being studied as well as the strength of the static field. If the spin rate is not so fast as to completely eliminate the anisotropy, the tops of the isotropic peak and spinning sidebands will trace out the powder pattern that would result from a static experiment, making the spinning sideband intensities useful in the analysis. Thus, the relative intensities can give information about the anisotropic interactions that are being partially eliminated. With the spectrum reduced to a series of peaks instead of broad distributions, it can be much easier to distinguish between overlapping sites. The spinning sidebands' contribution to the spectrum can be calculated by starting with the equation [9],

$$\omega(\Omega; t) = -\omega_0 \mathbf{b}_0 \boldsymbol{\sigma} \mathbf{b}_0. \quad (2.14)$$

This equation shows the contribution to the observed frequency for a particular orientation Ω of the chemical shielding tensor, $\boldsymbol{\sigma}^R$ (which will be discussed in section 2.4.1),

where \mathbf{b}_0 represents the unit vector for the \mathbf{B}_0 axis as defined in the frame of the spinning rotor and can be written as

$$\mathbf{b}_0 = (\sin \theta_R \cos \omega_R t, \sin \theta_R \sin \omega_R t, \cos \theta_R), \quad (2.15)$$

where ω_R is the spinning rate. Using this definition for \mathbf{b}_0^R in the equation for the spectral frequency, and rearranging terms through the use of trigonometric identities [17], leads to

$$\begin{aligned} \omega(\Omega, t) = & -\omega_0 \left\{ \sigma_{iso} + \frac{1}{2} (3 \cos^2 \theta_R - 1) (\sigma_{zz} - \sigma_{iso}) \right. \\ & + \sin^2 \theta_R \left[\frac{1}{2} (\sigma_{xx} - \sigma_{yy}) \cos(2\omega_R t) + \sigma_{xy} \sin(2\omega_R t) \right] \\ & \left. + 2 \sin \theta_R \cos \theta_R [\sigma_{xz} \cos(\omega_R t) + \sigma_{yz} \sin(\omega_R t)] \right\}, \end{aligned} \quad (2.16)$$

where σ_{iso} is referred to as the isotropic chemical shift of the interaction tensor and is defined as

$$\sigma_{iso} = \frac{1}{3} (\sigma_{xx} + \sigma_{yy} + \sigma_{zz}). \quad (2.17)$$

The components of σ_{ij} can be rewritten in terms of the components of the tensor in the principal axis system (PAS) through the use of a rotation matrix $\mathbf{R}(\alpha, \beta, \gamma)$. The principal axis frame is defined as the frame in which the interaction tensor is diagonal. The rotation is performed as in the equation

$$\boldsymbol{\sigma} = \mathbf{R}^{-1}(\alpha, \beta, \gamma) \begin{pmatrix} \sigma_{xx}^{PAS} & 0 & 0 \\ 0 & \sigma_{yy}^{PAS} & 0 \\ 0 & 0 & \sigma_{zz}^{PAS} \end{pmatrix} \mathbf{R}(\alpha, \beta, \gamma). \quad (2.18)$$

Using this rotation matrix, with the magic angle $\theta_R = 54.7^\circ$, leads to spectral frequency components

$$\begin{aligned} \omega(\alpha, \beta, \gamma; t) = & -\omega_0\{\sigma_{iso} + [A_1 \cos(\omega_R t + \gamma) + B_1 \sin(\omega_R t + \gamma)] \\ & + [A_2 \cos(2\omega_R t + 2\gamma) + B_2 \sin(2\omega_R t + 2\gamma)]\}, \end{aligned} \quad (2.19)$$

where

$$A_1 = \frac{2}{3}\sqrt{2} \sin \beta \cos \beta [\cos^2 \alpha (\sigma_{xx}^{PAS} - \sigma_{zz}^{PAS}) + \sin^2 \alpha (\sigma_{yy}^{PAS} - \sigma_{zz}^{PAS})] \quad (2.20a)$$

$$B_1 = \frac{2}{3}\sqrt{2} \sin \alpha \cos \alpha \sin \beta (\sigma_{xx}^{PAS} - \sigma_{yy}^{PAS}) \quad (2.20b)$$

$$\begin{aligned} A_2 = \frac{1}{3} & ((\cos^2 \beta \cos^2 \alpha - \sin^2 \alpha) (\sigma_{xx}^{PAS} - \sigma_{zz}^{PAS})) \\ & + (\cos^2 \beta \sin^2 \alpha - \cos^2 \alpha) (\sigma_{yy}^{PAS} - \sigma_{zz}^{PAS}) \end{aligned} \quad (2.21a)$$

$$B_2 = -\frac{2}{3} \sin \alpha \cos \alpha \cos \beta (\sigma_{xx}^{PAS} - \sigma_{yy}^{PAS}). \quad (2.21b)$$

The σ_{iso} term gives the center peak seen in the spectrum, while the $\omega_R t$ terms lead to features at multiples of the rotor frequency; the spinning sideband manifold. In the case where the spin rate is much greater than the anisotropy, the effects of these terms is negligible in the spectrum [17]. The sideband intensities for arbitrary spin rates can be expressed as infinite sums of Bessel functions [17] or evaluated numerically [9].

Due to the fact that the chemical shift anisotropy is directly proportional to the strength of the static field, as higher fields are used, faster spinning speeds are required in order to completely reduce the spectrum to its isotropic components. Also, it is worth noting that it is not necessarily the case that the most intense peak is the isotropic one. The only way to be completely sure which peak is the isotropic shift is to vary the spin-

ning speed. All of the spinning sidebands will shift so as to occur at multiples of the new spinning speeds, while the isotropic peak will remain at a constant position. Identifying the center peak is very useful in differentiating between multiple sites [17].

The difference in NMR spectra that results from spinning under MAS conditions as opposed to a static experiment is shown in Figure 2.3. Both spectra are of the ^{207}Pb nucleus in lead nitrate $[\text{Pb}(\text{NO}_3)_2]$. The wide powder pattern of the static spectrum is shown in Figure 2.3(a). By using magic angle spinning at a spin rate of 5 kHz, the spectrum is reduced to a relatively narrow central peak, located at the value of the isotropic chemical shift of the powder pattern, as well as a series of spinning sidebands, as shown in Figure 2.3(b).

If there are multiple unique sites of a particular nucleus, a static experiment will often result in overlapping powder patterns— one for each site. One advantage of using MAS is that it makes it significantly easier to interpret spectra, particularly for samples that have overlapping line shapes. Another, very important advantage is in the increase of the observed signal-to-noise ratio. Since the total amount of sample is not changed between a static or MAS experiment, the total integrated intensity of the spectrum will remain constant. However in the case of an MAS experiment, all of this intensity is now concentrated into a handful of individual peaks, according to

$$\frac{(S/N)_{\text{MAS}}}{(S/N)_{\text{static}}} \simeq \frac{\Delta_{\text{static}}}{n\Delta_{\text{sideband}}}, \quad (2.22)$$

where Δ_{static} represents the width of the static powder pattern, Δ_{sideband} is the width of a sideband, and n is the total number of sidebands. For example, for a CSA powder pattern width of 20 kHz and 5 kHz MAS (resulting in four sidebands in addition to the center band) with $\Delta_{\text{sideband}} \sim 100$ Hz, the signal-to-noise gain is 40. This is a typical result.

2.4 NMR Tensor Interactions

As previously mentioned, the nuclei being observed in an NMR experiment are not isolated nuclei residing in the static field. They are surrounded by the electrons of the atom, as well as the nuclei and electrons of neighboring atoms or ions of the crystal. These other charges provide significant contributions to the NMR spectrum, in addition to the always-present Zeeman interaction resulting from the external field. These effects cause the local field felt by the observed nucleus to change, effectively altering its resonant frequency.

Since the change in resonant frequency is highly dependent on the local structure near the nucleus, different crystallographic sites will respond differently in an NMR experiment. This is the basis for determining structural information of a system from a solid state MAS NMR spectrum. These next few sections will describe several of the interactions that are relevant to the materials that are studied in Chapters 4 and 5, beginning with the chemical shielding interaction.

2.4.1 The Chemical Shielding Interaction

The strong static field causes the electrons to circulate around it; this causes an induced opposing field to manifest at the center of motion, the location of the nucleus. The effect of this opposing field is partial shielding of the static field at the nucleus, which is referred to as the diamagnetic component of the chemical shielding interaction. With the effective local field altered in this way, the resonant frequency of the nucleus is affected. This change in frequency, measured relative to some standard reference material, is referred to as the chemical shift tensor.

$$\hat{\mathcal{H}}_{CS} = \gamma \hat{I} \cdot \sigma \cdot B_0 \quad (2.23)$$

The diamagnetic contribution of the chemical shielding goes as $1/r^3$, where r is the electron-nucleus distance [9]. This results in the largest contribution of chemical shielding coming from the core electrons. However, the valence electrons of neighboring atoms can still have a noticeable effect on the chemical shift.

The external field also distorts the electron distribution, mixing excited state electrons into the ground state. This results in the nucleus being effectively deshielded [9]. In most cases (except for isolated atoms) the ‘‘paramagnetic’’ contribution (i.e., upfield, rather than downfield) is significantly larger than the diamagnetic part. It is hard to compute, because this requires highly accurate quantum calculations of excited states.

The Cartesian chemical shielding contribution to the Hamiltonian is shown in Equation 2.23. σ is the chemical shielding tensor, a second-rank tensor that defines the strength of the chemical shielding interaction for nuclear spin I in the B_0 field. The chemical shielding tensor can be separated into two components: the symmetric (σ^s) and anti-symmetric (σ^{as}) parts,

$$\sigma^{PAS} = \sigma^s + \sigma^{as}, \quad (2.24)$$

where

$$\sigma^s = \begin{pmatrix} \sigma_{xx} & \frac{1}{2}(\sigma_{xy} + \sigma_{yx}) & \frac{1}{2}(\sigma_{xz} + \sigma_{zx}) \\ \frac{1}{2}(\sigma_{xy} + \sigma_{yx}) & \sigma_{yy} & \frac{1}{2}(\sigma_{yz} + \sigma_{zy}) \\ \frac{1}{2}(\sigma_{xz} + \sigma_{zx}) & \frac{1}{2}(\sigma_{yz} + \sigma_{zy}) & \sigma_{zz} \end{pmatrix} \quad (2.25a)$$

$$\sigma^{as} = \begin{pmatrix} 0 & \frac{1}{2}(\sigma_{xy} - \sigma_{yx}) & \frac{1}{2}(\sigma_{xz} - \sigma_{zx}) \\ \frac{1}{2}(\sigma_{xy} - \sigma_{yx}) & 0 & \frac{1}{2}(\sigma_{yz} - \sigma_{zy}) \\ \frac{1}{2}(\sigma_{xz} - \sigma_{zx}) & \frac{1}{2}(\sigma_{yz} - \sigma_{zy}) & 0 \end{pmatrix}. \quad (2.25b)$$

The reason for separating the shielding tensor components is that it is only the symmetric part that has any real influence on the NMR spectrum. The antisymmetric contribu-

tions are of the order $\sigma^2 B_0 \sim 10^6$ smaller than the symmetric contribution. In addition, it is possible to choose a frame in which the symmetric part of the chemical shielding tensor is diagonal; the principal axis system (PAS). The direction of this frame depends on the local electronic structure around the nucleus. In the PAS frame, the diagonal components of σ are referred to as the principal values, σ_{xx} , σ_{yy} , and σ_{zz} , defined such that

$$|\sigma_{zz} - \sigma_{iso}| > |\sigma_{yy} - \sigma_{iso}| > |\sigma_{xx} - \sigma_{iso}|. \quad (2.26)$$

These values can be alternately expressed as the isotropic value σ_{iso} , the anisotropy Δ_{CS} , and the asymmetry η [18, 19], defined as

$$\sigma_{iso} = \frac{1}{3}(\sigma_{xx}^{PAS} + \sigma_{yy}^{PAS} + \sigma_{zz}^{PAS}) \quad (2.27a)$$

$$\Delta = \sigma_{zz}^{PAS} - \sigma_{iso} \quad (2.27b)$$

$$\eta = \frac{\sigma_{yy}^{PAS} - \sigma_{xx}^{PAS}}{\Delta}. \quad (2.27c)$$

This is the IUPAC-approved (International Union of Pure and Applied Chemistry) convention for reporting tensor components which has been widely, but not universally [20], adopted by the NMR community. Expressing the principal values in this manner makes it easier to describe the NMR spectrum. The isotropic value moves the entire spectrum up or down field relative to a carrier frequency. The anisotropy describes the width of frequency region covered by the spectrum. The asymmetry (which can vary between zero and one) describes the shape of the powder pattern (and also relative intensities of sidebands, in the case of magic angle spinning experiments as described in Section 2.3).

With the three principal components and the relative direction of the PAS frame, it is possible to accurately describe the resulting NMR spectrum due to the chemical shielding interaction. This can be easily combined with other interactions which may be present in

the system, such as the quadrupole or paramagnetic interactions.

2.4.2 The Paramagnetic Interaction

Aside from the Zeeman interaction, the paramagnetic interaction is the most significant one for the complex oxides $\text{Nd}_{\frac{2}{3}-x}\text{Li}_{3x}\text{TiO}_3$ that will be discussed in detail in Chapter 4. Like the chemical shielding interaction, the paramagnetic interaction results from the effect of the external magnetic field on the electrons in the material. However, the resulting interaction is very different. When some of the electrons have unpaired spins in the ground electronic state, electron-nuclear dipolar coupling, modulated by very fast electron spin relaxation, has a profound effect on the resonance of nearby nuclei. This change in the local field of the nucleus is what is referred to as the paramagnetic *interaction*, not to be confused with the “paramagnetic” contribution to the ordinary chemical shift. In the case of the $\text{Nd}_{\frac{2}{3}-x}\text{Li}_{3x}\text{TiO}_3$ materials, it is the electrons of the strongly paramagnetic neodymium atoms that couple with the observed lithium nuclei to produce a large paramagnetic interaction. In many situations where significant unpaired electron density is transferred into core orbitals of nearby nuclei, electron-nuclear hyperfine coupling also occurs. This interaction is probably not important for the Nd^{+3} ions in this study, since the atomic F-orbitals on Nd^{+3} that contain unpaired electrons are strongly localized on the Nd^{+3} cations.

While the nature of the interactions themselves are quite different, the mathematics describing the paramagnetic interaction are not too different from those used to describe the chemical shielding interaction. The Hamiltonian for dipolar coupling between a nucleus and single electron is given by,

$$\mathcal{H}_{en} = \overline{\mu_e} \cdot D_{en} \cdot \mu_N = \gamma_N \mu_e \cdot D_{en} \cdot I, \quad (2.28)$$

where $\overline{\mu_e}$ is the average moment of the electron and μ_N is the moment of the nucleus

with spin I [21]. D_{en} represents the dipolar coupling tensor between the electrons of the neodymium and the lithium nucleus and is defined as

$$D_{\alpha\beta} \equiv \frac{1}{r^3}(\delta_{\alpha\beta} - 3e_\alpha e_\beta), \quad (2.29)$$

where r is the distance between the nucleus and electron, while e_α , e_β , and e_γ represent the x , y , z components of a unit vector between the two, giving the direction of the interaction tensor. It has been shown [22] that the thermally averaged magnetic moment for the neodymium's electrons can be expressed as

$$\overline{\mu_e} = \frac{\beta_e^2 S(S+1)}{3k_B T} g \cdot g \cdot B_0, \quad (2.30)$$

with the unpaired electron spin S , the Bohr magneton β_e , the Boltzmann constant k , the temperature T , and the the g -tensor of the unpaired electron. Using this definition, the Hamiltonian can be rewritten as

$$\mathcal{H}_{en} = \gamma_N B_0 \cdot \mathcal{P}_{en} \cdot I, \quad (2.31)$$

where \mathcal{P}_{en} represents the nuclear-electron dipolar coupling tensor as defined by

$$\mathcal{P}_{en} = C g \cdot g \cdot D_{en} \quad (2.32)$$

and with the scalar C ,

$$C = \frac{\beta_e^2 S(S+1)}{3k_B T}. \quad (2.33)$$

It is worth noting that the scalar component C is the only source of temperature dependence in this interaction. This means that if the paramagnetic tensor is being calculated for a system at various temperatures (as is done in Chapter 4), the tensor can

be calculated once. It then only needs to be scaled according to the C factor evaluated at the appropriate temperature in order to obtain the correct interaction tensor. This can allow for a significant lowering of the cost of the subsequent calculations (described in Section 4.4).

In order to determine the total effect of multiple neodymium sites near the lithium nucleus, the cumulative \mathcal{P}_{en} can be represented simply as a sum of the interactions between the nucleus and each individual site, out to a specific cutoff distance from the nucleus. The cutoff is determined based on at what point the contribution to the total tensor is considered to be negligible,

$$\mathcal{P}_{en} = \sum_i \mathcal{P}_{en,i} = \sum_i C g_i^2 \cdot D_{en,i}. \quad (2.34)$$

Actually calculating \mathcal{P}_{en} can be done most easily by representing it in the frame of the g -tensor of the electrons,

$$\mathcal{P}_{en}^g = \begin{pmatrix} p_{xx} & p_{xy} & p_{xz} \\ p_{yx} & p_{yy} & p_{yz} \\ p_{zx} & p_{zy} & p_{zz} \end{pmatrix}, \quad (2.35)$$

with the individual elements,

$$p_{xx} = g_{xx}^2 (1 - 3 \sin^2 \theta \cos^2 \phi) (C/r^3) \quad (2.36a)$$

$$p_{xy} = g_{xx}^2 (-3 \sin^2 \theta \cos \phi \sin \phi) (C/r^3) \quad (2.36b)$$

$$p_{xz} = g_{xx}^2 (-3 \sin \theta \cos \eta \cos \phi) (C/r^3) \quad (2.36c)$$

$$p_{yx} = g_{yy}^2 (-3 \sin^2 \theta \cos \phi \sin \phi) (C/r^3) \quad (2.36d)$$

$$p_{yy} = g_{yy}^2 (1 - 3 \sin^2 \theta \sin^2 \phi) (C/r^3) \quad (2.36e)$$

$$p_{yz} = g_{yy}^2 (-3 \sin \theta \cos \theta \sin \phi) (C/r^3) \quad (2.36f)$$

$$p_{zx} = g_{zz}^2 (-3 \sin \theta \cos \theta \cos \phi) (C/r^3) \quad (2.36g)$$

$$p_{zy} = g_{zz}^2 (-3 \sin \theta \cos \theta \sin \phi) (C/r^3) \quad (2.36h)$$

$$p_{zz} = g_{zz}^2 (1 - 3 \cos^2 \eta) (C/r^3). \quad (2.36i)$$

Here, ϕ and θ represent the azimuthal and polar vectors, respectively, between the nucleus and each electron relative to the g -tensor frame. In general, this tensor is not traceless. However, much like the chemical shielding tensor, the anti-symmetric components can be ignored when the spectrum is calculated. This allows the spectra to be defined only in terms of the principal components of the diagonalized \mathcal{P}_{en} tensor. Using the three principal components of \mathcal{P}_{en} , the parameters of the paramagnetic contribution to the spectrum can be described as,

$$\delta_{iso} \equiv \frac{1}{3} (p_{xx} + p_{yy} + p_{zz}) \quad (2.37a)$$

$$\Delta\sigma \equiv p_{zz} - \frac{1}{2} (p_{xx} + p_{yy}) \quad (2.37b)$$

$$\eta \equiv \frac{p_{yy} - p_{xx}}{p_{zz} - \delta_{iso}}, \quad (2.37c)$$

with

$$|p_{zz} - \delta_{iso}| > |p_{yy} - \delta_{iso}| > |p_{xx} - \delta_{iso}|. \quad (2.38)$$

In this form, the spectrum is defined in terms of the isotropic value δ_{iso} , the anisotropy $\Delta\sigma$, and the asymmetry η . These three parameters can be used to define the appearance of the spectra in the same way the chemical shielding counterparts do. δ_{iso} shifts the entire spectrum up or down field, $\Delta\sigma$ determines the total coverage in frequency-space of the spectrum, and η determines the shape of the spectrum. The process of actually using these values to simulate a line shape will be detailed in Chapter 4.

2.4.3 The Quadrupole Interaction

The quadrupole interaction results from the non-spherical electric charge distribution in the nucleus interacting with the local electric field gradient. Any location that is not in the center of a symmetric cubic lattice will have a non-zero electric field gradient. The degree to which the nucleus is affected by the EFG is determined by the quadrupole moment of the nucleus.

“Quadrupole” refers to the order of charge distribution in the nucleus. The monopole order only describes the nucleus as a single positive charge, while the dipole splits it into negative and positive regions. However, the electric dipole is always zero in the nucleus. Otherwise the charges would interact with the nucleus’ own electric field and the generated force would rearrange the charge distribution in such a way as to make the dipole zero. The next level of charge distribution is the quadrupole, which is what interacts with the local electric field gradient to produce the interaction described in this section. All nuclei with spins $I > 1/2$ will have an electric quadrupole moment, in addition to the magnetic dipole moment that all nuclei have.

The Hamiltonian for a quadrupolar nucleus interacting with a local electric field gradient [9], \hat{V} is given by

$$\hat{\mathcal{H}}_Q = \frac{eQ}{2I(2I-1)\hbar} \hat{\mathbf{I}} \cdot \hat{\mathbf{V}} \cdot \hat{\mathbf{I}} \quad (2.39a)$$

$$\hat{\mathcal{H}}_Q = \frac{eQ}{6I(2I-1)\hbar} \sum_{\alpha,\beta=x,y,z} V_{\alpha\beta} \left[\frac{3}{2} (\hat{I}_\alpha \hat{I}_\beta + \hat{I}_\beta \hat{I}_\alpha) - \delta_{\alpha\beta} \hat{I}^2 \right], \quad (2.39b)$$

where $\hat{\mathbf{I}}$ is the nuclear spin vector and Q is the nuclear quadrupole moment. Q is a property of the type of nucleus and is the same regardless of the local environment. α , β , and γ refer to the x , y , and z coordinates of whatever axis system the electric field gradient is defined in, usually the PAS.

The components of the electric field gradient are used to define the anisotropy of the field gradient tensor: the quadrupole coupling constant C_Q and the asymmetry parameter η_Q .

$$C_Q = \frac{V_{zz}^{PAS} eQ}{\hbar} \quad (2.40a)$$

$$\eta_Q = \frac{V_{yy}^{PAS} - V_{xx}^{PAS}}{V_{zz}^{PAS}}. \quad (2.40b)$$

As with the chemical shift interaction, it is sometimes easier to use terms like this to describe the interaction than to report it in terms of the tensor components since it gives direct information about the spectrum. C_Q is analogous to span and determines the frequency range of the spectrum due to the quadrupole interaction and η_Q determines the asymmetry of the spectrum. Unlike the previous two interactions discussed, there is no isotropic component present, because $V(\mathbf{r})$ is a traceless tensor.

The principal axis system (PAS) is chosen so as to diagonalize the quadrupole Hamiltonian, with the principal values defined such that $|V_{zz}| > |V_{yy}| > |V_{xx}|$. The EFG tensor itself is a symmetric traceless tensor [23],

$$V_{ij} = \lim_{r \rightarrow \text{inf}} \left(\frac{\delta^2 V(\mathbf{r})}{\delta r_i \delta r_j} - \frac{1}{3} \delta_{ij} \nabla^2 V \right), \quad (2.41)$$

where $V(\mathbf{r})$ is the Coulomb potential. This results in a field gradient described by

$$V_{ij}(\mathbf{r}) = \frac{q}{4\pi\epsilon_0 r^5} \begin{pmatrix} r_y^2 + r_z^2 - 2r_x^2 & -3r_x r_y & -3r_x r_z \\ -3r_x r_y & r_x^2 + r_z^2 - 2r_y^2 & -3r_y r_z \\ -3r_x r_z & -3r_y r_z & r_x^2 + r_y^2 - 2r_z^2 \end{pmatrix}, \quad (2.42)$$

where $V_{ij}(\mathbf{r})$ is the electric field gradient at a given position due to a charge q located at \mathbf{r} . The net EFG at this position can be calculated by summing over all charges in the area. Using the above definitions for C_Q and η_Q given the tensor \hat{V}_{ij} , the Hamiltonian can then be rewritten as

$$\hat{\mathcal{H}}_Q = \frac{C_Q}{4I(2I-1)} [3\hat{I}_{zPAS}^2 - \hat{I}^2 + \frac{1}{2}\eta_Q(\hat{I}_{xPAS}^2 - \hat{I}_{yPAS}^2)]. \quad (2.43)$$

In Chapter 4 we will show how this Hamiltonian, combined with the paramagnetic interaction, can be used to simulate the NMR line shapes of the $\text{Nd}_{\frac{2}{3}-x}\text{Li}_{3x}\text{TiO}_3$ materials.

CHAPTER 3

Experimental Methods

3.1 Experimental Equipment Overview

The nuclear interactions that make NMR useful in condensed matter physics were explained in Chapter 2. The purpose of this chapter is to describe how the experiments are actually performed. This includes the equipment used, the steps required to acquire the data, and procedures for analyzing the data to extract relevant NMR parameters for comparison with theory.

The majority of experiments were performed using a Bruker Biospin 750 MHz wide-bore magnet, operating at 17.6 T, and controlled by a Bruker AVANCE I spectrometer system. The superconducting magnet is kept continuously at field to ensure adequate field stability. Due to the low temperature requirements in order to maintain such a high field, it is a pumped magnet. This means that the primary method of keeping the temperature low is a liquid helium dewar, which is pumped on at all times by a vacuum pump in order to reduce the temperature of the liquid below the helium boiling point of 4.2 K. To insulate this dewar, it is surrounded by a vacuum chamber, which itself is surrounded by a liquid nitrogen chamber.

The main superconducting coils provide the static magnetic field. In addition to these, there are additional lower-powered room temperature shim coils that are used to shim the field in the vicinity of the sample to provide as homogenous a field as possible (within 1 part in 10^8). The shim settings are optimized for the individual probe being used as well as the type of experiment (static or MAS). Around the sample, located in the probe itself, there is a solenoid coil that is used to provide the transverse rf pulses as well as to detect the current induced by the precessing nuclear spins. The pulses themselves are supplied by a kilowatt amplifier, and are usually attenuated by approximately two to three decibels and are of the order of a few microseconds long, depending on the experiment. The actual power and duration of the pulses are optimized for the nucleus being observed as well as the specific experiment. The induced signal passes through a frequency filter (low-pass, high-pass, or bandpass) to reduce noise outside the desired range. It then enters the high-gain pre-amp before being digitized and processed by the spectrometer.

The frequency of the rf pulses used to manipulate the nuclear spins is referred to as the carrier frequency. It must be close to the Larmor frequency of the nucleus in the field and is adjusted in order to optimize the experiment. Ideally, the applied pulse would be on resonance. However in practice, being directly on resonance can occasionally lead to artifacts in the resulting spectrum due to receiver imperfections. For this reason, the applied pulses are usually slightly displaced from exact resonance during experiments. While the pulse that is seen by the nucleus is at the carrier frequency ω_0 , the pulse is not actually generated at this frequency. Instead, it is the result of the mixing of two separate pulses,

$$\omega_0 = \omega_{\text{IF}} \pm \omega_{\text{mix}}. \quad (3.1)$$

Depending on the spectrometer, either the sum or difference of the two frequencies could be used to reach the desired carrier frequency. The intermediate frequency ω_{IF}

is a constant frequency defined by the spectrometer and is completely independent of the nucleus being observed. In the case of the Bruker Avance I system used here, the intermediate frequency is 20 MHz. The mixing frequency ω_{mix} is used to bring the final carrier frequency to the desired value. While it may seem like needlessly complicating the process to generate a pulse, its purpose becomes clear during the acquisition phase of the experiment.

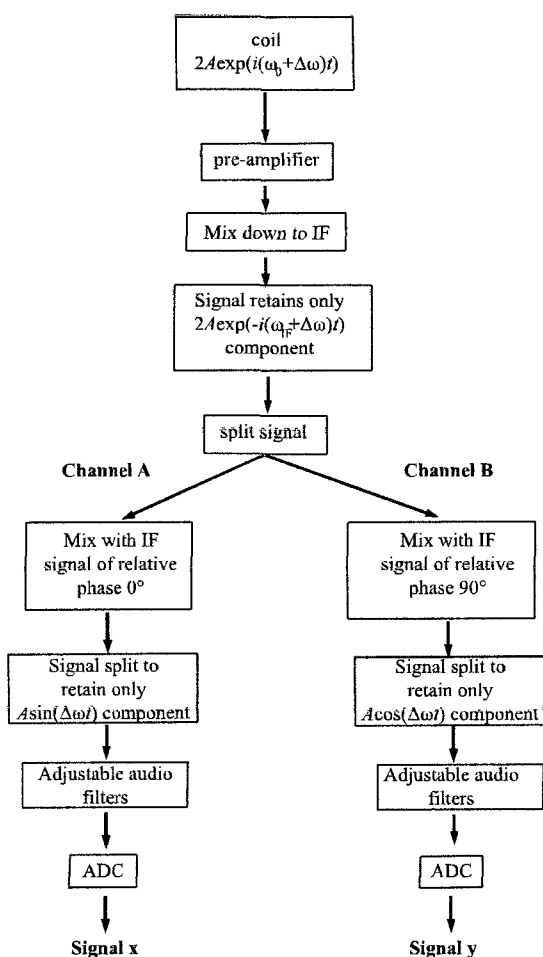


FIG. 3.1: Basic overview of the receiver stage of an NMR experiment

A simplified version of the receiver stage of an NMR experiment [9, 24] is shown in Figure 3.1. Following the radio frequency pulse sequence, the NMR signal is initially generated in the induction coil in the form of

$$2Ae^{i(\omega_0+\Delta\omega)t}, \quad (3.2)$$

where A is the amplitude of the signal and the spectrum is defined in terms of a series of frequencies centered around the carrier frequency. The signal is then sent through a low-noise pre-amp to increase the gain (≈ 30 dB) and as a consequence, both the noise and the signal increase in this stage. The pre-amp usually features an analog filter (bandpass, low-pass, or high-pass) that helps isolate the signal in the vicinity of the observed frequency. After the pre-amp, the signal is mixed down to make it of the form

$$2Ae^{i(\omega_{IF}+\Delta\omega)t}. \quad (3.3)$$

This now makes the spectrum a series of frequencies in the vicinity of the intermediate frequency instead of the carrier. At this point, a narrowband filter around the intermediate frequency is used. With the intermediate frequency being constant within the spectrometer, all spectra at this point will be contained in a relatively narrow range regardless of the nuclei being observed; typically ± 1 -2 MHz is the largest observable bandwidth. The major advantage of working around the intermediate frequency is that only one set of frequency filters and other adjustments is necessary to perform a wide range of NMR experiments (with optimal signal-to-noise) on different nuclei by choosing the carrier frequency.

With the signal now in terms of the intermediate frequency, it is split into two separate channels. One is mixed with ω_{IF} with a relative phase of 0° while the other is mixed with ω_{IF} at a relative phase of 90° . The two channels are usually referred to as “real” and “imaginary”, or alternately “A” and “B”. The real and imaginary parts correspond to current in phase and 90° out of phase relative to the carrier, respectively. Phase-sensitive detection is then used in each channel to isolate the audio components, $A \cos(\Delta\omega t)$ in the case of the real channel and $A \sin(\Delta\omega t)$ in the imaginary channel. The signals are then

each passed through two analog-to-digital converters and stored in a high-speed digital memory buffer, which can be routed as needed to normal computer memory for signal averaging.

In addition to the 17.6 T magnet, some NMR experiments were performed using a 7 T (300 MHz) Oxford magnet, along with an identical Bruker AVANCE I spectrometer. Since this is a lower-field magnet, it is not necessary to pump on the helium dewar. This spectrometer was used in order to observe any field-dependant properties of the NMR spectra. Using a lower field also has the advantage of reducing the strength of the chemical shielding interaction, making it easier to spin out interactions through the use of MAS.

Most experiments were performed under magic angle spinning conditions (as explained in Section 2.3) in a 2.5 mm variable temperature probe at various spin rates, as shown in Figure 3.2. Signal-to-noise and acquisition time were not major issues since the majority of experiments were observing the abundant lithium isotope ${}^7\text{Li}$, which is generally a very easy nucleus to observe. The 2.5 mm probe was used because it allows stable spinning at speeds up to 30 kHz.

${}^6\text{Li}$, the other isotope, was also observed in several materials. Unfortunately, the natural abundance of ${}^6\text{Li}$ (7.42%) and lower gyromagnetic ratio ($39.4 \times 10^6 \text{ rad s}^{-1} \text{ T}^{-1}$, as opposed to $104.0 \times 10^6 \text{ rad s}^{-1} \text{ T}^{-1}$ for ${}^7\text{Li}$) results in relatively poor signal-to-noise. However, the 2.5 mm probe was still used since the amount of material available did not allow for multiple samples to be prepared. For this reason, an acceptable quality ${}^6\text{Li}$ spectrum takes significantly longer to acquire. Most of the ${}^6\text{Li}$ experiments used at least three times the number scans as the ${}^7\text{Li}$ samples; even then, the signal-to-noise was still noticeably worse than for the ${}^7\text{Li}$ spectra. In the case of the $\text{Nd}_{\frac{2}{3}-x}\text{Li}_{3x}\text{TiO}_3$ samples, the ${}^7\text{Li}$ experiments ran for 100,000 scans, while the ${}^6\text{Li}$ experiments acquired 300,000. This is why the majority of experiments were focused on the ${}^7\text{Li}$ nuclei. In spite of these difficulties, the ${}^6\text{Li}$ spectra were useful in comparing to the simulations detailed in Chapter 4. For the purposes of calibrating the pulse power for both ${}^7\text{Li}$ and ${}^6\text{Li}$, an

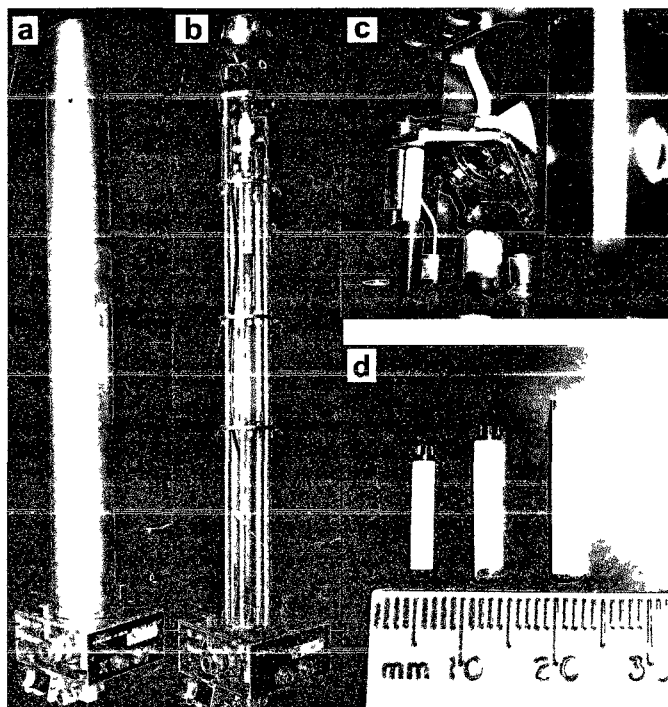


FIG. 3.2: (a) 2.5 mm MAS probe as it is used in the field and (b) with the outer casing removed, with (c) a close-up of the stator where the sample is located. The sample itself is packed inside 2.5 mm rotors (d) as shown. 3.2 mm and 4 mm rotors are included here for comparison.

aqueous LiCl solution was used.

The first step for preparing a sample is crushing it into a powder and packing it inside a sample rotor as seen in Figure 3.2(d). The top of the rotor has turbine fins where the drive gas is aimed to provide sufficient torque to rotate the sample in MAS experiments. The bottom of the rotor has half of the circumference around the edge blackened in order to provide a squarewave signal to be used as feedback to the spin rate controller. The rotor is then placed in the stator near the top of the probe. A cross-section of an MAS stator during a spinning experiment is shown in Figure 3.3. For MAS experiments, dry nitrogen gas is blown towards the rotor from the sides of the stator in order to stabilize it; this is the bearing gas. A second stream of nitrogen gas, the drive gas, is then blown along the fluted top of the rotor to provide torque and spin the rotor. An optical sensor is used to monitor the spin rate by observing the black mark on the bottom of the rotor. An electronic feedback controller is used to automatically adjust the bearing and drive

gas pressure to maintain the desired spin rate. Under normal conditions, the spin rate is usually held within a few Hz of the target rate, for several hours to several days.

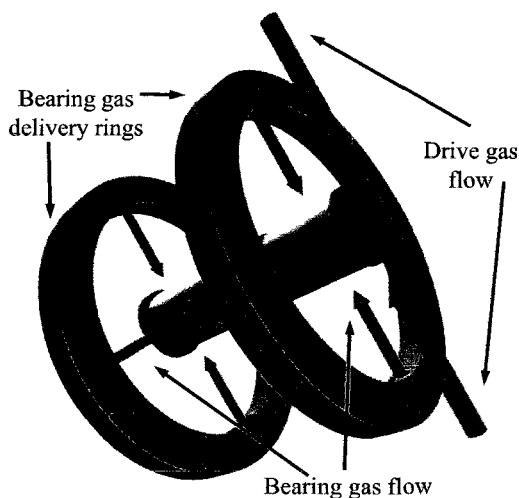


FIG. 3.3: Cross-section of an MAS stator. The coil and stator housing are left out for clarity. The bearing gas (blue) maintains the stability of the rotor, while the drive gas (red) propels it using the turbine cap of the rotor

The variable temperature probe used in these experiments can cover a range of approximately 210-330 K while the rotor is spinning. It is important to note that this is the target temperature and not the temperature of the sample itself. The temperature sensor is inline with the flow of VT gas to the sample rotor, but is not recording the actual temperature of the sample. The true sample temperature is always higher due to frictional heating that occurs as a result of the nitrogen gas spinning the rotor. A spin rate of 30 kHz can cause up to 30 K of frictional heating to the sample. This effect can be accounted for with proper calibration using lead nitrate, for which the temperature-dependant behavior is known, as shown in Appendix B. It is usually necessary to allow at least 15 minutes for a sample to come to thermal equilibrium before beginning an experiment.

To cool the sample during a variable temperature experiment, dry nitrogen gas is passed through a heat exchanger submerged in a liquid nitrogen dewar to lower its temperature. The gas then passes into a glass dewar inside the probe body. Inside this dewar,

the gas passes over a heating coil before entering the stator where the sample is located. By varying both the flow rate of the nitrogen gas as well as the current in the heating coil, the temperature can be controlled stably within 0.1 K (according to the sensor in-line with the gas flow). Temperature gradients in the sample can vary by more than this. The gas flow rate is set and remains constant during the experiment. The power to the heating coil is controlled automatically by the spectrometer software using a feedback loop that monitors the temperature in the vicinity of the sample. For variable temperature experiments above room temperature, room temperature gas is sent directly into the dewar and heated by the coil as needed.

3.2 Pulse Sequences

Different sequences of transverse radio frequency pulses are used to excite the spins and obtain an NMR signal. The actual sequence used for an experiment can depend on many factors, such as the nuclei being studied and the type of environment they are expected to be in. Some pulse sequences enhance certain energy transitions, while others may work to optimize the observed signal-to-noise of an experiment.

3.2.1 Zero-Go Pulse Sequence

The most basic NMR experiment commonly used is a single 90° pulse followed by signal acquisition, also referred to as a Zero-Go (ZG) pulse sequence. This sequence is shown in Figure 3.4, and consists of an initial delay D_1 followed by a single 90° pulse. Following this, the FID is acquired after a brief delay (“de” $> 15\text{-}20 \mu\text{s}$) is used in order to avoid pulse power being detected by the pre-amp receiver.

By optimizing each of these parameters, the sensitivity and signal-to-noise ratio can be greatly increased. The value chosen for D_1 is dependent upon the spin-lattice relax-

ation time of the sample, T_{1z} . The recycle delay is chosen to be sufficiently long for the spin system to return to thermal equilibrium before another pulse is applied. Since T_{1z} recovery is an exponential function (equation 2.7), the recycle delay is a compromise chosen to maximize the amount of time the system is allowed to recover while minimizing the total time for each scan. Typically, this is three to five times the length of T_{1z} , which allows the system to return to approximately 95%-99% of equilibrium. The optimal recycle delay value was shown by Ernst to be approximately $1.5T_{1z}$ [14]. However, most of the experiments performed here waited more than $3T_{1z}$ in order to avoid any saturation and line shape distortion due to site- or orientation-dependant T_{1z} across the line shape. If one site has a sufficiently long T_{1z} compared to other sites, it is possible to suppress it completely in the spectrum. This is often helpful in identifying and assigning individual sites in the spectrum.

The length and power of the pulse is chosen so that it rotates the magnetization 90° from the B_0 axis and the pulse is in the $x-y$ plane. There are usually specific phase cycles in a sequence in order to compensate for imperfections in the audio amplifiers. These include DC offsets in the receiver channels, as well as artifacts arising from unwanted coherence transfer pathways generated by pulses in multi-level spin systems. In addition to the relative phase of the pulses, the routing of the signal to the A and B channels is also changed in order to minimize these effects in the Fourier transformed spectra. The total number of scans for the experiment are then chosen to be a multiple of the number of phases in the cycle. In this specific case (the ZG pulse sequence), the phase cycle that was used was [x -x -x x y -y -y y] i.e., signals were accumulated on successive scans with phase 0, phase 180, phase 270, phase 0, phase 90, phase 270, phase 270, phase 0, and routed to computer memory in such a manner that “real” x and “imaginary” y pass through both digitizers and always appear in A and B sections of computer memory [24]. In this case, the real part would be routed as [A -A -A A B -B -B B], where ‘-A’ represents -1 times the signal routed to channel A.

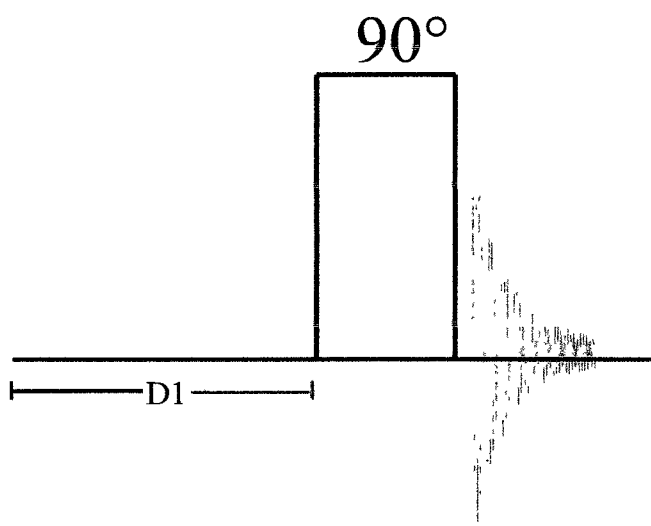


FIG. 3.4: Pulse sequence diagram of a ZG (Zero-Go) experiment. A single 90° pulse is used, followed by signal acquisition. The recycle delay of the pulse is adjusted to account for the relaxation time of the nuclei.

3.2.2 Hahn-Echo Pulse Sequence

Another common pulse sequence is the Hahn-Echo [25], shown in Figure 3.5, which was first developed by Hahn and Maxwell and used a pair of 90° pulses. The sequence was also discovered independently by Carr and Purcell, who used a 90 - 180 pulse sequence with both pulses along the x -axis [12]. The sequence was later modified by Meiboom and Gill to have the echo pulse along the y -axis [26].

It begins with the same delay, D_1 , as the basic single pulse experiment followed by a 90° pulse. After this, there is a delay, τ , before a second, 180° pulse is applied along an axis perpendicular to the first pulse. For instance, if the first pulse is along the x -axis, the second will be along the y -axis. Following this second pulse, the FID is acquired.

The second pulse functions to refocus the signal and produces an echo that is located τ after the pulse. This works by taking advantage of the dephasing of the nuclear spins in the system. Following the initial 90° pulse, the transverse component of the net spin will begin to dephase over time, as shown in Figure 3.6. The 180° pulse reverses the direction

of the precessing spins. This causes the magnitude of the transverse component of the spin to refocus (producing the echo) before continuing to dephase. In order to properly refocus the magnetization for a rotating sample, the pulse sequence must be synchronized with the rotor spin rate [27]. In an MAS experiment, the delay τ is chosen such that the time between the center of the two pulses is a multiple of a rotor cycle.

In the case of a single-pulse experiment, such as the ZG sequence described above, the signal occurs immediately following the pulse. This has the potential to cause problems if there is electronic ringing that results from the pulse at a frequency close to what is being observed. The signal can be significantly obscured by electronic noise. The advantage of the echo pulse sequence is that it allows the observed signal to be displaced in time from the rf pulse. The disadvantage of observing the echo is that the farther out the echo is, the lower the observed signal intensity. The rate at which the signal drops off is dependent upon the T_2 relaxation time. For a site with a very short T_2 , an echo experiment may not be a viable option. The phase sequence used for the Hahn-Echo experiments is Pulse 1: $[x\ y\ -x\ -y]$ and Pulse 2: $[x\ x\ x\ x\ y\ y\ y\ y\ -x\ -x\ -x\ -x\ -y\ -y\ -y\ -y]$. As with the previous pulse sequence, the signal routing is also adjusted to ensure the real signal goes to the A channel, with the routing going as $[A\ A\ A\ A\ B\ B\ B\ B\ -A\ -A\ -A\ -A\ -B\ -B\ -B\ -B]$.

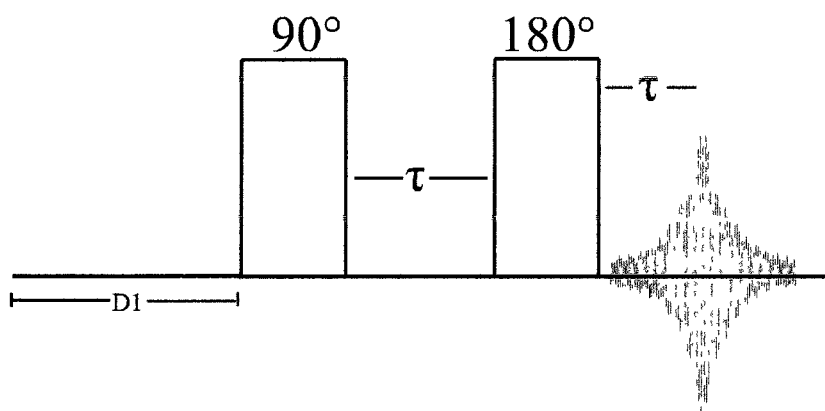


FIG. 3.5: Hahn-Echo pulse sequence. Following the initial 90° pulse, a second, 180° pulse is applied to refocus the signal in order to produce an echo spaced τ after the second pulse.

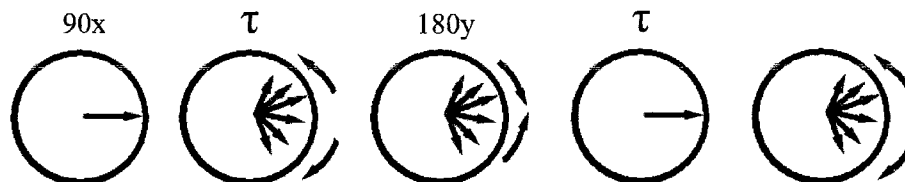


FIG. 3.6: Time evolution of transverse magnetization during a Hahn-echo NMR experiment. The dephasing transverse magnetization is rotated by a 180° pulse in order to produce an echo, which is recorded as the FID.

3.2.3 T_{1z} Saturation-Recovery Pulse Sequence

It is possible to determine the value of the spin-lattice relaxation time, T_{1z} , for nuclei in a material by using a variety of different pulse sequences. The experiment used in this work (described in Chapter 5) is the T_{1z} Saturation-Recovery pulse sequence and is shown in Figure 3.7. The beginning of the pulse sequence (following the initial recycle delay D_1) is a series of 90° pulses separated by delay d_{10} . The number and spacing of the pulses are optimized so that immediately following the pulse train, the system is completely saturated, i.e., the free induction decay (FID) recorded at this time will show no signal. After the saturation pulses, there is a delay τ before a detection 90° pulse, followed by the digitization of the FID signal. The phase sequence used for the acquisition pulse (the final 90° pulse) in this pulse program was [x x -x -x y y -y -y].

The complete saturation-recovery experiment is composed of a series of 1D spectra, each with a different value of the relaxation delay, τ . τ is varied such that the intensities of the resulting spectra can be fit to an exponential recovery curve in order to determine the value of T_{1z} , an example of which is shown in Figure 5.1. It is important to have an approximate value for the relaxation time when choosing values for the delay list. That way, a series of τ values can be chosen so that they are evenly distributed along the relaxation curve, including a short value which has the system sufficiently saturated. In addition, there is always an “infinity” value chosen which is sufficiently long that the system has nearly completely recovered. A good series of τ values usually contains on

the order of 10 to 15 values, which can make these experiments time consuming. When it comes to running the experiment, the ordering of the τ list is usually randomized to avoid systematic errors. This is meant to account for any spectrometer drift that may result over the course of the experiment. The data manipulation used to analyze the resulting spectra in order to obtain the values of T_{1z} will be discussed in more detail in Chapter 5.

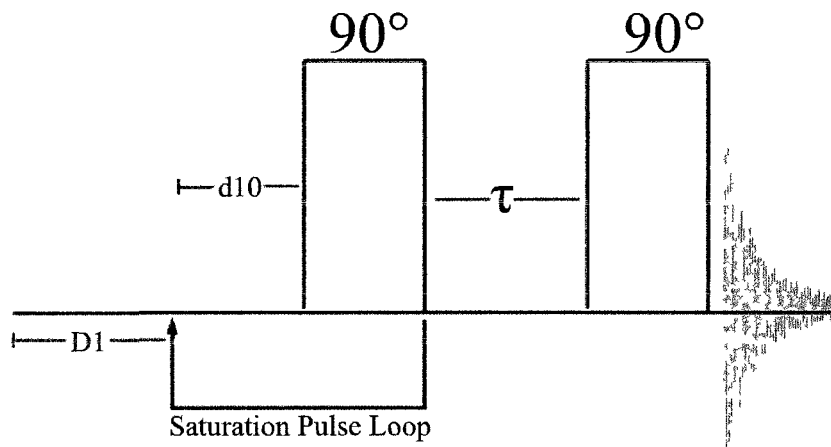


FIG 3 7 Pulse sequence diagram of a T_{1z} Saturation-Recovery experiment. After completely saturating the spectrum with the initial pulse train, the recovery of the system over time can be observed by varying the delay before the acquisition pulse.

3.3 Signal Processing

At the end of each pulse sequence, the free induction decay (FID) signal is digitized by the analog-to-digital converters (ADC) of the spectrometer and stored in computer memory. This signal is the current induced in the coil by nuclear spins as they precess and relax and is recorded in two ADC channels (real and imaginary signal) that are orthogonal to each other (described in Figure 3.1). The spectrometer ensures the proper routing of the audio components signal in order to cancel artifacts while allowing desired signals to accumulate. At this point, the signal can now be processed by the workstation to produce a usable spectrum. The FID is initially recorded in the time-domain, so it must first go

through a few steps of processing in order to transform it into the frequency-domain where it can be more easily interpreted.

In the case of an MAS experiment, the FID usually appears as a series of rotary echoes that decay exponentially over time, as seen in Figure 3.8(a). Depending on the phasing of the real and imaginary channels, there will likely be some signal visible in both channels. When on resonance, the zeroth-order phase correction of the FID can be adjusted such that there is a minimal amount of signal in the imaginary channel and a maximum in the real channel. The most effective way to phase the spectrum in the time-domain is to adjust the zeroth-order phase correction until the real part of the FID shows no signal, causing all of the signal to be isolated to the imaginary channel, followed by an additional 90° phase correction to bring it back to the real channel. When there are components of the spectrum off-resonance, this does not work since there will always be some signal in both channels. Alternatively, the phase correction can also be done after the Fourier transformation. When done in the frequency-domain, the goal is to adjust the phase until the real component of the spectrum is absorption mode. This usually requires both zeroth- and first-order phase corrections and can be slightly more difficult to determine when it is correct.

The beginning of the FID is also shifted so as to set the zero time of the acquisition on the peak of a rotary echo. Doing this decreases the likelihood of artifacts being introduced into the spectrum as a result of the finite recovery time of the electronics. Shifting points in this manner has the same effect as first-order phase correction, i.e. a linear combination $A_i \cos \phi_i + B_i \sin \phi_i$ where ϕ_i is proportional to the offset of frequency component ω_i from the center of the spectrum. The reason for this shift is that there is sometimes electronic noise resulting from some of the pulse bleeding into the receiver, or simply ringing in the electronic circuit. When this happens, it is necessary to shift past this initial noise. However, shifting farther than necessary can result in losing a lot of information on the high frequency components in the spectrum; this is also important if some regions of the

spectrum have a shorter T_2 relaxation time.

Another artifact in the frequency spectrum occurs if the signal acquisition time is not long enough. This leads to the FID being truncated and the usual fix for this is to multiply the FID by a decaying exponential, either Gaussian or Lorentzian, in order to get the FID to approach zero by the end of the acquisition time. This has the apparent effect of smoothing the spectrum in the frequency domain. While line broadening may make the signal-to-noise appear improved, overusing it can lead to compromised resolution: fine details in the spectrum being completely lost. Most of the experimental spectra shown in later chapters used Gaussian broadening on the order of a few hundred Hertz.

Once the time-domain FID has been processed, it is then Fourier transformed so as to present the signal in the frequency domain. The zeroth- and first-order phase correction of the Fourier transformation can then be further adjusted in order to provide an absorption mode spectrum, i.e., having a flat baseline with all of the signal appearing positive. It is not always possible to get a completely flat baseline, and occasionally the best phasing still results in a rolling baseline. If necessary, this can often be corrected by a spline fit and subtraction of the rolling baseline, depending on how important a flat baseline is to the analysis. Once the spectrum is finally in a satisfactory state, it can then be analyzed to determine the desired parameters such as the chemical shift tensor components and quadrupolar coupling constants. This will be done in Chapters 4 and 5 for the materials of interest.

The initial time-domain FID and resulting frequency-domain spectrum from a deuterium D_2O experiment at 17.6 T is shown in Figure 3.8. Since the two deuterium nuclei in the molecule are identical by symmetry, there is only a single peak in the spectrum. Also, since it is a liquid sample, this ends up being a relatively narrow peak with no asymmetry, arising from molecular tumbling (as explained in Chapter 2). For this reason, D_2O can be useful in optimizing the homogeneity of the B_0 field. Any inhomogeneity in the field will result in a broadened line shape as different regions of the sample would

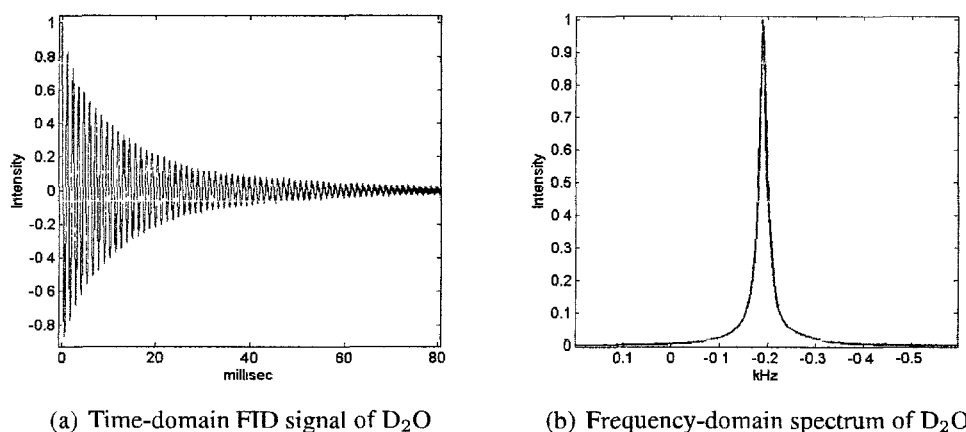


FIG. 3.8: The results of a single 90° pulse experiment on D₂O, observing the deuterium nuclei, before and after applying a Fourier transformation.

be exposed to slightly different field strengths. By adjusting the shim coils until the line width is minimized, any inhomogeneity can be eliminated.

It is also worth noting that the frequency axis in the spectrum is actually offset relative to the carrier frequency, and is not an absolute value. In order to compare the peak positions and other line shape features to other experiments, it is necessary to reference them to a common value. For most nuclei, there is a standard reference material, which is the standard established by IUPAC [19], that can be used to calibrate the frequency axis. For instance, lithium experiments can easily be referenced to aqueous LiCl. Also, the frequency axis can be reported in units of Hertz or parts per million (ppm). This is determined by expressing the chemical shift as defined by,

$$\delta = \frac{\nu - \nu_R}{\nu_0}, \quad (3.4)$$

where ν_R is a reference value that is used to determine the zero of the axis and ν_0 is the operating frequency of the spectrometer for the nucleus being observed. Since the difference in frequencies is on the order of Hertz and the operating frequency of the spectrometer is on the order of MHz, the resulting value is easily expressed in parts per

million. This unit has the benefit of being field-independent, so it makes it easier to compare experiments that were performed at different B_0 field strengths.

Through the use of the equipment and procedures described in this chapter, NMR spectra can be obtained on a wide range of nuclei in many different materials. The high-resolution offered by being able to take measurements at tenths of a microsecond provide enough detail to clearly identify individual sites of a nucleus. This allows NMR to provide invaluable information about the small-scale structure of materials, as well as the dynamics of the atoms, that can lead to observable properties on the macroscopic scale.

CHAPTER 4

A Study of Complex Paramagnetic

Oxides: $\text{Nd}_{\frac{2}{3}-x}\text{Li}_{3x}\text{TiO}_3$

4.1 An Overview of $\text{Nd}_{\frac{2}{3}-x}\text{Li}_{3x}\text{TiO}_3$

Magic angle spinning NMR was used to study a series of materials with the composition $\text{Nd}_{\frac{2}{3}-x}\text{Li}_{3x}\text{TiO}_3$, where $x=0.05, 0.083, 0.116,$ and 0.142 . These materials exhibit a novel nano-checkerboard phase separation between the lithium and neodymium atoms that occurs spontaneously during synthesis. The nano-scale dimensions of the separate lithium-rich and lithium-poor regions can be finely controlled just by varying the concentration of lithium during the initial synthesis. One possible application of this type of material is as a template for creating small, controlled structures on a surface, such as nano-scale circuits for electronic devices.

All of the $\text{Nd}_{\frac{2}{3}-x}\text{Li}_{3x}\text{TiO}_3$ materials have the same basic perovskite crystal structure, as seen in Figure 4.1. The perovskite's atomic structure is denoted by ABX_3 . In the case of $\text{Nd}_{\frac{2}{3}-x}\text{Li}_{3x}\text{TiO}_3$, the A-sites are each either lithium, neodymium, or simply vacant; the B-sites are all titanium; and the X-sites are oxygen. Along the z -axis of the crystal,

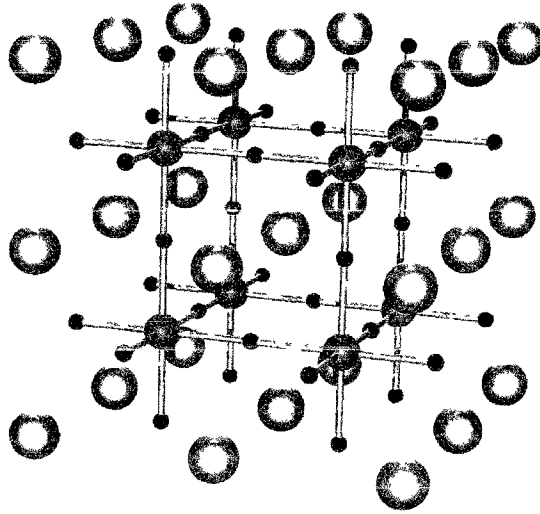


FIG. 4.1: Idealized perovskite crystal structure ABO_3 . The red spheres represent the oxygens, the blue spheres are B-atoms (Ti in the case of $Nd_{\frac{2}{3}-x}Li_{3x}TiO_3$), and the silver spheres are A-atoms (mixture of Li and Nd in $Nd_{\frac{2}{3}-x}Li_{3x}TiO_3$)

there are alternating planes of A-sites and B-sites. The oxygens are distributed throughout the crystal, forming octahedral cages around each of the B-site atoms. The A-site planes alternate between pure-neodymium layers and neodymium-lithium mixed layers. It is in these mixed layers that the phase separation between the lithium and neodymium occurs. The checkerboard-like structure is evident in the idealized crystal structure shown in Figure 4.2 [1]. In the neodymium region of the mixed layer, the neodymium sites are only partially occupied (the fraction occupied is 0.2947 in the case of $x = 0.083$), and it is assumed to be with a random distribution of vacancies. All other sites in the material appear to be 100% occupied [1]. The actual dimensions of the square lithium region are directly dependant upon the bulk lithium concentration, and are shown in the TEM images of several concentrations, with the borders of the lithium regions noted (Figure 4.3). It is worth noting that the checkerboard separation is a macroscopic structural effect not limited to the surface of the crystallite.

With regards to charge distribution, the structure can be divided into two domains: lithium-rich and lithium-poor. These domains are defined by the square lithium regions of

the mixed layer and extend along the z -axis of the structure. This results in the lithium-rich region having the stoichiometry of $\text{Nd}_{1/2}\text{Li}_{1/2}\text{TiO}_3$, while the lithium-poor region is $\text{Nd}_{2/3}\text{TiO}_3$. The net charge of each of these regions is zero. This also supports the idea that the neodymium vacancies are only located in the lithium-poor region of the mixed layer. If vacancies were present in the neodymium-pure layer, the net charge of the lithium-rich region would no longer be neutral.

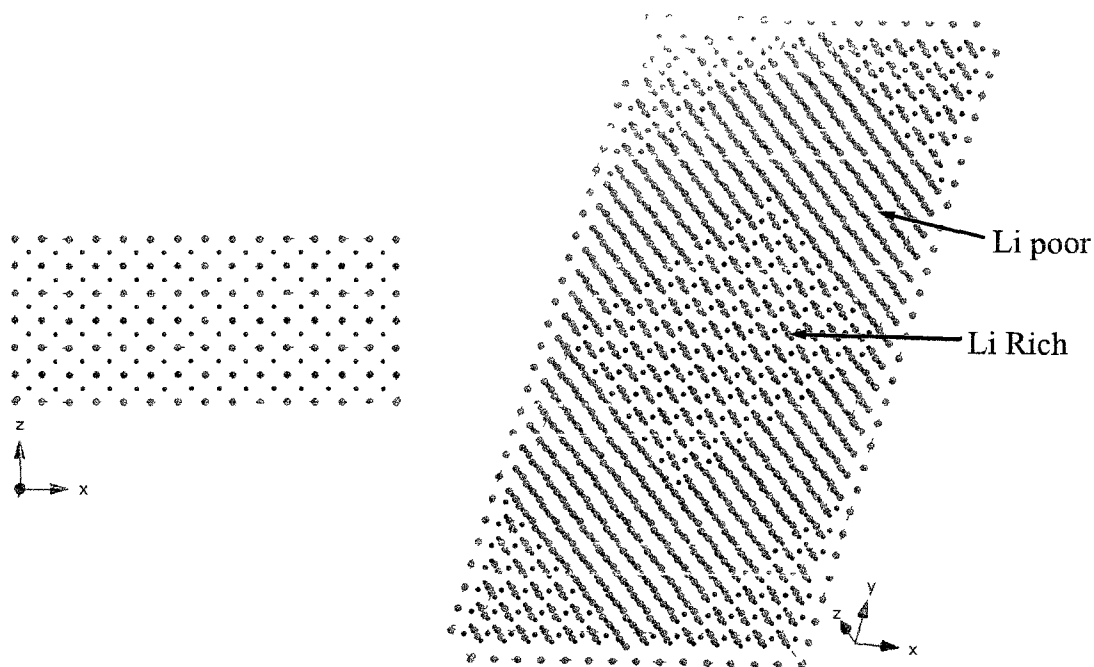


FIG. 4 2: A CrystalMaker™ rendition of a single supercell of $\text{Nd}_{58}\text{Li}_{25}\text{TiO}_3$ (sample 2) viewed from two perspectives [1]. In the Nd/Li-mixed layer, the neodymium sites are 29.47% occupied. (Red=Li, Green=Nd, Blue=Ti, Oxygens are hidden).

A total of four different $\text{Nd}_{\frac{2}{3}-x}\text{Li}_{3x}\text{TiO}_3$ samples were studied as part of this work, each with a different lithium concentration. These samples were all prepared by Professor Peter Davies' group at the University of Pennsylvania, which also performed powder X-Ray diffraction, neutron diffraction, and TEM imaging experiments [1, 2]. The TEM images clearly show the regularity and dimensions of the square lithium regions and how they differ in size with varying lithium concentration. Ideally, the diffraction experiments could be used to determine the exact crystal structure of a sample. However, due to the

large number of atoms per unit cell (over 1000 just for $x = 0.083$), doing this for anything more than a low-concentration sample becomes very time-intensive and impractical to accomplish. This is one of the reasons NMR is a worthwhile addition to the study of these materials. The four samples featured in the NMR study are as follows: sample 1: $x = 0.05$, sample 2: $x = 0.083$, sample 3: $x = 0.116$, and sample 4: $x = 0.142$.

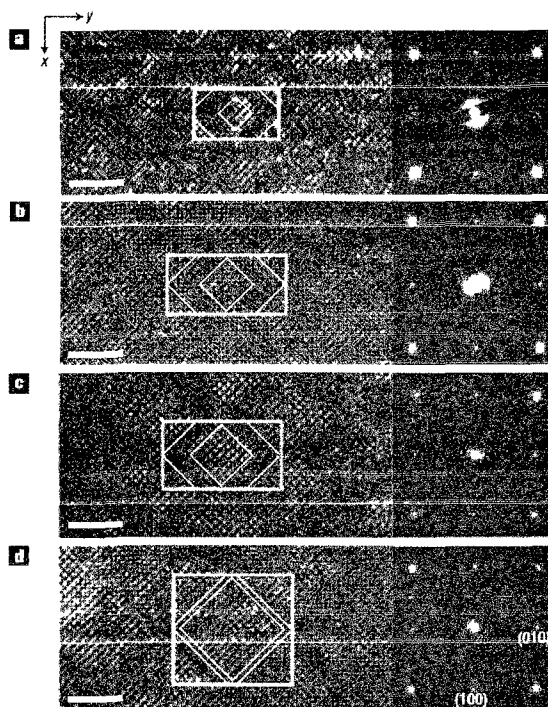


FIG. 4.3: TEM images taken with the electron beam parallel to $[001]$ and their corresponding SAED patterns of grains with nominal compositions $(\text{Nd}_{0.62}\text{Li}_{0.15})\text{TiO}_3$ (a), $(\text{Nd}_{0.58}\text{Li}_{0.25})\text{TiO}_3$ (b), $(\text{Nd}_{0.55}\text{Li}_{0.35})\text{TiO}_3$ (c) and $(\text{Nd}_{0.53}\text{Li}_{0.43})\text{TiO}_3$ (d). Supercells are indicated with a thick outline, where the dimensions are $12 \times 20 a_p$ (a), $14 \times 28 a_p$ (b), $16 \times 26 a_p$ (c) and $26 \times 28 a_p$ (d), as measured from the SAED patterns. Li-rich square domains are indicated with a thin outline. The outlines are intended to guide the eye only – the images do not demonstrate atomically flat interfaces. The scale bars are 5 nm. [1]

The structure for sample 2 (shown in Figure 4.2) was determined by a combination of TEM imagery and powder X-Ray diffraction [2]. Due to the number of atoms in a single unit cell and the difficulty in fitting the diffraction data, sample 2 was the only concentration that a complete crystal structure was available for. For the other concentrations, the dimensions of the unit cell as well as the phase boundaries were determined from the TEM images, but the individual atom locations were not calculated.

4.2 Summary of Experiments

Lithium MAS NMR spectra were recorded for each of the four samples at various temperatures (set temperatures ranging from 220 K to 330 K) and in both 7 T and 17.6 T static fields. Both ${}^7\text{Li}$ and ${}^6\text{Li}$ spectra were obtained, but due to the significantly better signal-to-noise of ${}^7\text{Li}$ over ${}^6\text{Li}$, more extensive data was taken observing the ${}^7\text{Li}$ isotope. However, it is important to understand that ${}^6\text{Li}$ spectra are critical to independently obtain some of the NMR parameters for the structure (this will be addressed later in this chapter). The higher signal-to-noise of ${}^7\text{Li}$ is due mostly to the relative natural abundance of each isotope: 92.58% natural abundance for ${}^7\text{Li}$ compared to 7.42% for ${}^6\text{Li}$.

For the initial experimental tune-up and optimization, an aqueous LiCl solution was used to set the pulse widths and power levels. In addition, the LiCl solution was also used to determine the spectral coverage of the pulse sequences used. This was done by running a series of single-pulse NMR experiments on LiCl with the exact same parameters as was used for the $\text{Nd}_{\frac{2}{3}-x}\text{Li}_{3x}\text{TiO}_3$ experiments, including spectral window and pulse sequence parameters. The carrier frequency offset was then changed incrementally farther away from the LiCl signal, with the change in intensity of the lithium signal with respect to its distance from the carrier noted. This intensity distribution was then used to determine the amount of loss in intensity for portions of the $\text{Nd}_{\frac{2}{3}-x}\text{Li}_{3x}\text{TiO}_3$ spectrum due to the finite pulse width. The envelope generated by this fit was used to scale the simulated line shapes (discussed in Section 4.4) in order to allow them to more accurately be compared to experimental results. The changes in intensity of the LiCl solution ${}^7\text{Li}$ spectrum with respect to the frequency of the carrier are shown in Figure 4.4, and Equation 4.1 shows the scaling factor used on the simulations to account for the finite pulse width, where Δ is the carrier frequency offset in kHz from the resonance frequency.

$$y = -(3.45 \times 10^{-4})\Delta^2 - (4.22 \times 10^{-15})\Delta + 94.3 \quad (4.1)$$

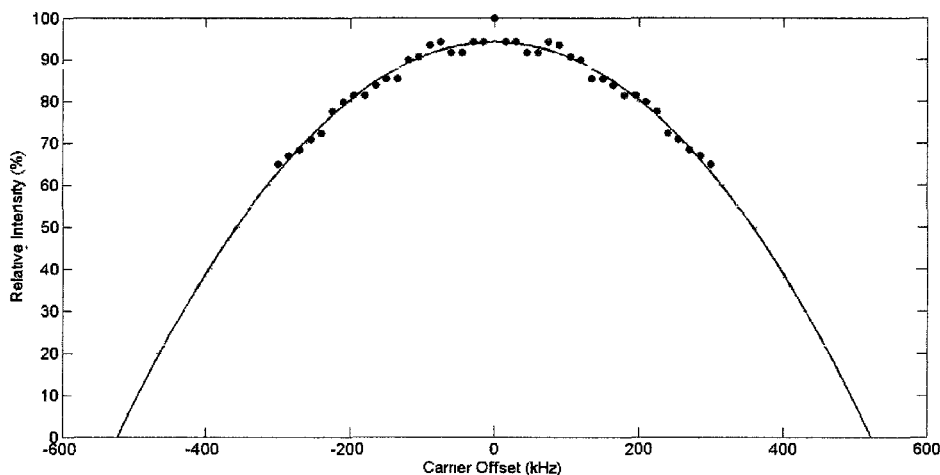


FIG. 4.4: The relative intensities of a series of aqueous LiCl spectra with different carrier frequency offsets. These can be used to correct for the finite pulse coverage observed in a wide spectrum. Acquired after a nominal 90° pulse on exact resonance, with $\omega_1 = 166.667$ kHz.

For the ^7Li spectra, the pulse sequence used was a basic Zero-Go sequence (Figure 3.4), consisting of a single 90° pulse followed by signal acquisition. Most of these experiments had an MAS spin-rate of 30 kHz and used a 2.5 mm rotor. The sample temperature range covered was 277-360 K in the 17.6 T field, while the 7 T experiments were only performed at ambient temperature. At 17.6 T, typical experimental parameters were a pulse width of $1.5 \mu\text{s}$ at 5 dB, recycle delay of 10 ms, and a spectral window of 2 MHz. In the 7 T field, the parameters were the same aside from changing the spectral window to 1 MHz.

The ^6Li experiments utilized a Hahn-Echo pulse sequence (Figure 3.5). Due to the lower resonant frequency of ^6Li , a ZG pulse sequence produced a large amount of electronic ringing in the probe electronics at the beginning of acquisition, making it difficult to obtain an undistorted spectrum. By using an echo pulse, it was possible to move the NMR signal far enough out in time to avoid this recovery problem. Most of these experiments were performed with an MAS spin-rate of 15 kHz in order to provide a sufficient number of spinning sidebands to compare to simulation. Since the overall anisotropy of the tensor is smaller by one-third in the frequency domain than ^7Li (due to the smaller

Larmor frequency), spinning at 30 kHz results in almost all of the anisotropy being eliminated. Having more spinning sidebands allows any resulting fit to the data to be more reliable and accurate. Typical experimental parameters used at both 17.6 T and 7 T fields were a pulse width of 1.5 μs at 5 dB, a recycle delay of 10 ms, and a spectral window of 200 kHz.

In addition to the MAS NMR experiments that comprise the bulk of this study, a series of electron paramagnetic resonance (EPR) experiments were performed by Bruker Biospin in an attempt to investigate the g -tensor values for the paramagnetic interaction. There was also a measurement of the magnetic susceptibility of samples 2 and 4 as a function of temperature in a 7 T Superconducting Quantum Interference Device (SQUID) performed by Ale Lukaszew's lab, covering a range of 5-300 K. The results of both of these additional studies will be discussed in the next section.

4.3 Qualitative Results

The ^7Li spectra acquired at 17.6 T at various temperatures for each of the four available lithium concentrations are shown in Figure 4.5. All of the spectra show three distinct sets of peaks, whose relative intensity changes with lithium concentration. It is easy to distinguish two sets of peaks from visual inspection of the spectrum. Through simulations, which are discussed later in this chapter, it becomes clear that one of these actually consists of two nearly coincident components.

There are noticeable changes in the spectra both as a function of temperature and lithium concentration. With changing temperature, the spectra of each concentration have similar behavior. As the temperature is decreased, the apparent width of the spectrum increases, indicating an increase in the anisotropy ($\Delta\sigma$) of the interaction tensors. Also notable is the fact that the center of mass of the spectrum does *not* change as a function of temperature. This is true for all four samples and over the entire experimentally acces-

sible temperature range. However, the relative positions of the isotropic chemical shift of each of the three component peaks does change with temperature. This leads to considerable spectral overlap making it difficult to distinguish separate sets of peaks at the lower temperatures. Previous NMR experiments on similar paramagnetic materials have observed the same temperature independent behavior of the isotropic shift [28].

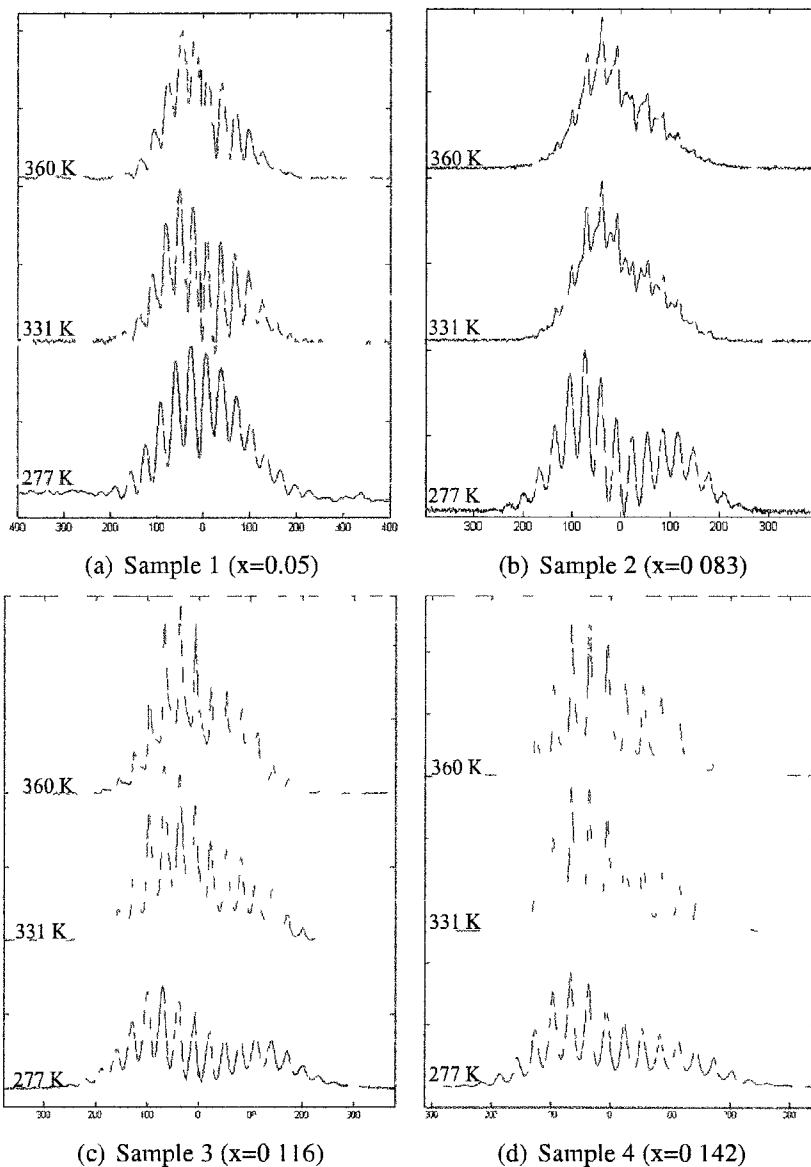


FIG 4.5 ${}^7\text{Li}$ spectra of $\text{Nd}_{2/3-x}\text{Li}_{3x}\text{TiO}_3$ taken at different temperatures with varying Li concentrations (red=360 K, green=331 K, blue=277 K) Frequency axes are in units of kHz

Sample 4 has one dominant set of peaks, with the other two sets visible as lower-intensity shoulders on the sides of the main peaks. As lithium concentration is decreased, the relative intensities of the shoulders increase relative to the major peaks, but with the relative position unchanged when observed at the same temperature. For the lowest concentration, the peaks which were previously the shoulders of the main peak in the high-concentration sample are now the largest peaks of the spectrum, with the previously dominant peaks appearing along the shoulders. By performing experiments at various MAS spin rates, it is possible to identify the center peak for each of the sets and thus, their relative chemical shifts. This demonstrates that the relative intensity of each of the three sets of peaks is changing with concentration, as opposed to their chemical shifts. The loss of signal-to-noise at lower concentrations is a direct result of less lithium in the sample. All of the experimental parameters were kept constant for each of the different concentrations.

In addition to the NMR experiments performed on these samples, a series of electron paramagnetic resonance (EPR) experiments were performed courtesy of Bruker Biospin. The purpose of these measurements was to determine the g -tensor components of the neodymium atoms. The g -tensors are an important component of the point-charge calculations for the paramagnetic interaction (discussed in Section 4.4) and it was hoped that they could be experimentally determined. A typical EPR spectrum is shown in Figure 4.6.

Unfortunately, the EPR spectra are inconclusive. There is a large amount of dipolar and exchange coupling among the unpaired spins; this is an unavoidable consequence of the high concentration of paramagnetic Nd^{+3} ions [29]. Because of this broadening, it is not possible to accurately determine the g -tensor values for the material. For this reason, the point-charge calculations performed in Section 4.4 treat the g -tensor components as free variables in the fits.

Several experiments were also performed in a SQUID. There were two stages to

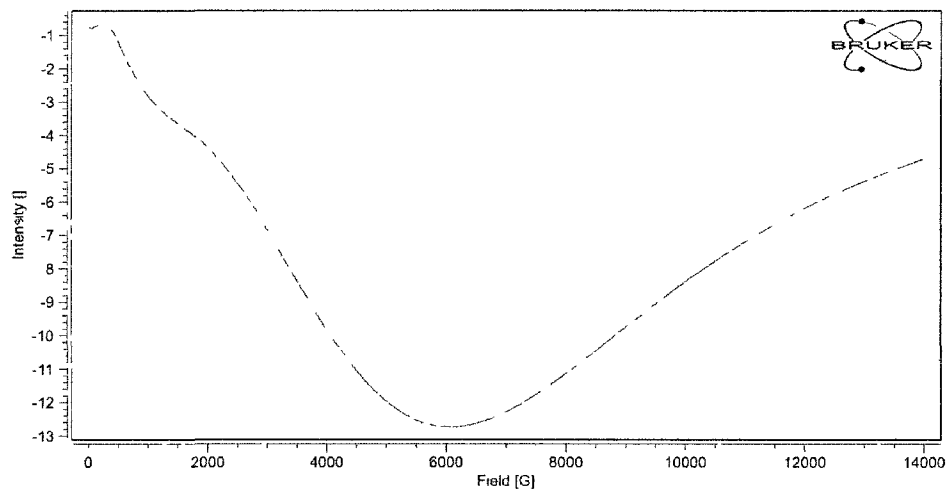


FIG. 4.6: Electron Paramagnetic Resonance spectrum of sample 2 ($x=0.083$) as performed at 70 K by Bruker Biospin [29]. The spectra resulting from these experiments were too broad to determine the g -tensor principal values of the neodymium sites.

these experiments. The first stage kept the sample in a constant magnetic field of 45000 Oe and lowered the temperature to 50 K. The magnetic moment of the sample was measured at each temperature in increments of 5 K, up to room temperature. The results of this experiment for samples 2 and 4 are shown in Figure 4.7.

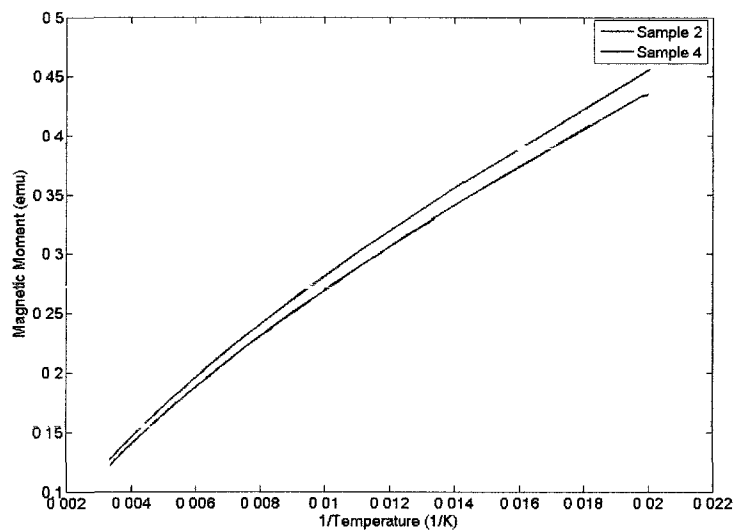


FIG. 4.7: Magnetic susceptibility measurements of sample 2 ($x=0.083$) and sample 4 ($x=0.142$) of $\text{Nd}_{2-x}\text{Li}_{3x}\text{TiO}_3$ at 4.5 T as a function of temperature.

The second part of the SQUID experiments kept the temperature constant (room temperature) while the applied field was varied in a loop from 45000 Oe to -45000 Oe in steps of 5000 Oe. The magnetic moment of the sample was recorded at each step, with the results shown in Figure 4.8.

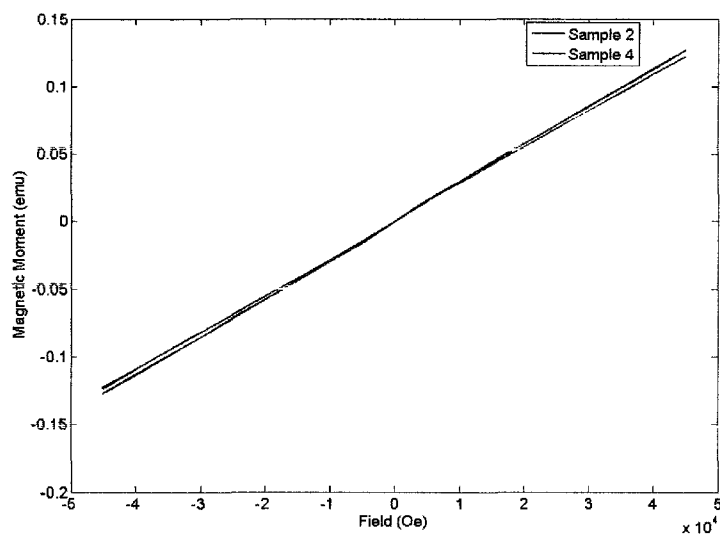


FIG. 4.8: M vs H for sample 2 ($x=0.083$) and sample 4 ($x=0.142$) of $\text{Nd}_{\frac{2}{3}-x}\text{Li}_{3x}\text{TiO}_3$

Unlike the EPR measurements, the SQUID measurements were not intended to provide any specific information about NMR-relevant parameters. The goal was simply to see if there were any “interesting” results or trends that presented themselves as a result. However, it is true that the paramagnetic interaction tensor is supposed to depend on the anisotropy in the bulk susceptibility. The measurements show the expected result for any paramagnetic material [30, 31]. The “normal” temperature-dependence of the electron magnetic moment stands in stark contrast to the temperature *independent* isotropic chemical shift of ^7Li in our samples, and may reflect local anti-ferromagnetic order that is not considered in the model leading to Equation 4.2 shown below.

4.4 Simulating the NMR Spectra

Aside from the Zeeman interaction, the primary interaction present in these samples is the paramagnetic dipole-dipole interaction between the lithium and neodymium atoms. For ${}^7\text{Li}$, there is also an additional contribution from first-order quadrupole effects. For ${}^6\text{Li}$, the quadrupole interaction is weak enough that it can be safely ignored (due to the lower quadrupole moment of ${}^6\text{Li}$). Following the discussion in Chapter 2, the total Hamiltonian for ${}^7\text{Li}$ is

$$\mathcal{H} = \gamma_N B_0 \cdot \mathcal{P}_{en} \cdot I + \frac{C_Q}{2I(2I-1)} \hat{\mathbf{I}} \cdot \hat{\mathbf{V}} \cdot \hat{\mathbf{I}}. \quad (4.2)$$

In order to simulate the spectrum, the equations for the time-dependence of the density matrix (equation 2.11) and the time-domain signal (equation 2.12) are used. The goal is to manipulate Equation 2.11 into a form that can be solved using a Matlab™ ODE solver. The way to do this is to express the Hamiltonian in terms of spherical irreducible tensors in the laboratory frame, the final result of which is [9]

$$H = -I_Z \delta_{iso} + I_Z \sqrt{\frac{2}{3}} R_{2,0}^{PAAA} + \frac{1}{\sqrt{6}} (3I_Z^2 - I \cdot I) R_{2,0}^Q. \quad (4.3)$$

Spherical irreducible tensors of rank two can be constructed from linear combinations of Cartesian vector components, such that they transform under rotation according to the rule given by

$$T_{L,M}^{F1} = \sum_{N=-L}^L T_{L,N}^{F2} D_{NM}^L(\alpha, \beta, \gamma), \quad (4.4)$$

where $\Omega = (\alpha, \beta, \gamma)$ is an Euler rotation that rotates coordinate axes $F2$ into coordinate axes $F1$ using the Wigner rotation matrix D_{NM}^L . Using basic trigonometry for rotation of axes, applied to cartesian vectors $A = (A_x, A_y, A_z)$ and $B = (B_x, B_y, B_z)$ it can be shown that in any axis system,

$$T_{0,0} = -\frac{1}{\sqrt{3}}(A_x B_x + A_y B_y + A_z B_z) \quad (4.5a)$$

$$T_{1,0} = -i(A_y B_x - A_x B_y)/\sqrt{2} \quad (4.5b)$$

$$T_{1,\pm 1} = (A_z B_x - A_x B_z) \pm i(A_z B_y - A_y B_z)/2 \quad (4.5c)$$

$$T_{2,0} = \sqrt{\frac{2}{3}}(A_z B_z - \frac{1}{2}(A_x B_x + A_y B_y)) \quad (4.5d)$$

$$T_{2,\pm 1} = \mp \frac{1}{2}[A_x B_z + A_z B_x \pm i(A_y B_z + A_z B_y)] \quad (4.5e)$$

$$T_{2,\pm 2} = \frac{1}{2}[(A_x B_x - A_y B_y) \pm i(A_x B_y + A_y B_x)]. \quad (4.5f)$$

The second-rank Hamiltonian operators for spin interactions relevant to these simulations are quadrupole coupling and the paramagnetic interaction. Converting the Cartesian forms already shown to scalar contractions of two second-rank spherical irreducible tensors is useful because it simplifies calculating the Hamiltonian matrix elements and it reveals the rotational symmetries explicitly.

Thus in general, we get

$$\mathcal{H} = -\omega_0 I_z + c \sum_{L=-2}^2 \sum_{M=-L}^L (-1)^M R_{L,M}(\alpha, \beta, \gamma) T_{L,-M}, \quad (4.6)$$

where $c = C_Q$ for quadrupoles and $c = \gamma_{L\alpha}$ for chemical shielding and paramagnetic tensors. $T_{L,M}$ are spin operators, and $R_{L,M}(\alpha, \beta, \gamma)$ are lattice variables, which depend on the orientation of the tensor with respect to the external field.

To compute the spectrum, note that $\omega_0 \sim 100$ MHz is typically much larger than $\gamma|\Delta|$ or C_Q . Thus, we retain only the part of the interaction that commutes with I_z (in lab fixed coordinates),

$$\mathcal{H} = -\omega_0 I_z + c[R_{0,0}T_{0,0} + R_{2,0}(\alpha, \beta, \gamma)T_{2,0}]. \quad (4.7)$$

Looking at the quadrupole coupling first, the $R_{0,0}T_{0,0}$ term is independent of orientation, and in the principal axis system that diagonalizes the electric field gradient tensor, we get

$$T_{0,0} = -\frac{1}{\sqrt{3}}(I_x^2 + I_y^2 + I_z^2) = -\frac{1}{\sqrt{3}}I \cdot I \quad (4.8)$$

$$\left(\frac{eQ}{\hbar}\right)R_{0,0} = \frac{e^2Q}{\hbar}(q_{xx} + q_{yy} + q_{zz}) = 0 \quad (4.9)$$

Therefore, for first order quadrupole coupling, we end up with

$$\begin{aligned} \mathcal{H} &= -\omega_0 I_z + C_Q R_{2,0}^{LAB}(\alpha, \beta, \gamma) \sqrt{\frac{2}{3}}(I_z^2 - \frac{1}{2}(I_x^2 + I_y^2)) \\ &= -\omega_0 I_z + C_Q R_{2,0}^{LAB}(\alpha, \beta, \gamma) \left(-\frac{1}{\sqrt{6}}(3I_z^2 - I \cdot I)\right). \end{aligned} \quad (4.10)$$

The tensors represented in the PAS frame can be rotated to the lab fixed frame through the use of [32]

$$R_{2,0}^{LAB} = \sum_{M=-2}^2 R_{2,M}^{PAS} D_{M,0}^{(2)}(\alpha, \beta, \gamma), \quad (4.11)$$

with the $R_{L,M}^{PAS}$ tensors defined as

$$R_{2,0}^{PAS} = \sqrt{\frac{2}{3}}(q_{zz} - \frac{1}{2}(q_{xx} + q_{yy})) \quad (4.12a)$$

$$R_{2,\pm 1}^{PAS} = 0 \quad (4.12b)$$

$$R_{2,\pm 2}^{PAS} = \frac{1}{2}(q_{xx} - q_{yy}), \quad (4.12c)$$

where q_{ii} are the principal components of the quadrupole interaction tensor in the PAS

frame and are defined such that $|q_{zz}| > |q_{yy}| > |q_{xx}|$. In the event of magic angle spinning, which was used for these experiments, an additional Wigner rotation is performed in order. The first rotation is from the PAS frame to the rotor-fixed frame. The second takes the rotor-fixed frame to the lab frame.

Using the Hamiltonian for each energy level, along with the vector V_Q as defined in

$$V_Q = \sqrt{6} \begin{bmatrix} R_{2,2}^{PAS} & R_{2,1}^{PAS} & R_{2,0}^{PAS} & R_{2,-1}^{PAS} & R_{2,-2}^{PAS} \end{bmatrix} \quad (4.13a)$$

$$= \sqrt{6} \begin{bmatrix} \frac{1}{2}(q_{xx} - q_{yy}) & 0 & \sqrt{\frac{2}{3}}(q_{zz} - \frac{1}{2}(q_{xx} + q_{yy})) & 0 & \frac{1}{2}(q_{xx} - q_{yy}) \end{bmatrix} \quad (4.13b)$$

$$= 3q_{zz} \begin{bmatrix} \frac{1}{\sqrt{6}} \frac{(q_{xx} - q_{yy})}{q_{zz}} & 0 & 1 & 0 & \frac{1}{\sqrt{6}} \frac{(q_{xx} - q_{yy})}{q_{zz}} \end{bmatrix} \quad (4.13c)$$

$$= 3q_{zz} \begin{bmatrix} \frac{1}{\sqrt{6}}\eta & 0 & 1 & 0 & \frac{1}{\sqrt{6}}\eta, \end{bmatrix} \quad (4.13d)$$

allows the energy level transitions to be determined. For this particular example of a spin-3/2 system the results are,

$$(E_1 - E_2) = \omega_0 - 3C_Q \begin{bmatrix} \frac{\eta}{\sqrt{6}} & 0 & 1 & 0 & \frac{\eta}{\sqrt{6}} \end{bmatrix} \cdot D \quad (4.14a)$$

$$(E_3 - E_4) = \omega_0 + 3C_Q \begin{bmatrix} \frac{\eta}{\sqrt{6}} & 0 & 1 & 0 & \frac{\eta}{\sqrt{6}} \end{bmatrix} \cdot D \quad (4.14b)$$

$$(E_2 - E_3) = \omega_0. \quad (4.14c)$$

These resulting energy-level transitions can now be used in the differential equation to determine how the density matrix evolves with time. The next step is to address the paramagnetic component of the Hamiltonian. The paramagnetic component is solved similarly to the quadrupole portion, beginning with the Hamiltonian in

$$\mathcal{H} = -\omega_0 I_z + \omega_0 I \cdot \sigma \cdot \hat{z}_{LAB} \quad (4.15a)$$

$$= -\omega_0 I_z + \omega_0 \sum_{L,M} T_{L,-M}^{PARA} R_{L,M}^{PARA}. \quad (4.15b)$$

The spherical tensors in this case are defined as

$$T_{00}^{PARA} = -\frac{1}{\sqrt{3}} I_z \quad (4.16a)$$

$$T_{1,0}^{PARA} = 0 \quad (4.16b)$$

$$T_{1,\pm 1}^{PARA} = -I_x \pm i \frac{I_y}{2} \quad (4.16c)$$

$$T_{2,0}^{PARA} = \sqrt{\frac{2}{3}} I_z \quad (4.16d)$$

$$T_{2,\pm 1}^{PARA} = \mp I_x - i \frac{I_y}{2} \quad (4.16e)$$

$$T_{2,\pm 2}^{PARA} = 0 \quad (4.16f)$$

and

$$R_{00}^{PAS} = -\frac{1}{\sqrt{3}} \omega_0 (\sigma_{xx} + \sigma_{yy} + \sigma_{zz}) \quad (4.17a)$$

$$R_{1,0}^{PAS} = R_{1,\pm 1}^{PAS} = 0 \quad (4.17b)$$

$$R_{2,0}^{PAS} = \sqrt{\frac{2}{3}} \omega_0 (\sigma_{zz} - \frac{1}{2} (\sigma_{xx} + \sigma_{yy})) \quad (4.17c)$$

$$R_{2,\pm 1}^{PAS} = 0 \quad (4.17d)$$

$$R_{2,\pm 2}^{PAS} = \frac{1}{2} \omega_0 (\sigma_{yy} - \sigma_{xx}), \quad (4.17e)$$

resulting in the Hamiltonian

$$\mathcal{H} = -\omega_0 I_z + \frac{1}{3}(\sigma_{xx} + \sigma_{yy} + \sigma_{zz})\omega_0 I_z + \sqrt{\frac{2}{3}} I_z R_{2,0}^{LAB}. \quad (4.18)$$

The relation,

$$\sqrt{\frac{2}{3}} R_{2,0}^{PARA-LAB} = \sqrt{\frac{2}{3}} \sum_{M=-2}^2 R_{2,M}^{PARA-PAS} D_{M,0}^{(2)}(\alpha, \beta, \gamma) \quad (4.19)$$

is then be used to write the irreducible spherical R-tensor in the Hamiltonian in terms of the LAB frame. As with the quadrupolar derivation above, an additional Wigner rotation is necessary if magic angle spinning is used.

Defining the vector V_p as

$$V_p = \sqrt{\frac{2}{3}} \begin{bmatrix} R_{2,2}^{PAS} & 0 & R_{2,0}^{PAS} & 0 & R_{2,-2}^{PAS} \end{bmatrix} \quad (4.20a)$$

$$= \omega_0 \sqrt{\frac{2}{3}} \begin{bmatrix} \frac{1}{2}(\sigma_{yy} - \sigma_{xx}) & 0 & \sqrt{\frac{2}{3}}(\sigma_{zz} - \frac{1}{2}(\sigma_{xx} + \sigma_{yy})) & 0 & \frac{1}{2}(\sigma_{yy} - \sigma_{xx}) \end{bmatrix} \quad (4.20b)$$

$$= \omega_0 \begin{bmatrix} \frac{1}{\sqrt{6}}(\sigma_{yy} - \sigma_{xx}) & 0 & \frac{2}{3}\Delta\sigma & 0 & \frac{1}{\sqrt{6}}(\sigma_{yy} - \sigma_{xx}), \end{bmatrix} \quad (4.20c)$$

allows the energy levels in the lab frame to be simplified to the form

$$E_1 - E_2 = E_2 - E_3 = E_3 - E_4 = (\omega_0 + \delta_{iso}) + V_p \cdot D. \quad (4.21)$$

This can then be included along with the previously determined quadrupolar component in the differential equation to solve for the density matrix.

The net change in energy between levels is determined by adding the contributions from the paramagnetic and quadrupole interactions for each level. At this point, the energy levels are in terms of the principal values of both the paramagnetic and quadrupolar interaction tensors (δ_{iso} , $\Delta\sigma$, η , C_Q , and η_Q). These values are calculated through lattice sums, approximating each nucleus as a point charge, and using the definitions for

the tensors given in Chapter 2. In performing the point-charge calculations, only the paramagnetic neodymium sites are included in the calculation of the paramagnetic interaction tensors, while the electric field gradient calculation necessary to determine the quadrupole tensors includes all atoms present. Additionally, the partial occupancy of the neodymium sites in the mixed layer is taken into account. The model used assumes a random distribution of vacancies among the neodymium sites of this layer, with a random number generator determining whether each individual site is included according to the occupancy rate of 29.47% [1, 2]. Two other models of vacancy distribution were also considered. One was to force the neodymium sites directly next to the lithium-rich domain to be 100% occupied, adjusting the occupancy rate of the other neodymium sites accordingly. This produced no discernable difference in calculated tensor components. The other method attempted was to manually assign vacancies with the intention of spacing them as evenly as possible throughout the neodymium region. This fixed-location vacancy model resulted in a significant change ($\sim 20\%$) in the calculated tensor components and would not fit well with the experimental results.

Density functional theory (DFT) is frequently used to account for electron distributions and provides reasonably accurate values for the tensor components [33, 34]. However, due to the large number of nuclei per unit cell, as well as the relatively complicated electron distributions present around neodymium nuclei, DFT calculations are impractical in this case. Since lithium's outer electrons are s-electrons with a spherical distribution, the point charge approximation seems reasonable. This was verified by comparing point-charge and DFT calculations for the EFG at the location of lithium atoms in both the paraelectric and ferroelectric forms of lithium niobate (LiNbO_3). While the point-charge calculations did not turn out identical to the DFT calculations, they were close enough (i.e., within an order of magnitude) to use in this case where the quadrupole interaction is much smaller than the paramagnetic interaction. This comparison between point-charge and DFT calculations is discussed in detail in Appendix A.

When calculating the line shape for ${}^6\text{Li}$, the Hamiltonian remains the same, except for the omission of the quadrupole term and the different nuclear spin value. The free induction decay signal resulting from an NMR experiment can be calculated using the trace of the density matrix, as shown in

$$s(t) = \text{trace}(\rho(t)I^-) \quad (4.22a)$$

$$= \sum_{j,k} \rho_{jk} \langle k|I^-|j\rangle \quad (4.22b)$$

$$= \sqrt{3}\rho_{12} + 2\rho_{23} + \sqrt{3}\rho_{34}, \quad (4.22c)$$

where Equation 4.22c shows the specific case of a spin-3/2 system.

The time-dependent behavior of the density matrix ρ is determined from the commutator of ρ with the Hamiltonian, as given by

$$\dot{\rho} = i[\rho, \mathcal{H}] \quad (4.23a)$$

$$\dot{\rho}_{jk} = i \sum_l (\rho_{jl}\mathcal{H}_{lk} - \mathcal{H}_{jl}\rho_{lk}) \quad (4.23b)$$

$$\dot{\rho}_{12} = i\rho_{12}(\mathcal{H}_{22} - \mathcal{H}_{11}), \quad (4.23c)$$

with Equation 4.23c giving the result for a specific element of the density matrix. The Hamiltonian used must be evaluated in the lab-frame to properly simulate the observed signal, which is why the Wigner rotations were used to go from the PAS frame to the lab frame. The result is a differential equation of the form,

$$\dot{\rho} = i(ae^{2ikt} + be^{ikt} + ce^{-ikt} + de^{-2ikt} + f)\rho(t) \quad (4.24)$$

This is then solved numerically using the ODE solving routines available in Matlab™, specifically ODE45. Powder averaging is done over several hundred increments in order to account for the various orientations of the tensors in the powder sample. The distribution of powder increments is calculated using routines already present in the EXPRESS software [8]. The resulting signal of each crystallographically unique lithium site is calculated individually. Each FID is then added to produce the simulated signal of the entire system, which is then Fourier transformed to provide the simulated frequency-domain spectrum which is compared to the experimental spectrum.

The Matlab™ functions that actually calculate the time-domain signal were written as a module for the Exchange Program for Relaxing Spin Systems (EXPRESS), a general purpose program developed by Professors Vold and Hoatson for modeling the effects of jump dynamics on a wide class of NMR experiments [8]. The reason for using EXPRESS in this way was that it was convenient to use the existing front-end and data structure organization to set up the simulations and calculate the powder increments. In addition, the processing functions used in EXPRESS were useful in making the time-domain simulation into a form that could be properly compared with experimental data. This includes the Fourier transformation, as well as zero-filling and line-broadening routines. Since the simulations are an ideal situation with no decay, it was necessary to artificially add spin-spin relaxation in the form of exponential multiplication (em) to the time-domain signal. In addition, it was necessary to account for the limited spectral coverage of the pulses by scaling the frequency-domain spectrum by the envelope determined in Equation 4.1.

4.5 Fitting the Simulations to Experiment

Once the simulations were performed, they could be directly compared to the experimental results. There were several steps to this process. First, the simulation was shifted along the frequency axis so that the maxima of the peaks were aligned with those

of the experimental results. This is equivalent to changing the reference frequency for the simulation's frequency axis. Following this, the scale of the simulation was adjusted by multiplying all of the points across the spectrum by a constant factor in order to best match the spectral intensities with the experimental results (which would vary depending on total number of scans, for instance). This scaling factor was varied to give the best possible fit and was uniform across the spectrum in order to maintain the relative intensity of individual peaks. The quality of the fit was determined by the sum of squares of residuals across each peak in the spectrum. The points chosen for the fit were the maximum of each peak as well as several points to either side of the maximum. The resulting sum of the squares of residuals for all of the points chosen was then taken to represent the quality of the fit.

In order to determine the NMR parameters accurately, both ^6Li and ^7Li spectra were fitted. Assuming the proposed crystal structure is accurate for sample 2, a series of lattice sums can be used to calculate both the paramagnetic and quadrupole tensors for each lithium site using the equations of each interaction as shown in Chapter 2, namely Equations 2.34 and 2.42. The paramagnetic interaction depends directly on the g-tensor components of the neodymium electrons. Since the EPR measurements were inconclusive, the three primary components of the g-tensor were left as free parameters in the fitting of the spectra.

Due to the much lower quadrupole moment of ^6Li , the only interactions that need to be taken into account for the simulation are the Zeeman interaction and the paramagnetic interaction. For this reason, it was useful to first fit the ^6Li spectrum and determine the best-fit g-tensor components before attempting to fit the ^7Li experiments. The g-tensor values obtained through these fits were then used in the fits of the ^7Li results, which required incorporating the quadrupole interaction.

While it is possible for different neodymium sites to have different g-tensors, the number of sites present in the material would make this impractical to analyze. Conse-

quently, it is assumed that the difference in g-tensor values between different neodymium sites is negligible. Thus, only three parameters were varied independently, g_{xx} , g_{yy} , and g_{zz} . In order to save on computing time, the lattice sum for the paramagnetic tensor was calculated once with the g-tensor principal values set to one. For each set of principal values being evaluated, the individual elements of the paramagnetic tensor only needed to be scaled by the appropriate factor of g_{xx} , g_{yy} , or g_{zz} . Finally, the tensor was diagonalized to provide the principal values necessary to determine δ_{iso} , $\Delta\sigma$, and η . These values were then used to calculate a spectrum that could be compared to the experimental results. The method for choosing permutations was simply to decide on a range of values for each component (divided into discrete values) and run through each possible permutation. Once approximate values were determined, the range of each component was refined to test a finer distribution of values.

The initial fits were completed on spectra with a temperature set-point close to room temperature so as to have the material in a state as close as possible to the proposed x-ray structure [1]. The actual sample temperature (determined from the calibration described in Appendix B) was approximately 332 K. The values for the g-tensor components were also kept constant between calculations for both the ${}^6\text{Li}$ and ${}^7\text{Li}$ spectra. Through the ${}^6\text{Li}$ fit, it was determined that the best values for the g-tensor of the neodymium electrons are $g_{xx} = 1.48$, $g_{yy} = 0.87$, and $g_{zz} = 1.22$.

The results of simulating the spectra of both ${}^6\text{Li}$ and ${}^7\text{Li}$ of sample 2 at a room temperature set-point are shown in Figures 4.9 and 4.10. The ${}^6\text{Li}$ experiment was performed at only 15 kHz in order to provide more spinning sidebands to increase the accuracy of the fit. The ${}^7\text{Li}$ simulation in this figure also includes the quadrupole interaction, which is not present in the ${}^6\text{Li}$ simulation.

Once the room temperature spectra of sample 2 were satisfactorily fit, the high- and low-temperature spectra were considered. In fitting the other temperatures, all of the parameters of the room temperature fit were kept constant except for the constant in front of

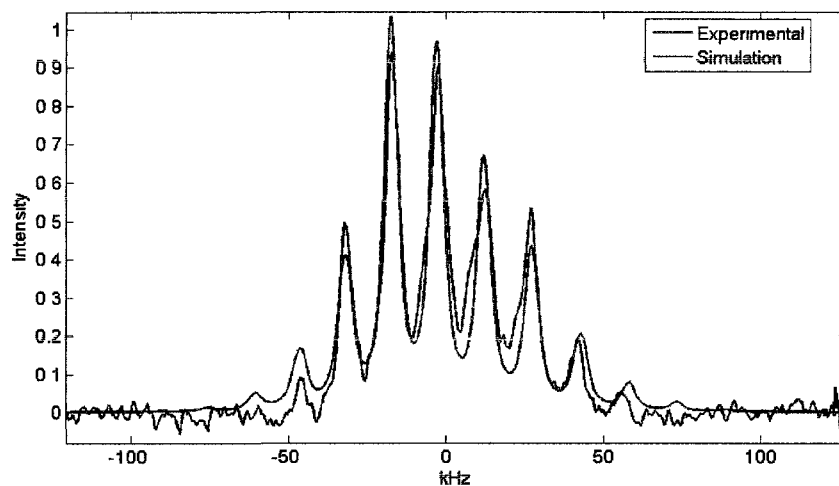


FIG. 4.9: ${}^6\text{Li}$ spectra of $\text{Nd}_{\frac{2}{3}-x}\text{Li}_{3x}\text{TiO}_3$ ($x=0.083$) at $T=320$ K and 15kHz compared to simulation

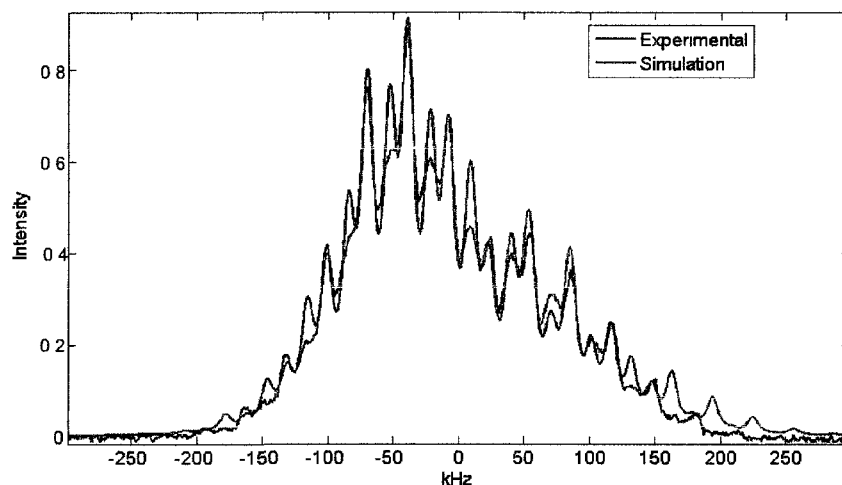


FIG. 4.10: ${}^7\text{Li}$ spectra of $\text{Nd}_{\frac{2}{3}-x}\text{Li}_{3x}\text{TiO}_3$ ($x=0.083$) at $T=331$ K and 30kHz compared to simulation

the paramagnetic tensor, C . This was scaled with the inverse of the sample temperature according to its expected behavior. The results of fitting both a low-temperature and a high-temperature spectrum in this manner are shown in Figures 4.11 and 4.12, respectively.

The high-temperature simulation fits the experiment quite well, comparable to how well the room temperature simulation fit. However, for the low-temperature the fit is

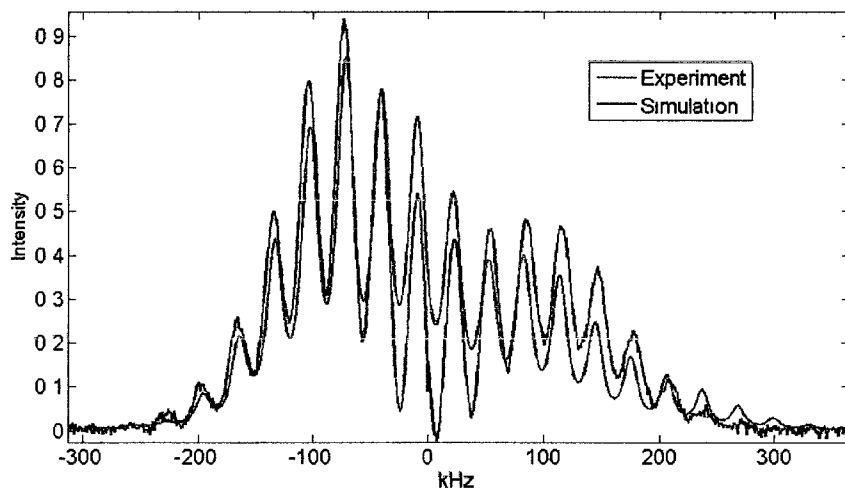


FIG. 4.11: ${}^7\text{Li}$ spectra of $\text{Nd}_{\frac{2}{3}-x}\text{Li}_{3x}\text{TiO}_3$ ($x=0.083$) at $T=277$ K and 30 kHz compared to simulation

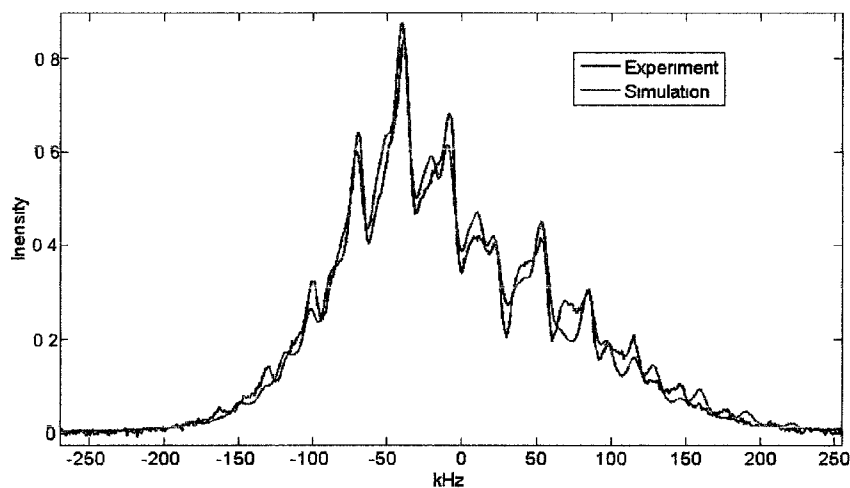


FIG. 4.12: ${}^7\text{Li}$ spectra of $\text{Nd}_{\frac{2}{3}-x}\text{Li}_{3x}\text{TiO}_3$ ($x=0.083$) at $T=360$ K and 30 kHz compared to simulation

noticeably worse. This shows that at lower temperatures, it is not sufficient to scale the paramagnetic term in order to get an accurate fit. A possible explanation for this will be discussed in the Section 4.7.

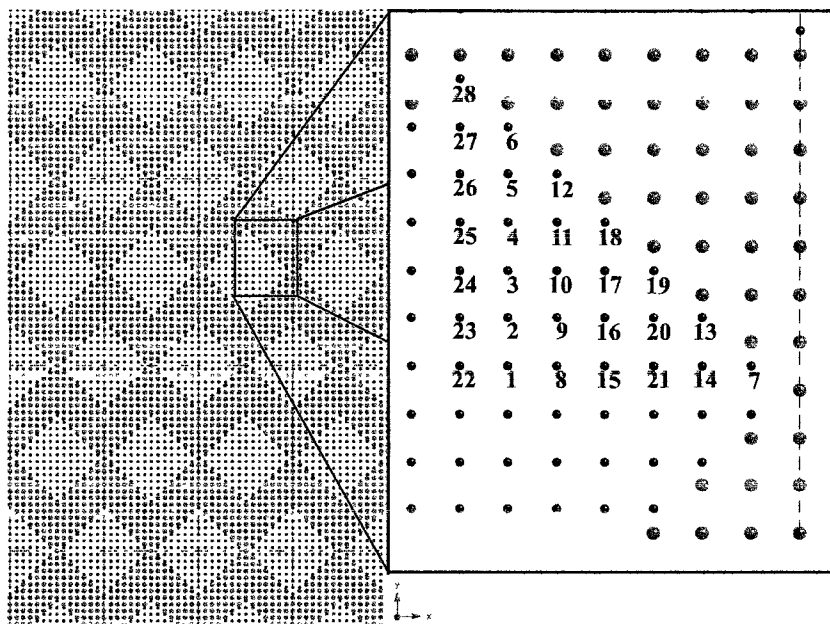


FIG. 4.13: The 28 unique lithium sites of $\text{Nd}_{58}\text{Li}_{25}\text{TiO}_3$ (sample 2). Only the “mixed” layer is shown here, for clarity.

4.6 Quantitative Results of $x=0.083$

As mentioned in the previous section, the values which provided the best possible fit were $g_{xx} = 1.48$, $g_{yy} = 0.87$, and $g_{zz} = 1.22$. While these values are a bit lower than may be expected (usually ~ 2) [35, 36], they are not unreasonably so. These g-tensor values were then kept constant for all of the subsequent ${}^7\text{Li}$ calculations and simulations.

For the initial fits at a sample temperature $T=331$ K for ${}^7\text{Li}$, the paramagnetic and quadrupole tensor components used were the results of the point-charge calculations, with no other adjustments to the values. The resulting tensor components for each for the 28 unique lithium sites in sample 2 are shown in Table 4.1 (see Appendix C for complete tensors), with the sites being labeled according to Figure 4.13. The resulting spectrum using these parameters is compared to the experimental result in Figure 4.10.

The point-charge approximation used for the quadrupole interaction (as demonstrated in Appendix A) is not expected to be exact. However, the order of magnitude of the interaction, as well as the symmetry properties of the model, are correct. Since the

Site Number	δ_{iso} (kHz)	$\Delta\sigma$ (ppm)	η	C_Q (kHz)	η_Q
1	3.3325	-831.3	0.4922	-0.7731	0.4739
2	-0.5768	-807.7	0.5079	-0.418	0.4013
3	-3.4773	-790	0.5183	0.3885	0.5899
4	-7.4509	-766.2	0.5371	-0.1368	0.4402
5	-11.5574	-741.7	0.5589	0.3973	0.1895
6	-15.5388	-717.9	0.5816	-0.6248	0.1827
7	-51.0427	-510.4	0.9324	-1.5066	0.9105
8	3.4567	-832.2	0.4932	-0.5656	0.4973
9	-0.1855	-810.3	0.5079	-3.5128	0.249
10	-3.2228	-791.7	0.5182	-0.9968	0.2902
11	-7.137	-768.2	0.5367	-6.0581	0.2925
12	-11.4743	-742.2	0.5592	-0.7214	0.5508
13	-46.3723	-537.5	0.8689	-2.8349	0.603
14	-50.9951	-510.9	0.9346	0.9891	0.6705
15	3.2617	-831	0.4936	-2.35	0.2253
16	-0.2526	-809.5	0.5048	-2.736	0.3506
17	-3.6621	-788.8	0.5186	2.5697	0.1863
18	-7.9556	-763.3	0.5407	-0.9441	0.1895
19	-42.1661	-561.8	0.815	-3.1864	0.25
20	-46.3522	-537.7	0.8687	-3.0688	0.699
21	-50.8089	-511.8	0.9293	-0.2485	0.3019
22	53.1811	-1169.9	0.5741	-0.4343	0.5395
23	52.4197	-1163.6	0.5666	-0.2368	0.9739
24	50.874	-1152.9	0.5637	0.1922	0.6083
25	49.473	-1142.1	0.5544	0.1936	0.2604
26	49.4399	-1140.3	0.5452	0.2084	0.1053
27	47.9625	-1130	0.5413	0.1934	0.142
28	46.8274	-1121.4	0.5342	1.0201	0.1933

TABLE 4.1: Paramagnetic and quadrupolar tensor components of each site for ${}^7\text{Li}$ in $\text{Nd}_{58}\text{Li}_{25}\text{TiO}_3$ (sample 2) at $T=331$ K. Site numbers refer to labels used in Figure 4.13.

results of the point-charge calculations in this case are quite small (compared to the paramagnetic interaction), the error in their values is negligible in this case. In fact, ignoring the quadrupole interaction entirely shows no appreciable effect on the results of this fit. While the simulation is a good fit to the experimental spectrum, it is not a precise match, which is to be expected. The crystal structure being used for the point-charge calculations is an idealized structure.

From the paramagnetic tensor components (Table 4.1), the 28 unique lithium sites can be easily grouped into three sets based on the values of the isotropic shift and anisotropy. These three sets correspond to the three sets of peaks visible in the spectrum. The lithium sites that fall into each group are shown in Figure 4.14.

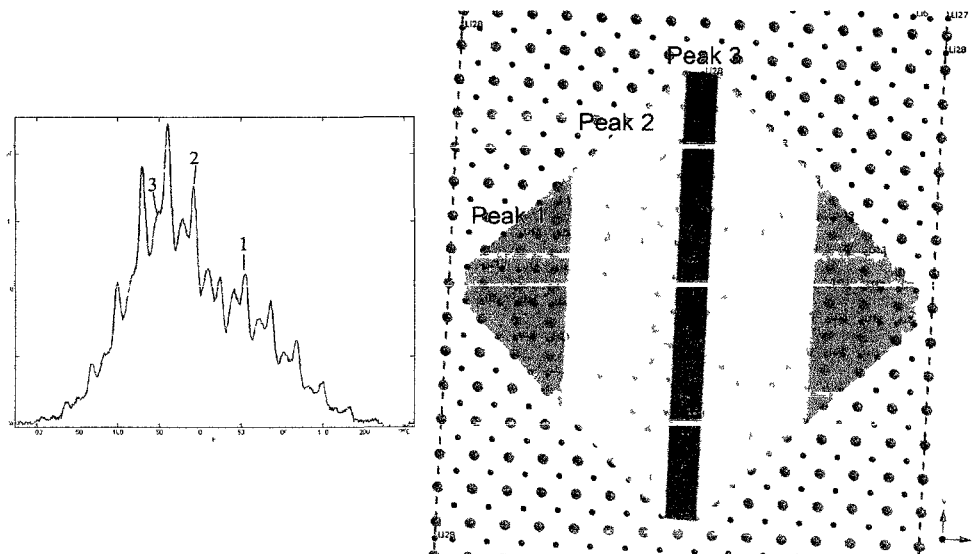


FIG. 4.14: From the parameters generated by the simulations, it is possible to assign each peak in the spectrum to a group of lithium sites in the $\text{Nd}_{2/3-x}\text{Li}_{3x}\text{TiO}_3$ structure. The labels in the spectrum indicate the center peak of each group.

While it is convenient to group the 28 lithium sites qualitatively into three sets, it is insufficient to simply simulate a three-site model with correct relative weights. Within each set of sites, there is still a distribution of tensor components which allows the simulation to fit the experimental spectrum as well as it does. Ignoring this distribution and only using an average set of parameters for each set results in a significantly worse fit.

The temperature-dependence of the anisotropy and isotropic shift [21], based on the fit results for $T=331$ K, are shown in Figures 4.15 and 4.16 respectively. The values of the isotropic shifts are shifted so as to be relative to the average value of all isotropic shifts. This is necessary to accurately line up with the experimental spectrum and is analogous to changing the reference frequency of the spectrum. Both figures also demonstrate the grouping of values that occurs as shown in Figure 4.14.

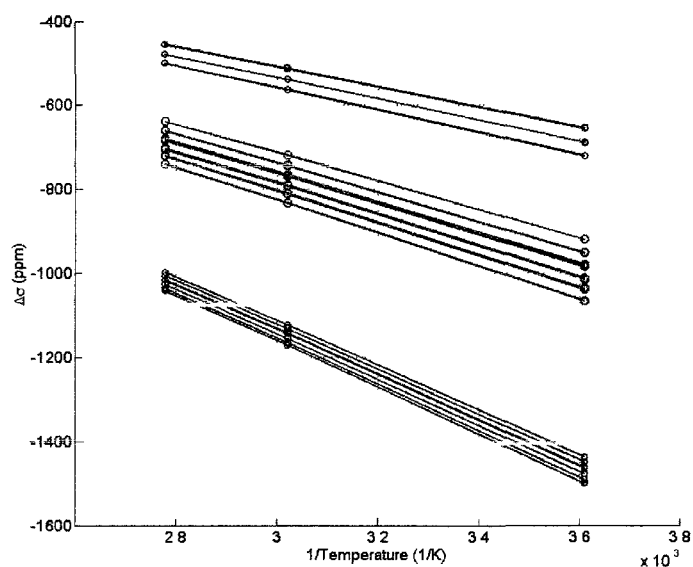


FIG. 4.15: The anisotropy ($\Delta\sigma$) of each of the 28 lithium sites as they are affected by temperature. The colors of the lines represent the three groupings of lithium sites according to the assignments made in figure 4.14, where group 1=Blue, 2=Green, and Red=3

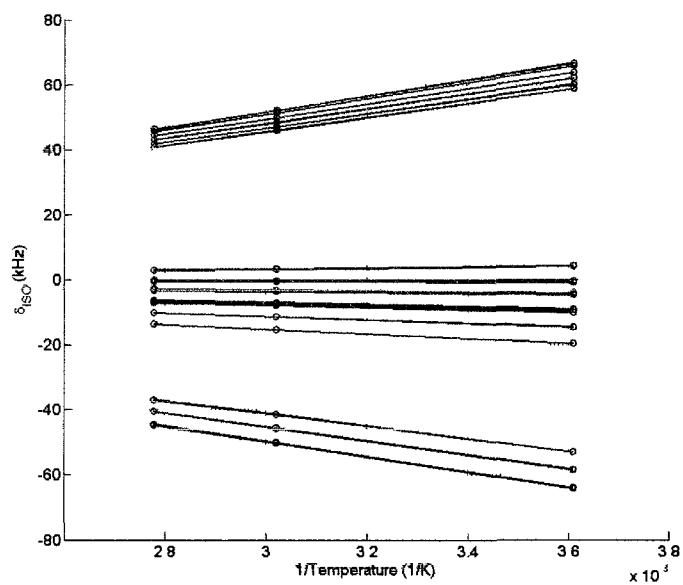


FIG. 4.16: The isotropic shift (δ_{ISC}) of each of the 28 lithium sites as they are affected by temperature. The colors of the lines represent the three groupings of lithium sites according to the assignments made in figure 4.14, where group 1=Blue, 2=Green, and Red=3

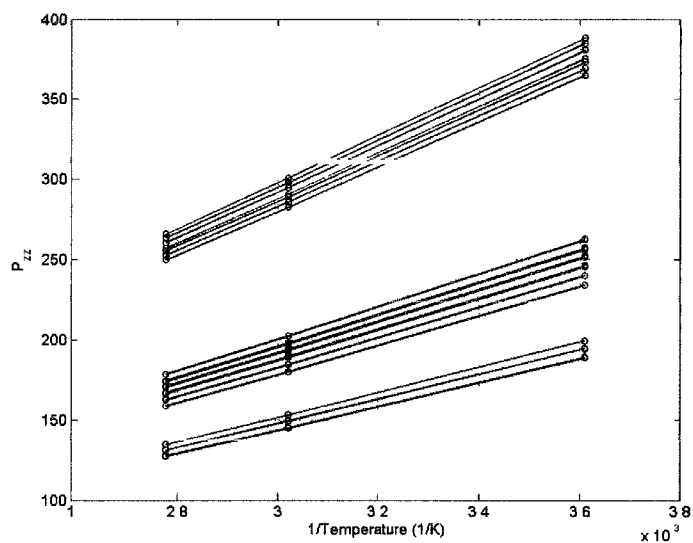


FIG. 4.17: The largest principal value of the paramagnetic interaction tensor (P_{zz}) of each of the 28 lithium sites as they are affected by temperature. The colors of the lines represent the three groupings of lithium sites according to the assignments made in Figure 4.14, where group 1=Blue, 2=Green, and Red=3

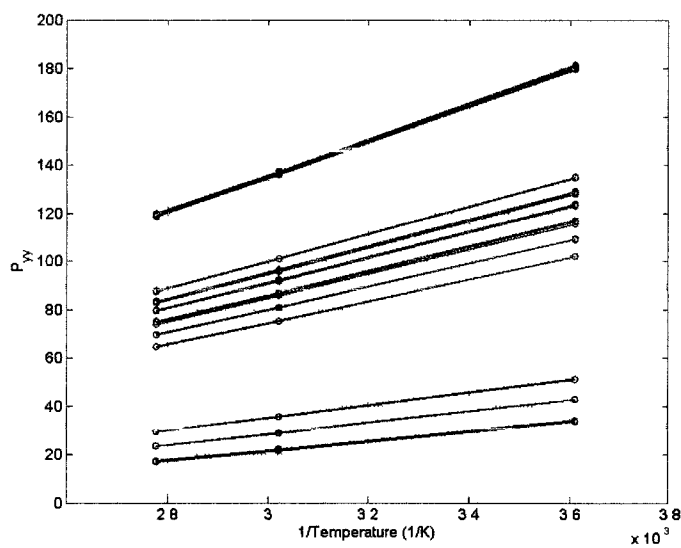


FIG. 4.18: The value of P_{yy} of the paramagnetic interaction tensor of each of the 28 lithium sites as they are affected by temperature. The colors of the lines represent the three groupings of lithium sites according to the assignments made in Figure 4.14, where group 1=Blue, 2=Green, and Red=3

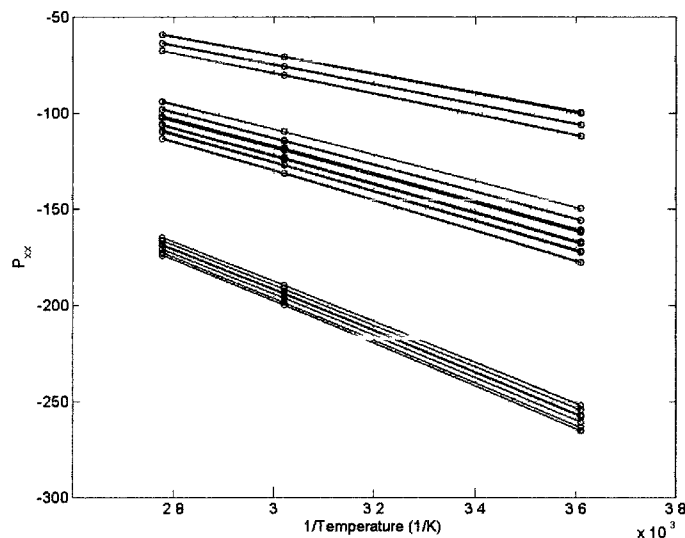


FIG. 4.19: The value of P_{xx} of the paramagnetic interaction tensor of each of the 28 lithium sites as they are affected by temperature. The colors of the lines represent the three groupings of lithium sites according to the assignments made in Figure 4.14, where group 1=Blue, 2=Green, and Red=3

The isotropic shifts show how the largest group of lithium sites (group 2) remains relatively constant, while the other two groups shift in opposite directions with temperature. The paramagnetic interaction tensors' principal components that produce this effect are shown in Figures 4.17, 4.18, and 4.19 for P_{zz} , P_{yy} , and P_{xx} .

Fitting the high-temperature results ($T=360$ K) only required scaling the paramagnetic tensors inversely with temperature, as shown in the expected values for the isotropic shift and anisotropy. No other adjustments needed to be made in order obtain an adequate fit, as shown in Figure 4.12. The low-temperature fit was not as straight-forward. Only scaling the paramagnetic tensor, while leaving the quadrupole tensor unchanged, results in the fit shown in Figure 4.11. The difference between the simulation and the experimental spectrum is significantly worse than the high-temperature fits. There are several potential causes for the poor fit at low temperature.

One likelihood is that there is some distortion to the crystal lattice as a function of temperature. It is not known whether there is any contraction or expansion that may result

in changes to the interaction tensor components. However, the fit is still reasonably close enough that any physical distortion is likely minimal.

The other likely contributing factor to the low-temperature spectrum is suppression of motion in the lithium sites. Each lithium site in the idealized lattice is located at the center of a cage formed by the nearest-neighbor oxygen atoms. The point-charge calculations performed assume that there is no displacement for the lithium site. However, it is very likely that the lithium is displaced towards any one of the nearest-neighbor oxygen sites. There are six possible sites the lithium could be randomly jumping between—one for each neighboring oxygen nucleus. In the high-temperature scenario, this will be averaged by motion and the displacement can be safely ignored. The jump rate will increase as temperature increases, leading to motional averaging that results in the effective quadrupole tensor appearing as if the lithium is at the center position.

When the temperature is lowered, the jump rate will slow down to the point where it no longer averages the result of the displacement. Being displaced from the center of the octahedral cage will result in a larger quadrupole interaction due to the more asymmetric local environment (i.e., larger field gradients). In addition, the asymmetry parameter will also change. The current code for producing the simulations does not take into account displacements and jumping. Therefore, the quality of the low-temperature fit is not expected to be very good. However, it is still possible to examine what effects dynamics have on an individual site.

4.7 Lithium Dynamics in $\text{Nd}_{\frac{2}{3}-x}\text{Li}_{3x}\text{TiO}_3$

The idealized crystal lattice used in point-charge calculations described in Section 4.4 places Li^+ cations in A-sites of nominal cubic symmetry, i.e., at the centers of undistorted octahedral cages defined by the six nearest O^{2-} anions. In this model, finite electric field gradients at the Li nuclear positions arise exclusively from the broken symmetry arising

from the random introduction of Li^+ , Nd^{3+} , and vacancies in nearby A-sites. The relevant internuclear distances are much larger than the nearest neighbor $\text{Li}^+ - \text{O}^{2-}$ distance, so the calculated nuclear quadrupole coupling constants for ^7Li are quite small, on the order of a few kilohertz (See Table 4.1).

However, numerous X-ray and neutron scattering [1, 2] experiments reveal that the Li^+ cations are located at sites of lower symmetry, off-center from distorted octahedral cages. Tables C.4 and C.5 show the results of a representative point charge calculation in which the Li^+ cations in each of the 28 crystallographically distinct sites were displaced by $\pm 1.5 \text{ \AA}$ along Cartesian axes. As expected, some of the distorted sites (presumably, those which involve a close encounter between Li^+ and O^{2-}), exhibit quadrupole couplings as large as $\sim 250 \text{ kHz}$. No such values are found in fits to the experimental ^7Li NMR spectra. For example, an adequate fit to the spectrum of sample 2 ($x=0.083$), obtained at $T = 331 \text{ K}$, is obtained with quadrupole coupling constants on the order of 3 kHz .

Although the unit cell is too large to permit the design and testing of detailed models that incorporate distorted lattices, there is no doubt that the observation of very small quadrupole coupling constants for nominally off-center lithium ions is due to ionic motion. Note that ion migration from cage to cage, which leads to significant bulk conductivity in materials such as $\text{Li}_{0.3}\text{La}_{0.567}\text{TiO}_3$ [37], is too slow to measure in the paramagnetic $\text{Nd}_{\frac{2}{3}-x}\text{Li}_{3x}\text{TiO}_3$ samples. Instead, random “rattling” motions within the confines of a single, distorted octahedral cage can reduce the large electric field gradients expected for off-center ^7Li cations. The temperature-dependent NMR line shapes shown in Figure 4.5 provide support for this hypothesis. It can be seen that as temperature is lowered from 360 K to 277 K , the overall barycenter of the spectra scarcely change, while the spans (edge-to-edge distance) increase by more than the amount expected on the basis of $1/T$ scaling for each paramagnetic tensor. Moreover, there is a significant broadening of the individual sidebands at low temperature, accompanied by slightly lower signal to noise

ratio.

Attempts to account for the observed temperature dependence were made using EXPRESS. An obvious model, entirely consistent with the point-charge calculations, consists of defining seven orientational “sites” defined by the computed paramagnetic tensors for each of the 28 distorted crystallographic configurations specified, for example, in Tables 4.2 and 4.3. These seven sites are “connected” by sudden jumps, at rate k , that correspond to ion motion from site to site. Note that site orientations in this model are defined by Euler angles derived from the 3×3 Cartesian rotation matrices that diagonalize the relevant paramagnetic tensor. Thus, potentially large-angle rotational jumps “connect” sites that also differ in their isotropic and anisotropic paramagnetic tensor principal components. For purposes of calculating the site-dependent electric field gradient tensors, it is also necessary to specify their relative orientations with respect to the paramagnetic tensors. Thus, for each of the 28 crystallographic configurations, the seven-site model depends on no less than 78 independent variables. These consist of one jump rate, and for each of seven sites, three Euler angles defining the orientation of principal axes of the paramagnetic tensor, three more to define the relative orientation of the site-dependent electric field gradient tensor, three principal components of the paramagnetic tensor, and two principal components of the (traceless) electric field gradient tensor. EXPRESS handles most of the labor involved in defining these parameters, and then integrates equations of motion [38] that account both for coherent time dependence of the site frequencies induced by magic angle spinning, and random site-to-site jumps, summed over a sufficient number of randomly oriented crystallites to generate the spectrum expected for a polycrystalline powder sample.

The final line shape could then be obtained simply by adding the line shapes for the 28 crystallographic configurations. Clearly, there are far too many potentially adjustable parameters in this model to warrant any serious attempt at fitting to experimental data. Nevertheless, it is instructive to examine the results for a representative crystallographic

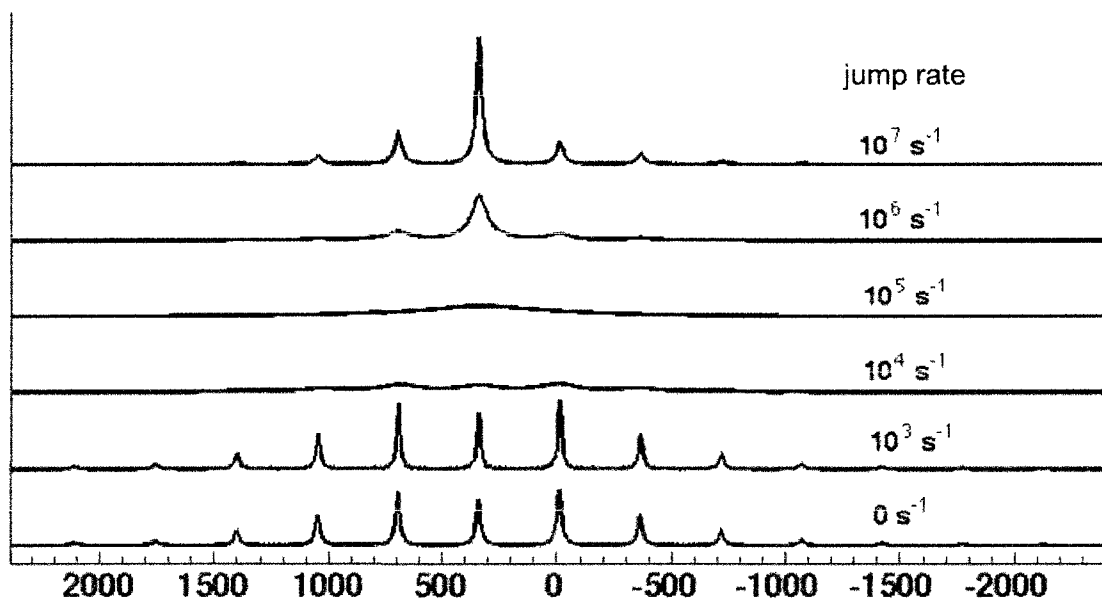


FIG. 4.20: Simulated MAS spectra of ${}^7\text{Li}$ in $\text{Nd}_{58}\text{Li}_{25}\text{TiO}_3$. Spin rate 30 kHz, Larmor frequency 291.47 MHz. Intra-cage “rattling” motion at rates between 0 and 10^7 s^{-1} is incorporated by methods described in the text.

configuration, as shown in Figure 4.20.

Site orientation and principal tensor components used to generate the line shapes in Figure 4.20 are summarized in Tables 4.2 and 4.3. These were generated from the Cartesian tensors for crystallographic site number 13 (as defined in Figure 4.13), by equating the orthogonal 3×3 matrix that diagonalizes the relevant tensor, element by element, to standard expressions for the 3×3 matrix that defines an Euler rotation. [The standard convention in NMR defines the second rotation (angle β) to be counter-clockwise positive about the y -axis [39]]. Crystallographic site 13 was chosen for this simulation because it revealed the largest dispersion of quadrupole coupling constants, ranging from -92.2 kHz to $+256.1$ kHz (see Table 4.3). It should be noted that the line shape is invariant to the sign of the quadrupole coupling constant in absence of motion, but motion that leads to a change in sign will have a profound effect.

Using EXPRESS, “rattling” motions of Li^+ cations can be modeled by sudden site-to-site jumps at an average rate k , such that the average lifetime in any given site is $1/(7k)$.

The bottom line shape in Figure 4.20 was generated with jump rate zero. This spectrum is a simple superposition of line shapes from the seven sites, summed over several thousand random crystallite orientations. In this limit, the site-specific tensor orientations do not matter, and site-specific differences between the tensor components are too small to be resolved as separate peaks within each rotational echo.

As the jump rate increases, the rotational echoes begin to broaden, and when the jump rate becomes comparable to the MAS spin rate ($2\pi \times 30 \text{ kHz} \sim 2 \times 10^5 \text{ s}^{-1}$), the spectrum almost disappears. This occurs because the random jumps, which now occur at least once (on average) during each rotor cycle, drastically interfere with the formation of rotational echoes. This behavior is at first glance surprising, since the dominant (paramagnetic) interaction constants are, according to Table 4.2, quite similar for all seven sites. However, the paramagnetic tensor orientations are strongly site-specific and the random jumps from site to site therefore produce large, sudden changes in the orientation-dependent spin precession frequencies. At faster rates, such that many jumps occur on average during each rotor cycle, the spins precession during each rotor cycle can be envisioned as responding to a single interaction tensor, averaged over all seven sites. Thus, in this limit of fast motion, the rotational echoes become sharp again, and define the line shape of a motionally-narrowed tensor.

Experimental temperature-dependent line shapes (see Figure 4.5) do not exhibit a large loss of intensity over the experimentally accessible temperature range. It may therefore be concluded that the rattling motion does not involve large-angle jumps; presumably, the off-center distortions are significantly smaller than the 1.5 \AA values that were used to generate Figure 4.20.

The computations described above are lengthy and intricate. Before attempting to (semi-quantitatively) estimate a realistic set of distortions such that point-charge calculations produce acceptably small-angle jumps, it is worth examining a simpler model that may provide an estimate of what angular jump sizes are required to reproduce the ex-

Site	Displacement ¹	α^2	β	γ	δ_{iso}	$\Delta\sigma^3$	η_σ
1	x, y, z	276.8	144.2	8.0	99.46	-511.6	0.97
2	x +1.5	15.80	93.9	271.3	99.57	-512.1	0.96
3	x - 1.5	142.1	154.0	318.0	97.37	-503.3	0.99
4	y -1.5	209.1	76.2	262.5	100.82	-519.5	0.97
5	y-1.5	347.7	106.5	269.0	97.94	-503.6	0.96
6	z +1.5	147.2	137.0	252.5	98.84	-508.9	0.97
7	z-1.5	314.1	127.0	177.9	99.15	-510.4	0.97

TABLE 4.2: Site-specific parameters for off-center ^7Li paramagnetic tensors computed by point-charge methods described in the text.

¹The undistorted coordinates for Li^+ (site 1) are denoted by x,y,z; data in this table is for crystallographic site 13 (as defined in Figure 4.13). Displacements by 1.5 Å along x, y, or z directions define sites 2 - 7.

²Euler angles (α , β , γ) rotate the paramagnetic tensor principal axes for each site into coincidence with the ^7Li electric field gradient tensor principal axes for that site (see Table 4.3).

³The isotropic shift δ_{iso} , anisotropy $\Delta\sigma$ and asymmetry parameter η_σ are derived from the eigenvalues of the 3×3 paramagnetic tensor using standard IUPAC (Haeberlen) conventions for chemical shielding tensors. Units are ppm except for η_σ which is dimensionless.

Site	Displacement ¹	α^2	β	γ	C_Q	η_Q
1	x, y, z	82.4	94.6	179.7	-2.85	0.60
2	x +1.5	98.7	4.0	3.5	+3.31	0.60
3	x - 1.5	98.0	72.9	269	-92.23	0.09
4	y +1.5	269.9	15.6	359.7	+256.07	0.04
5	y+1.5	121.2	16.5	8.9	+2.25	0.54
6	z +1.5	133.0	50.0	235.2	+0.7	0.63
7	z+1.5	170.9	91.6	313.7	+3.83	0.11

TABLE 4.3: Site-specific parameters for off-center ^7Li quadrupole coupling tensors computed by point-charge methods described in the text.

¹The undistorted coordinates for Li^+ (site 1) are denoted by x,y,z; data in this table is for crystallographic site 13 (as defined in Figure 4.13). Displacements by 1.5 Å along x, y, or z directions define sites 2 - 7.

²Euler angles (α , β , γ) rotate the ^7Li electric field gradient tensor principal axes for each site into coincidence with a crystal-fixed reference axis system.

³The quadrupole coupling constant, C_Q , and asymmetry parameter η_Q are derived from the eigenvalues of the 3×3 EFG tensor using standard IUPAC (Hahn) conventions. Units of C_Q are kHz.

Site(Q)	α	β	γ	$C_Q(\text{kHz})$	η_Q	
1	0	0	0	3.0	0	
2	180	90	90	3.0	0	
3	90	90	0	25.0	0	
Site(P)	α	β	γ	δ_{iso}	$\Delta\sigma$	η_σ
1	0	0	0	0	550	0.6
2	-90	-70	-180	5	560	0.6
3	0	-70	-90	10	540	0.6

TABLE 4.4: Site-specific parameters for a heuristic model of tensor interactions in a distorted perovskite lattice.

perimental line shapes. Such a model must account for the experimental observations 1) the overall span of the experimental spectrum increases significantly at low temperatures, without dramatic loss of intensity 2) high temperature spectra can be fit with very small quadrupole coupling tensors, on the order of a few kHz, while low temperature spectra can be fit better with quadrupole coupling tensors on the order of 20-30 kHz and 3) the first moment (“barycenter”) of the spectrum is essentially independent of temperature. Qualitatively, all three features can be reproduced in the framework of a simple, three-site model, with site-specific parameters listed in Table 4.4.

As before, the Euler angles for paramagnetic interactions (P) rotate the paramagnetic tensor principal axis frame for each site into coincidence with the quadrupole coupling tensor (Q) for that site. Thus, in site 1 the two tensors are exactly coincident. Since the inverse of a rotation (α, β, γ) is just $(-\gamma, -\beta, -\alpha)$, it is evident that the paramagnetic tensors for sites 2 and 3 are coincident, and rotated only slightly from that for site 1, through Euler angles $(0, 20, 0)$. On the other hand, the site angles chosen for the quadrupole coupling tensor place each of its principal components along x , y and z axes with equal probability, so that the fast-limit average tensor would be exactly zero if all three principal components were equal. The principal values listed in Table 4.4 were chosen to correspond roughly to values that fit the experimental spectra at low and high temperatures. Principal values for site-specific paramagnetic tensor principal components were also selected to roughly

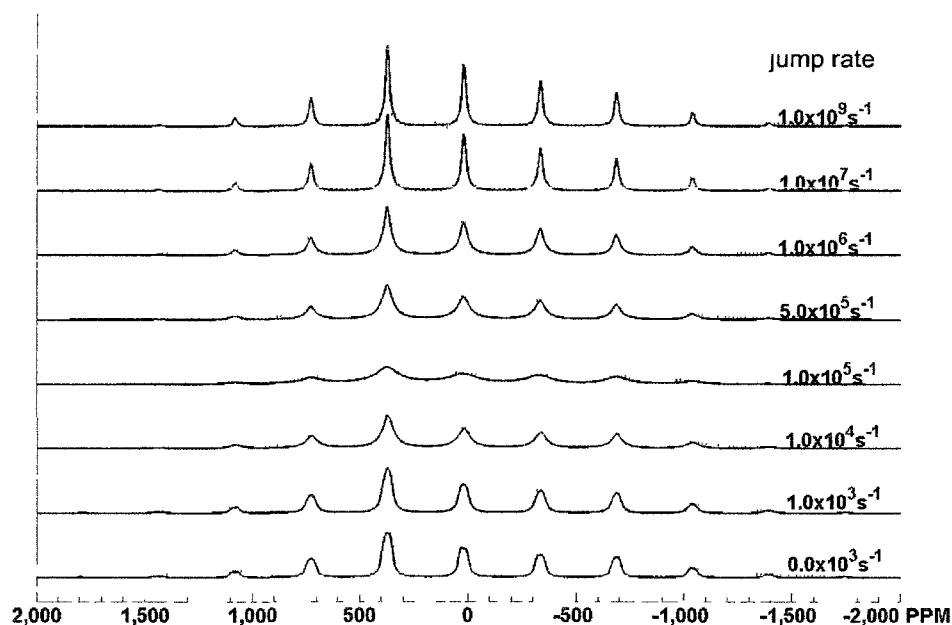


FIG 4.21 Simulated MAS spectra of ${}^7\text{Li}$ in $\text{Nd}_{2-x}\text{Li}_{3x}\text{TiO}_3$ using tensor parameters defined in Table 4.4

match the experimental spectra, with the arbitrary reference frequency set to zero at the middle of the spectrum.

Line shapes for this model, simulated as a function of jump rate, are shown in Figure 4.21. The red dashed lines are spline fits to the echo maxima, meant to outline the powder pattern traced by the envelope of sideband maxima. As expected for small-angle jumps, there is much more intensity at intermediate jump rates than for the large-angle jumps featured in the seven-site model. The asymmetric shape of the envelope, preserved at all jump rates, arises from the choice of $\eta_\sigma=0.6$ for all sites. It is encouraging that the point-charge (seven site) model with large distortions yields essentially equal values for this parameter in all sites.

It can be concluded from these simulations that small off-center displacements of the Li^+ cations can lead to sufficiently small reorientations of the paramagnetic tensor to account at least qualitatively for the temperature-dependent line shapes, and the time scale

for jumps among the off-centered positions is on the order of 10^6 s^{-1} at room temperature. It is worth noting that point-charge calculations of the ${}^7\text{Li}$ EFG tensor are very sensitive to the distance between ${}^7\text{Li}^+$ cations and neighboring O^{2-} anions, while the paramagnetic tensor depends only on the more distant Nd^{3+} ions. It remains to be seen whether carefully chosen directions for small ion displacements can approximately reproduce the tensor components listed in Table 4.4.

4.8 Conclusion

The NMR study of these $\text{Nd}_{\frac{2}{3}-x}\text{Li}_{3x}\text{TiO}_3$ materials supports the previously completed crystallographic work, demonstrating the fine structural control possible through adjustment of the lithium concentration of each sample. It has also been observed that there is no visible phase transition occurring with changing temperature. While the spectra do change with temperature, as is to be expected based on the interactions present, there are no sudden changes as temperature is varied over the $\sim 100 \text{ K}$ range observed. The structure of the materials with respect to the lithium/neodymium phase separation appears to remain intact.

The use of point-charge calculations to determine the lithium paramagnetic and quadrupole interaction tensors in the $\text{Nd}_{.58}\text{Li}_{.25}\text{TiO}_3$ (sample 2) material has allowed for accurate simulations of the experimental spectra at high temperature. While the low-temperature simulations are not accurate to the degree of the high-temperature ones, they still demonstrate the temperature-dependence of the paramagnetic tensor components quite well. It is clear from the qualitative results, and supported by the point-charge calculations, that the peaks in the spectrum can be grouped into three sets. While the overall center of mass of the spectrum is unchanged with respect to temperature, the relative position of the three isotropic shifts does change. Also, the anisotropy of the interaction scales inversely with temperature as expected for the paramagnetic tensor.

The results of the simulations for sample 2 of the $\text{Nd}_{\frac{2}{3}-x}\text{Li}_{3x}\text{TiO}_3$ materials allows for some extrapolation as to what is seen in the spectra of the other samples. Even at other lithium concentrations, there are still three visible sets of peaks, with similar differences in isotropic shifts. This suggests that the model of three sets of lithium sites still holds at other concentrations, with only the relative populations of each of the groups changing. This explains the observation that the “shoulders” on sample 2 become the most prominent peaks of the high-concentration sample 4, based on isotropic position. It also explains how each sample appears to have the same temperature-dependence with respect to the changing isotropic shifts and anisotropy of the peaks.

CHAPTER 5

Study of High-Dielectric Microwave Ceramics

5.1 Overview of High-Dielectric Microwave Ceramics

The use of oxide dielectrics is of great importance to microwave wireless communications, specifically mobile telecommunications. They allow both the size and cost of components such as frequency filters and oscillators to be reduced significantly. In order to be useful materials, they must satisfy several criteria: have a high dielectric constant, low dielectric loss in the microwave region, and temperature stability of its resonant frequency [3–5].

Previous work on these materials by Professor Peter Davies' group has been focused on trying to understand what aspects of their structure and chemistry allow for optimum performance as microwave ceramics; specifically, the role of cation disorder. For this reason, NMR spectroscopy can prove to be a useful addition to other methods of studying the materials. NMR can aid in elucidating structure information as well as potentially providing information on dynamics in the systems through the behavior of the $T_{1\rho}$ relaxation

rates.

Work was done on a pair of high-dielectric microwave ceramics in order to supplement previous studies that had been performed by Daniel Pechkis [40] as well as Peter K. Davies at the University of Pennsylvania [3–5]. In particular, the ^7Li T_{1z} relaxation times of $\text{Ca}(\text{Li}_{1/3}\text{Nb}_{2/3})\text{O}_3$ and $(\text{Ca}_{2/3}\text{La}_{1/3})(\text{Li}_{1/3}\text{Nb}_{2/3})\text{O}_3$ with respect to temperature were studied. There were also some observations of the niobium nucleus in both materials.

Like the $\text{Nd}_{\frac{2}{3}-x}\text{Li}_{3x}\text{TiO}_3$ samples discussed in Chapter 4, these microwave ceramics also feature a perovskite structure, ABO_3 (see Figure 4.1). All of the materials in this series feature a mixture of lithium and niobium in the B-site, while the A-site contains earth metals [3]. For the two specific samples examined in this chapter, the A-sites are entirely calcium for one of the samples and a two-to-one mixture of calcium and lanthanum in the second.

5.2 Summary of Experiments

^7Li MAS NMR spectra of both $\text{Ca}(\text{Li}_{1/3}\text{Nb}_{2/3})\text{O}_3$ and $(\text{Ca}_{2/3}\text{La}_{1/3})(\text{Li}_{1/3}\text{Nb}_{2/3})\text{O}_3$ were recorded in the 17.6 T field over a temperature range of 240 K to 330 K. Most experiments were performed with an MAS spinning speed of 8 kHz in a 4 mm MAS probe. A typical 90° pulse had a width of $5.5 \mu\text{s}$ and a power level of 5 dB, with a recycle delay of approximately 30 seconds to one minute. The actual recycle delay used was adjusted to be approximately three times the observed relaxation time.

In addition to basic single-pulse experiments, T_{1z} saturation-recovery experiments were also run under MAS conditions (as described in Section 3.2). The saturation pulse train typically used thirty 90° pulses spaced $5 \mu\text{s}$ apart, with the same pulse power and duration as for the single-pulse experiments. In order to record a well-defined recovery curve, the delay list used in the T_{1z} experiments varied with temperature and approximate T_{1z} value. Once a rough estimate of the relaxation time was determined (using a series

of short Zero-Go experiments with varying recycle delays), a delay list containing ten to twelve values was constructed that would give an even distribution of points along the recovery curve, an example of which is shown in Figure 5.1.

Once the complete set of spectra was obtained, analysis was performed using a Matlab™ package developed by Professor Robert Vold (initially “view1d”, later revised to “nmrlv”). The spectrum resulting from the “infinity” value of the delay list (the longest delay) is used in order to determine the amount of left shift and phase correction necessary to produce an absorption spectrum. Identical left shift and phase corrections are applied to all other partially relaxed spectra.

The value of T_{1z} is determined on a point-by-point basis. For each point across the peak, the amplitude relative to the infinity value is plotted as a function of delay value to produce a recovery curve as shown in Figure 5.1. The points are fit to an exponential function to determine the value of the relaxation rate (see Equation 2.7) for that position in the spectrum. The error in the T_{1z} value of the peak is determined by performing the same fit for a range of points across the width of the peak.

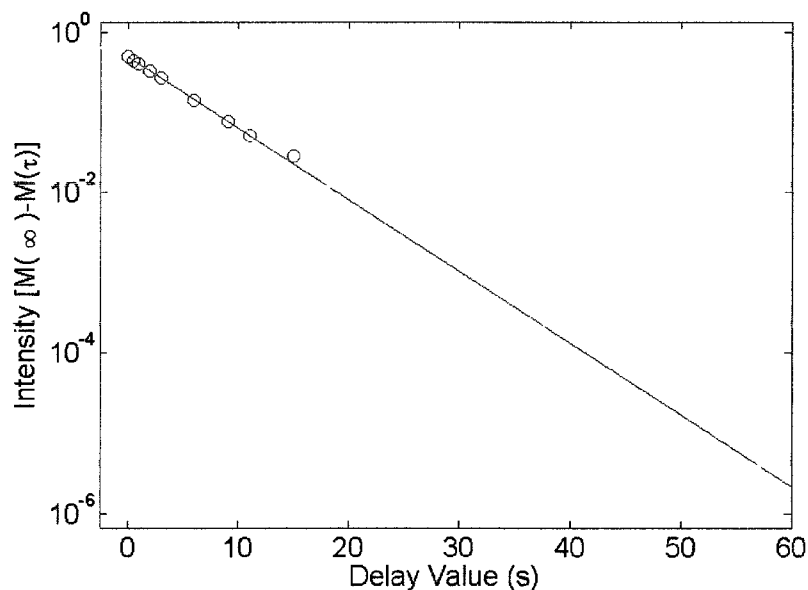


FIG. 5.1: The T_1 recovery curve of $(Ca_{2/3}La_{1/3})(Li_{1/3}Nb_{2/3})O_3$ at 319 K. The line through the data points represents a single-exponential fit applied to the results.

In addition to the ${}^7\text{Li}$ relaxation study, ${}^{93}\text{Nb}$ MAS NMR spectra were obtained for both samples. There was no T_{1z} analysis performed on these spectra due to the difficulty in getting a sufficiently saturated spectrum in order to properly perform a saturation-recovery experiment. However, there is still structural information to be obtained from the MAS spectra. For the $(\text{Ca}_{2/3}\text{La}_{1/3})(\text{Li}_{1/3}\text{Nb}_{2/3})\text{O}_3$ sample, a two-dimensional double-quantum satellite-transition MAS (STMAS) spectra was also obtained.

5.3 Results and Interpretation

5.3.1 Analysis of the Isotropic Shift and T_{1z} Relaxation of ${}^7\text{Li}$

Typical ${}^7\text{Li}$ MAS spectra for $\text{Ca}(\text{Li}_{1/3}\text{Nb}_{2/3})\text{O}_3$ and $(\text{Ca}_{2/3}\text{La}_{1/3})(\text{Li}_{1/3}\text{Nb}_{2/3})\text{O}_3$ are shown in Figures 5.2 and 5.4, respectively, with the center peak of each spectrum shown in more detail in Figures 5.3 and 5.5. Both spectra are relatively simple: a strong central peak with a small secondary peak located slightly upfield. The only noticeable difference between the spectra of the two materials being the shape of the small secondary peak. $\text{Ca}(\text{Li}_{1/3}\text{Nb}_{2/3})\text{O}_3$ has a relatively narrow peak (~ 70 Hz), while the other composition has a much broader shoulder (~ 300 Hz).

For lithium in these two materials, the primary interaction is the chemical shielding interaction (described in Section 2.4.1). The behavior of the isotropic chemical shift for the primary peaks of both materials was studied as a function of temperature. The isotropic position is taken as the frequency location of the highest point of the center peak of the spectrum. The results for temperature dependence of the isotropic chemical shift of $\text{Ca}(\text{Li}_{1/3}\text{Nb}_{2/3})\text{O}_3$ are shown in Figure 5.6.

When the isotropic shift is plotted against temperature, it results in a linear relation as defined by,

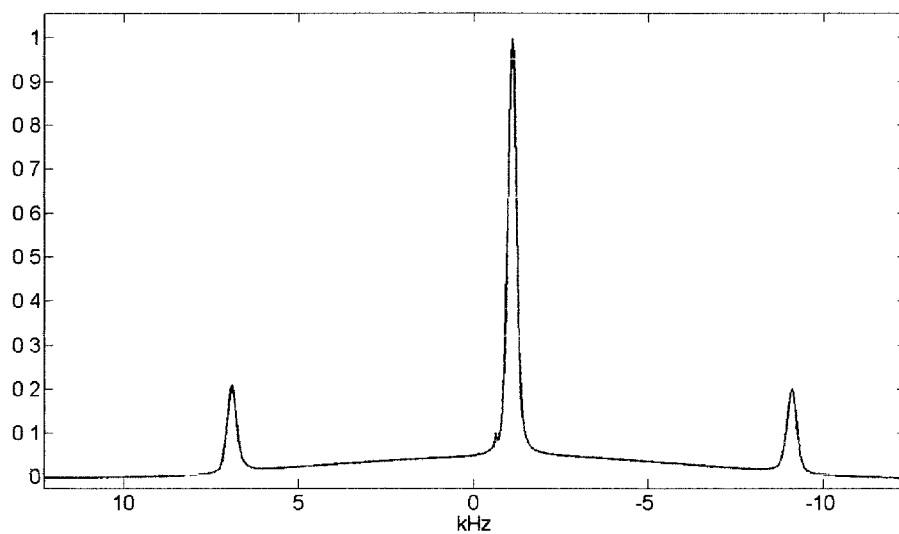


FIG. 5.2: ${}^7\text{Li}$ MAS spectrum of $\text{Ca}(\text{Li}_{1/3}\text{Nb}_{2/3})\text{O}_3$ performed at a spin rate of 8 kHz in a 17.6 T static field at a temperature of 280 K

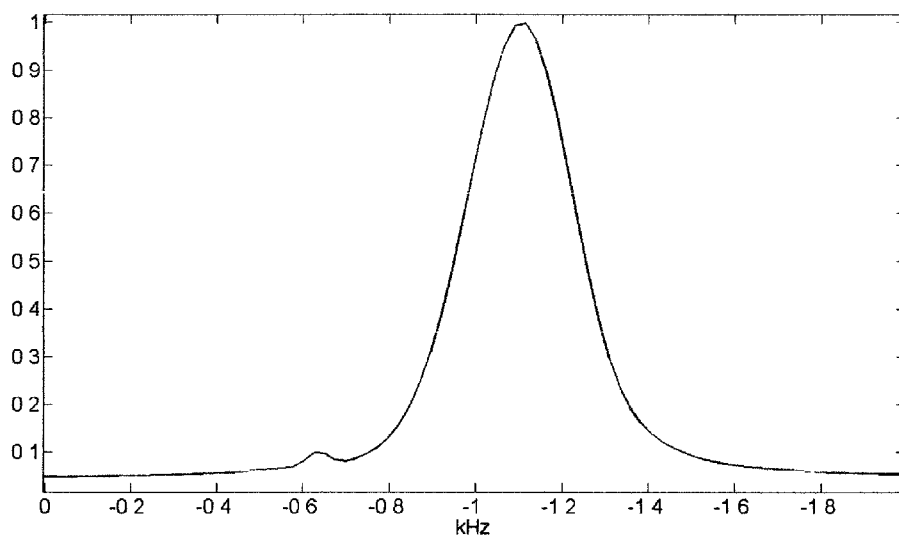


FIG. 5.3: Center peak of ${}^7\text{Li}$ MAS spectrum of $\text{Ca}(\text{Li}_{1/3}\text{Nb}_{2/3})\text{O}_3$ performed at a spin rate of 8 kHz in a 17.6 T static field at a temperature of 280 K

$$\delta_{iso}(\text{Hz}) = (3.53 \pm 0.53)T + (-2032 \pm 154). \quad (5.1)$$

In addition to the isotropic shift, the behavior of the T_{1z} relaxation time was also

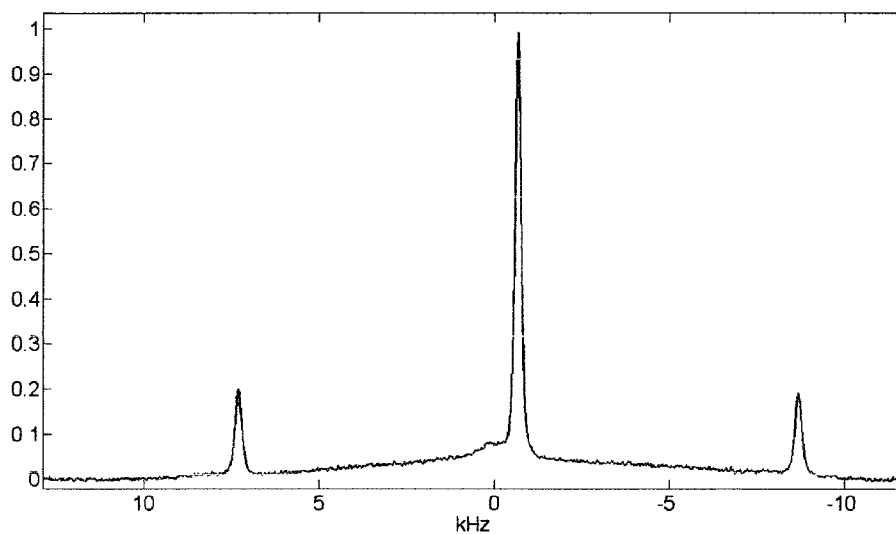


FIG. 5.4: ${}^7\text{Li}$ MAS spectrum of $(\text{Ca}_{2/3}\text{La}_{1/3})(\text{Li}_{1/3}\text{Nb}_{2/3})\text{O}_3$ performed at a spin rate of 8 kHz in a 17.6 T static field at a temperature of 280 K

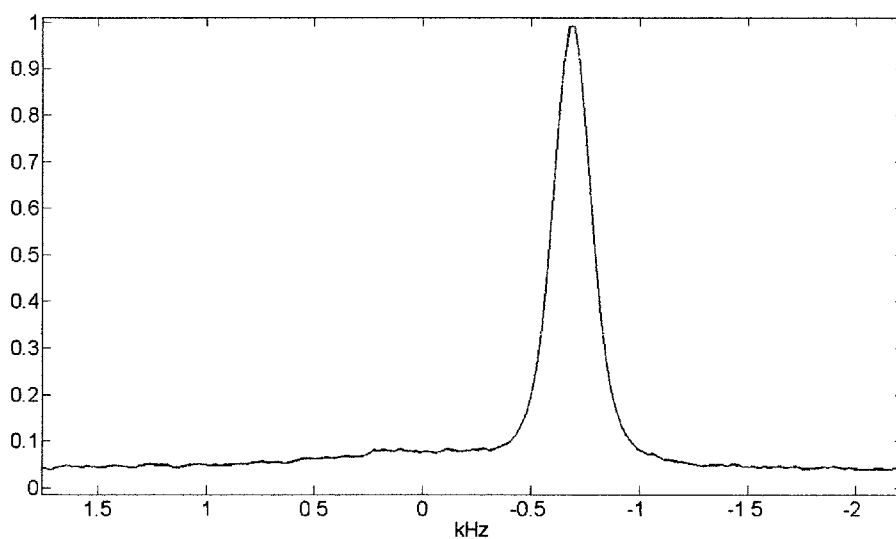


FIG. 5.5: Center peak of ${}^7\text{Li}$ MAS spectrum of $(\text{Ca}_{2/3}\text{La}_{1/3})(\text{Li}_{1/3}\text{Nb}_{2/3})\text{O}_3$ performed at a spin rate of 8 kHz in a 17.6 T static field at a temperature of 280 K

studied as a function of temperature. The results of this for $\text{Ca}(\text{Li}_{1/3}\text{Nb}_{2/3})\text{O}_3$ are shown in Figure 5.7, with the relaxation rate plotted on a logarithmic scale with respect to inverse temperature. Fitting these results leads to the relationship between relaxation rate and temperature as given by,

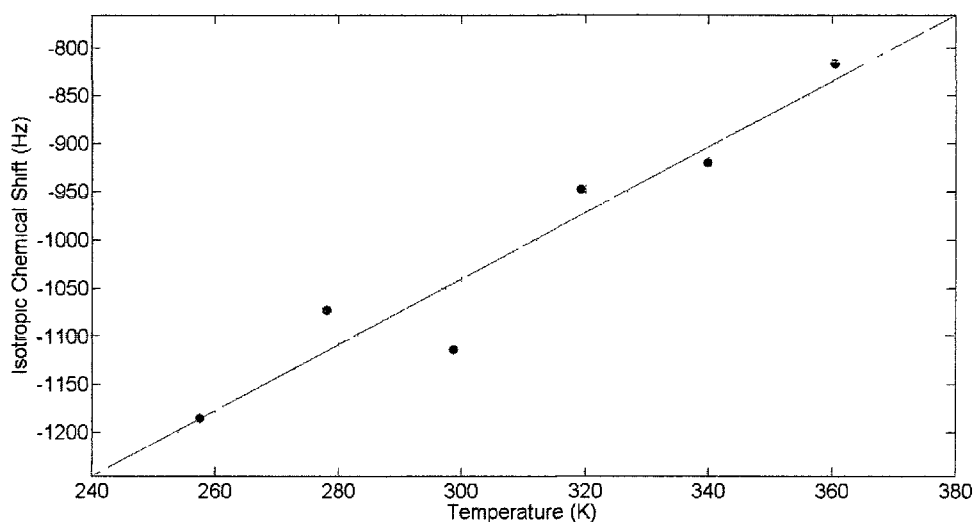


FIG. 5.6: Temperature dependence of the isotropic chemical shift of $\text{Ca}(\text{Li}_{1/3}\text{Nb}_{2/3})\text{O}_3$. Error bars are within the radius of each data point.

$$\frac{1}{T_{1z}} = (0.78 \pm 0.13)e^{(-5088.17 \pm 424)/RT}. \quad (5.2)$$

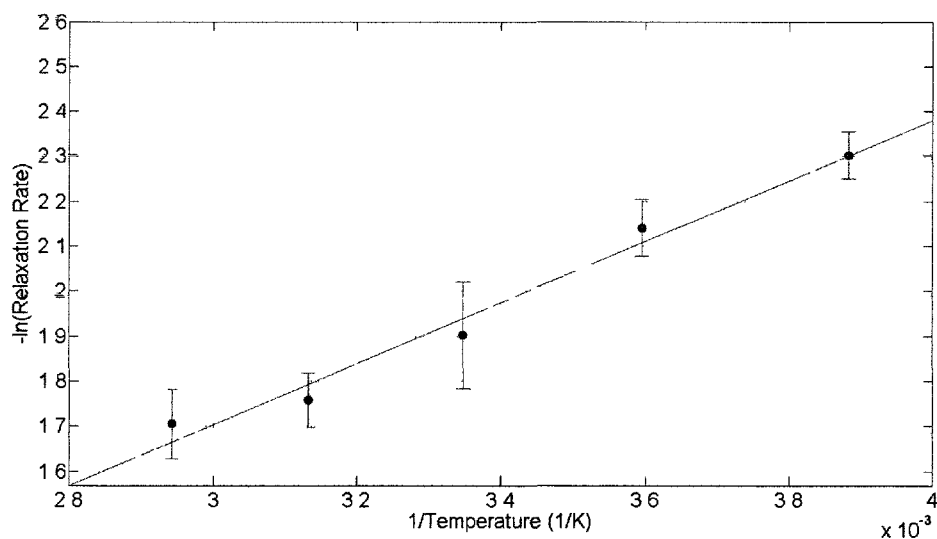


FIG. 5.7: Temperature dependence of the relaxation rate of $\text{Ca}(\text{Li}_{1/3}\text{Nb}_{2/3})\text{O}_3$

While there is some visible scatter in the T_{1z} plot, all of the values fall along the fit line within their error bars. The error bars themselves were determined by the scatter of

the relaxation rate measured at multiple points across the line shape. From examining both the isotropic chemical shift as well as the relaxation rate, it is clear that there is no structural phase change of these material over the temperature range covered by these experiments. This is important since it means that any devices made from these materials would not have sudden changes in performance with fluctuations in temperature. An attempt was made to also look at the relaxation behavior of the secondary peak. Unfortunately, due to the much lower intensity of the peak, accurate values for T_{1z} were not possible.

The values of the isotropic chemical shifts for $(Ca_{2/3}La_{1/3})(Li_{1/3}Nb_{2/3})O_3$ are shown in Figure 5.8. As with the $Ca(Li_{1/3}Nb_{2/3})O_3$ material, this also demonstrates a linear relation between isotropic shift and temperature, which is defined as,

$$\delta_{iso}(\text{Hz}) = (2.65 \pm 0.33)T + (-1434 \pm 97). \quad (5.3)$$

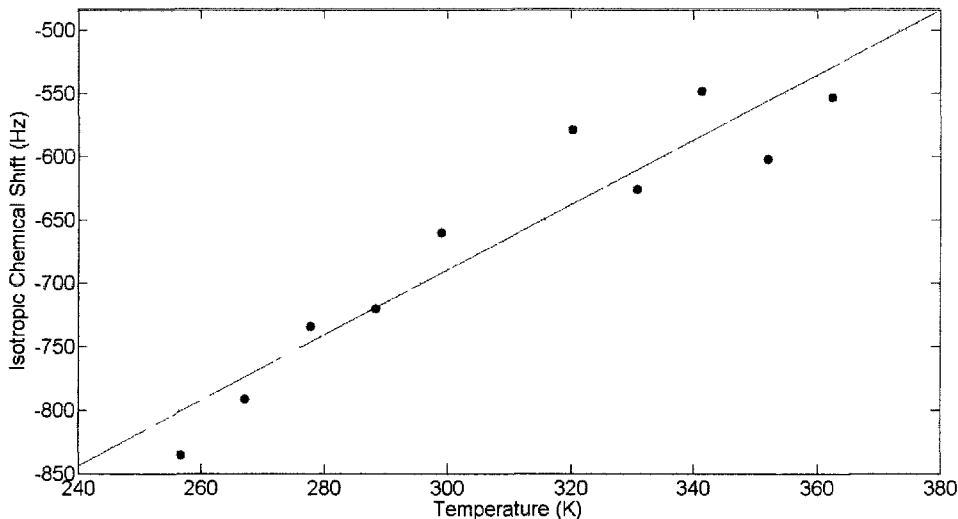


FIG. 5.8: Temperature dependence of the isotropic chemical shift of $(Ca_{2/3}La_{1/3})(Li_{1/3}Nb_{2/3})O_3$. Error bars are within the radius of each data point.

The behavior of the T_{1z} relaxation rate for $(Ca_{2/3}La_{1/3})(Li_{1/3}Nb_{2/3})O_3$ is shown in Figure 5.9. There is noticeably more scatter in this result than the other material. While

the values of the relaxation rate still all fall with the error bars of the fit, the amount of error present in each point is noticeably greater. This is a result of the relaxation rate not being as constant across the range of the peak.

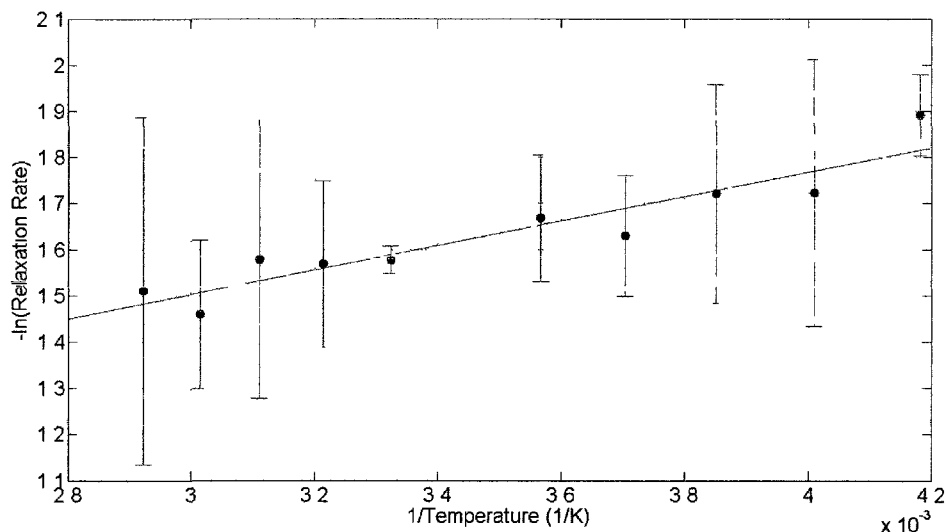


FIG. 5.9: Temperature dependence of the relaxation rate of $(\text{Ca}_{2/3}\text{La}_{1/3})(\text{Li}_{1/3}\text{Nb}_{2/3})\text{O}_3$

The fit of the relaxation rates results in the dependence between T_{1z} and temperature as given by,

$$\frac{1}{T_{1z}} = (2.01 \pm 0.26)e^{(-2211.52 \pm 291)/RT}. \quad (5.4)$$

As with the previous material, the temperature-dependencies of both the isotropic chemical shift and the T_{1z} relaxation rate of $(\text{Ca}_{2/3}\text{La}_{1/3})(\text{Li}_{1/3}\text{Nb}_{2/3})\text{O}_3$ exhibit no sudden jumps that would indicate a phase transition. It is also worth noting that the temperature dependence of both the isotropic shift and relaxation rate is less pronounced in $(\text{Ca}_{2/3}\text{La}_{1/3})(\text{Li}_{1/3}\text{Nb}_{2/3})\text{O}_3$ than was observed with $\text{Ca}(\text{Li}_{1/3}\text{Nb}_{2/3})\text{O}_3$. The isotropic shift of $\text{Ca}(\text{Li}_{1/3}\text{Nb}_{2/3})\text{O}_3$ changes at a rate of 3.53 Hz/K, while the isotropic shift of $(\text{Ca}_{2/3}\text{La}_{1/3})(\text{Li}_{1/3}\text{Nb}_{2/3})\text{O}_3$ is only affected at a rate of 2.65 Hz/K. Similarly, the activation energy for the relaxation rate is over twice as large for the $\text{Ca}(\text{Li}_{1/3}\text{Nb}_{2/3})\text{O}_3$ sample

when compared to $(Ca_{2/3}La_{1/3})(Li_{1/3}Nb_{2/3})O_3$.

5.3.2 Analysis of ^{93}Nb Results

While most of the work on these materials focused on the behavior of the lithium nuclei, there were also several experiments performed that observed the niobium nuclei. The ^{93}Nb spectra resulting from a basic single-pulse experiment for $Ca(Li_{1/3}Nb_{2/3})O_3$ and $(Ca_{2/3}La_{1/3})(Li_{1/3}Nb_{2/3})O_3$ are shown in Figures 5.10 and 5.11, respectively. Contrary to the lithium spectra, the niobium ones are noticeably more complicated with more overlap between adjacent peaks.

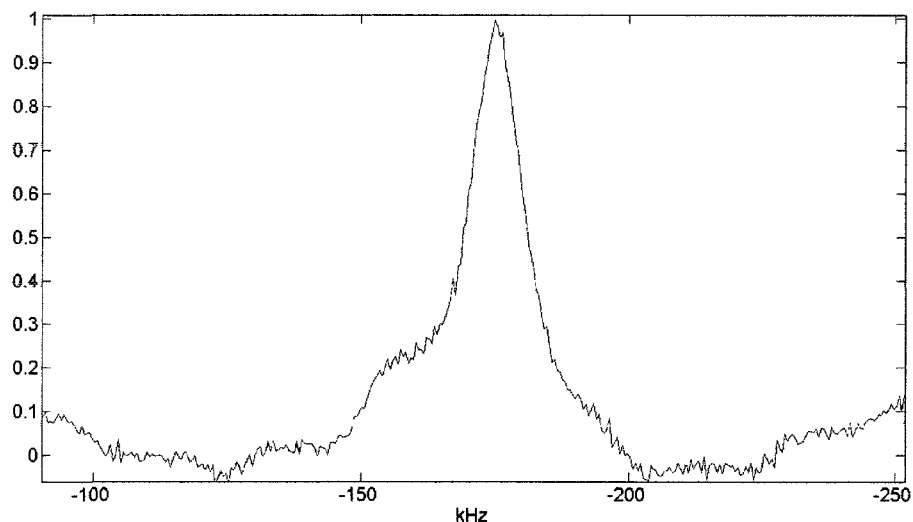


FIG. 5.10: 30 kHz MAS ^{93}Nb spectrum of $Ca(Li_{1/3}Nb_{2/3})O_3$ in 17.6 T static field at $T=310$ K

The spectrum for $Ca(Li_{1/3}Nb_{2/3})O_3$ shows at least two peaks clearly. The main peak is approximately 15 kHz wide, with a broader shoulder located slightly upfield. With how broad the peaks are, it is possible that more than two are present and are simply obscured by the overlap between them. The ^{93}Nb spectrum for $(Ca_{2/3}La_{1/3})(Li_{1/3}Nb_{2/3})O_3$ clearly shows four to five peaks. However, the peaks are much better resolved. The tallest peak has a linewidth of only 4 Hz. However, the total range of the center set of peaks is still

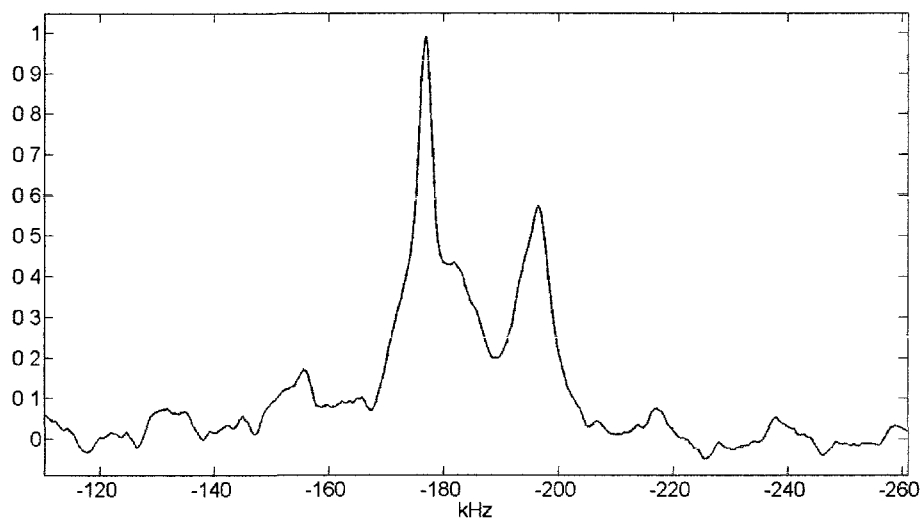


FIG. 5.11: 30 kHz MAS ^{93}Nb spectrum of $(\text{Ca}_{2/3}\text{La}_{1/3})(\text{Li}_{1/3}\text{Nb}_{2/3})\text{O}_3$ in 17.6 T static field at $T= 310\text{ K}$

wide enough to cause overlap with the spinning sidebands.

Unlike the lithium spectrum, the saturation-recovery pulse sequence was not usable to determine the T_{1z} relaxation time of the niobium spectra. The reason for this is that it was not possible to sufficiently saturate the spectrum as part of the pulse sequence. However, in an attempt to gain a better understanding of the line shape, a double-quantum satellite-transition magic angle spinning (STMAS) pulse sequence was used to separate the isotropic and anisotropic components of the spectrum [41–43]. This pulse sequence results in a two-dimensional spectrum as shown in Figure 5.12.

In this 2D spectrum, the coordinates of each peak are defined as $\langle\delta_{1/2}\rangle$ (along the F2 axis) and δ_{id} (along the F1 axis). A total of five distinct sites were identified, with their positions listed in Table 5.1 and slices taken along each peak shown in Figure 5.13. The direct dimension is referenced relative to NbCl solution. The indirect dimension is referenced relative to the direct through the relation

$$\delta_{id}^C = R\delta_{1/2}^C, \quad (5.5)$$

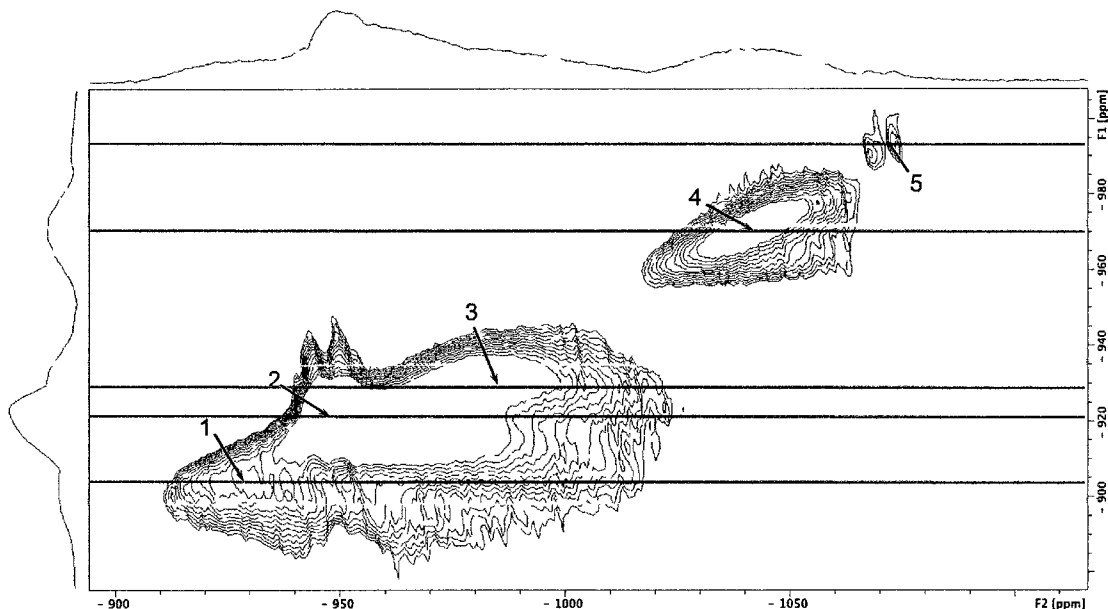


FIG. 5.12: 30 kHz Double-Quantum STMAS ^{93}Nb spectrum of $(\text{Ca}_{2/3}\text{La}_{1/3})(\text{Li}_{1/3}\text{Nb}_{2/3})\text{O}_3$ at $T=300$ K with standard shearing. Red lines represent locations of slices shown in Figure 5.13.

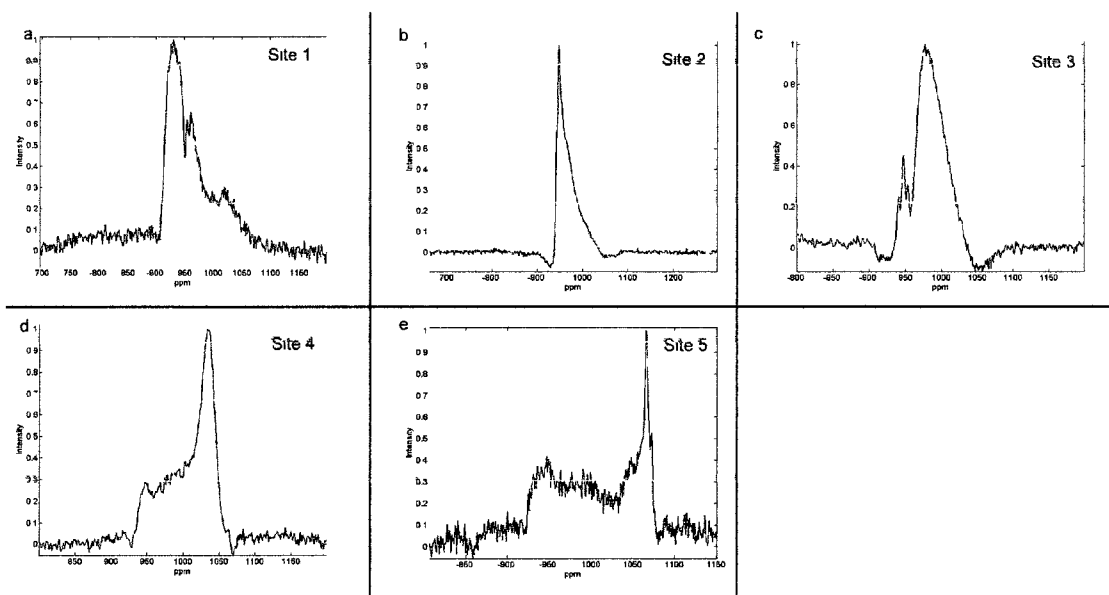


FIG. 5.13: Slices taken from a 30 kHz Double-Quantum STMAS ^{93}Nb spectrum of $(\text{Ca}_{2/3}\text{La}_{1/3})(\text{Li}_{1/3}\text{Nb}_{2/3})\text{O}_3$ at $T=300$ K at positions (a) $\delta_{id} = -903.1$ ppm, (b) $\delta_{id} = -923.8$ ppm, (c) $\delta_{id} = -929.7$ ppm, (d) $\delta_{id} = -971.6$ ppm, and (e) $\delta_{id} = -991.0$ ppm

where δ_{id}^C and $\delta_{1/2}^C$ represent the chemical shift value of the center of the anisotropic and isotropic axes, respectively. From the derivations shown in [44] and [45], the isotropic chemical shift and the isotropic shift of the second-order quadrupole (in Hertz) can be

Site Number	δ_{id} (ppm)	$\langle \delta_{1/2} \rangle$ (ppm)	δ_{iso}^{CS} (ppm)	δ_{iso}^{2Q} (kHz)	P_Q (MHz)
1	-903.1	-922.9	-915.7	-1313.2	13.17
2	-923.8	-950.2	-940.6	-1751.0	15.20
3	-929.7	-976.5	-959.6	-3104.0	20.24
4	-971.6	-1042.7	-1017.0	-4715.7	24.95
5	-991.0	-1070.9	-1042.0	-5299.3	26.45

TABLE 5.1: Identification of unique sites of ^{93}Nb in $(\text{Ca}_{2/3}\text{La}_{1/3})(\text{Li}_{1/3}\text{Nb}_{2/3})\text{O}_3$ using STMAS. F1 dimension is referenced relative to NbCl_5 solution

determined by the equations,

$$\langle \delta_{1/2} \rangle = \delta_{iso}^{\sigma} - R\delta_{iso}^{2Q} \quad (5.6)$$

$$\delta_{id} = \delta_{iso}^{\sigma} + \delta_{iso}^{2Q}. \quad (5.7)$$

In Equations 5.6 and 5.7, the scaling factor R is dependent on the nuclear spin and quantum coherence being observed. According to Table 2 of Ref. [45], in the case of double-quantum STMAS for a spin-9/2 nucleus, $R = 127/72$. The isotropic shift of the second-order quadrupole can be used to determine the quadrupole product (P_Q) using the relation,

$$\delta_{iso}^{2Q} = 3P_Q^2 \frac{3/4 - S(S+1)}{10\nu_0[2S(2S-1)]^2}. \quad (5.8)$$

Using these relations, the NMR parameters for each of the peaks was determined as shown in Table 5.1.

5.4 Conclusion

From the temperature-dependent studies of the high-dielectric microwave ceramics, it was shown that $(\text{Ca}_{2/3}\text{La}_{1/3})(\text{Li}_{1/3}\text{Nb}_{2/3})\text{O}_3$ is significantly less temperature-sensitive

with regards to both isotropic chemical shift and T_{1z} relaxation time. $\text{Ca}(\text{Li}_{1/3}\text{Nb}_{2/3})\text{O}_3$ was found to have a chemical shift that changed linearly with temperature at a rate of $3.53 \pm 0.53 \text{ Hz} \cdot \text{K}^{-1}$ and a relaxation rate that followed an Arrhenius relationship with an activation energy of $5.08 \text{ kJ} \cdot (\text{mol} \cdot \text{K})^{-1}$. $(\text{Ca}_{2/3}\text{La}_{1/3})(\text{Li}_{1/3}\text{Nb}_{2/3})\text{O}_3$, on the other hand, resulted with an isotropic chemical shift that changed at a rate of $2.65 \pm 0.33 \text{ Hz} \cdot \text{K}^{-1}$ and a T_{1z} relaxation rate with an activation energy of $2.21 \text{ kJ} \cdot (\text{mol} \cdot \text{K})^{-1}$. The most important thing to be inferred from these results is that $(\text{Ca}_{2/3}\text{La}_{1/3})(\text{Li}_{1/3}\text{Nb}_{2/3})\text{O}_3$ has noticeably less temperature-dependent behavior, likely making it much more useful of a material for the purpose of constructing electronic components. Less sensitivity to temperature for the NMR parameters would likely also result in less temperature-dependence of the device parameters if ionic motions responsible for spin-lattice relaxation are also responsible for dielectric loss.

The niobium spectra of each material mainly shows that while the total number of sites is similar, the linewidths for $(\text{Ca}_{2/3}\text{La}_{1/3})(\text{Li}_{1/3}\text{Nb}_{2/3})\text{O}_3$ are significantly narrower, making it easier to identify individual peaks. However, the MAS spectrum alone does not make it clear how many overlapping peaks may be present. The STMAS experiment performed on this material resulted in the identification of five unique sites, as well as the values of both the isotropic chemical shift and the quadrupole product (listed in Table 5.1) for each site.

CHAPTER 6

Conclusion

Through the studies discussed in this dissertation, several perovskite structures were examined. While the crystallographic structures of the $\text{Nd}_{\frac{2}{3}-x}\text{Li}_{3x}\text{TiO}_3$ materials and the dielectric microwave ceramics were all similarly perovskites, the composition of each lead to very different behaviors, even when observing the same nucleus. While the lithium NMR spectra of the microwave ceramics was dominated by the chemical shielding interaction, the presence of neodymium in the $\text{Nd}_{\frac{2}{3}-x}\text{Li}_{3x}\text{TiO}_3$ materials leads to the paramagnetic interaction taking precedence. Also, the highly ordered checkerboard structure of the $\text{Nd}_{\frac{2}{3}-x}\text{Li}_{3x}\text{TiO}_3$ materials results in a much larger number of unique sites (and therefore a much more complicated spectrum) when compared to the number of unique sites present in the microwave ceramics. These differences lead to slightly different approaches being taken to study each series of materials.

With the large number of unique lithium sites in the $\text{Nd}_{\frac{2}{3}-x}\text{Li}_{3x}\text{TiO}_3$ materials (28 in the case of $x=0.083$), the spectra were too complicated to simply deconvolute in order to obtain the NMR interaction tensor values. Fortunately, previous studies [1, 2] resulted in a proposed crystal structure for one of the concentrations ($x=0.083$). This made it possible to perform point-charge calculations in order to determine the tensor components

for each lithium site, for both the paramagnetic and quadrupole interactions. In addition to performing the point-charge calculations for the tensor components, software was also written to simulate the NMR spectra of both a spin-1 (${}^6\text{Li}$) system with a paramagnetic interaction present and a spin-3/2 (${}^7\text{Li}$) system with both paramagnetic and quadrupole interactions.

At high-temperature, simulated spectra based on the point-charge calculations resulted in a very good match to the experimental results. Several points of interest also became apparent. The paramagnetic interaction in these samples is a couple orders of magnitude stronger than the quadrupole interaction. Based on the principal values of the paramagnetic tensors, the 28 unique lithium sites could be easily grouped into three sets. Each set featured similar principal values (δ_{iso} , $\Delta\sigma$, and η). These three groups correspond to the three visible sets of peak present in each spectrum. It also fits the idea that the relative intensities of the peaks change with respect to lithium concentration, meaning that the relative populations of each group is changing based on the size of the lithium regions in the material.

While the simulated spectra agreed well with room-temperature and high-temperature experimental results, the low-temperature simulation does not match as well with experiment. It was theorized that this is due to possible displacement of the lithium atoms within octahedral cages formed by the neighboring oxygen atoms. At high enough temperatures, the jump rate between displacements is quick enough to be in the fast limit, leading to averaging of the interaction tensor. In the lower-temperature experiments, the nuclei are in the intermediate range where it is necessary to take into account the jump rate in order to accurately simulate the spectrum. Due to the number of sites present, each with its own set of displacements, the dynamics of the complete system were not simulated. However, the behavior of the interaction tensors of one of the lithium sites along the edge of the lithium-rich region was studied with respect to displacement amount and jump rate. The behavior of one-site simulations with respect to jump rate seems to match

with the observed behavior of the overall experimental spectra as temperature is lowered.

In the case of the microwave ceramic samples, the much simpler structure resulted in lithium NMR spectra that were much easier to interpret. The temperature dependence of both the isotropic chemical shift and the $T_{1\rho}$ relaxation rate was determined for each of the two samples. In both cases, the isotropic chemical shift behaved linearly with temperature, at a rate of 3.53 ± 0.53 Hz/K for $\text{Ca}(\text{Li}_{1/3}\text{Nb}_{2/3})\text{O}_3$ and 2.65 ± 0.33 Hz/K for $(\text{Ca}_{2/3}\text{La}_{1/3})(\text{Li}_{1/3}\text{Nb}_{2/3})\text{O}_3$. The relaxation time for each of these materials followed an Arrhenius behavior with an activation energy of 5.08 ± 0.424 kJ \cdot (mol \cdot K) $^{-1}$ for $\text{Ca}(\text{Li}_{1/3}\text{Nb}_{2/3})\text{O}_3$ and 2.21 ± 0.29 kJ \cdot (mol \cdot K) $^{-1}$ for $(\text{Ca}_{2/3}\text{La}_{1/3})(\text{Li}_{1/3}\text{Nb}_{2/3})\text{O}_3$. From these results, it is clear that the composition $(\text{Ca}_{2/3}\text{La}_{1/3})(\text{Li}_{1/3}\text{Nb}_{2/3})\text{O}_3$ is significantly less affected by temperature over the range observed, making it much more desirable in the use of electronic components.

In addition to the lithium studies that composed the majority of the microwave ceramics work, several experiments also observed the ^{93}Nb nucleus. The 1D single-pulse spectrum of each material did not reveal too much information, aside from the fact that there are clearly several unique sites with overlapping line shapes. While the range of isotropic shifts and overall span are similar between the two materials, the spectrum of $(\text{Ca}_{2/3}\text{La}_{1/3})(\text{Li}_{1/3}\text{Nb}_{2/3})\text{O}_3$ has noticeably narrower linewidths, allowing the different sites to be better resolved. Additionally, a double-quantum satellite transition MAS experiment was performed on $(\text{Ca}_{2/3}\text{La}_{1/3})(\text{Li}_{1/3}\text{Nb}_{2/3})\text{O}_3$ in order to better isolate the individual sites, separating the isotropic and anisotropic components of the spectrum. This resulted in the clear identification of five unique sites, as well as the values of the isotropic chemical shifts and quadrupole products.

APPENDIX A

Point Charge EFG Calculations of Lithium Niobate

The calculations described in Chapter 4 use a point-charge approximation in order to calculate the electric field gradient of the $\text{Nd}_{\frac{2}{3}-x}\text{Li}_{3x}\text{TiO}_3$ samples. The large number of atoms present per unit cell in these materials, as well as the complexity of the neodymium electron distribution, make the more accurate method of using density functional theory (DFT), not feasible. In order to determine how accurate the point-charge model is, the same calculations were also performed for two phases of lithium niobate (LiNbO_3). These materials have a much simpler structure which allows DFT calculations to be performed, from which the field gradient tensors can be determined. This permits direct comparison to the point-charge model.

Two forms of lithium niobate were examined, the paraelectric and ferroelectric structures. Both of these are distorted forms of the basic perovskite structure which is similar to the $\text{Nd}_{\frac{2}{3}-x}\text{Li}_{3x}\text{TiO}_3$ idealized structure. Equation A.1 gives the primitive vectors of the LiNbO_3 unit cell (illustrated in Figure A.2) that were used for the paraelectric structure, with the atom positions shown in Table A.1 and the structure shown in Figure A.1. The

ferroelectric structure is shown in Figure A.3 with the corresponding unit cell parameters given in Equation A.2 (illustrated in Figure A.2) and atom positions listed in Table A.2.

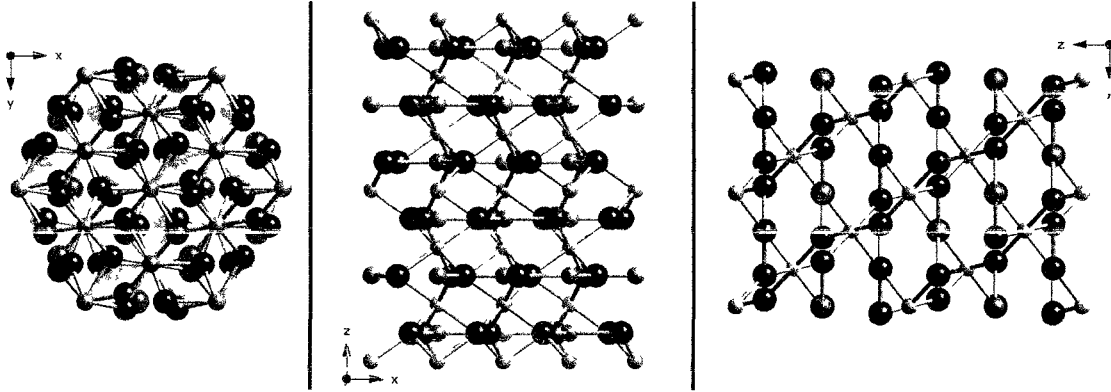


FIG. A.1: The crystal structure of the paraelectric form of LiNbO_3 along the $[001]$, $[010]$, and $[100]$ axes Niobium = Blue, Oxygen = Red, Lithium = Green. [46]

$$\hat{a}_{\text{para}} = 2.6274991390\hat{x} - 1.5169873360\hat{y} + 4.5970006560\hat{z} \quad (\text{A.1})$$

$$\hat{b}_{\text{para}} = 0.0000000000\hat{x} + 3.0339746710\hat{y} + 4.5970006560\hat{z}$$

$$\hat{c}_{\text{para}} = -2.6274991390\hat{x} - 1.5169873360\hat{y} + 4.5970006560\hat{z}$$

Nucleus	\hat{a}	\hat{b}	\hat{c}
Li	0.2500000000	0.2500000000	0.2500000000
Li	0.7500000000	0.7500000000	0.7500000000
Nb	0.0000000000	0.0000000000	0.0000000000
Nb	0.5000000000	0.5000000000	0.5000000000
O	0.6313333333	0.8686666667	0.2500000000
O	0.2500000000	0.6313333333	0.8686666667
O	0.8686666667	0.2500000000	0.6313333333
O	0.3686666667	0.1313333333	0.7500000000
O	0.7500000000	0.3686666667	0.1313333333
O	0.1313333333	0.7500000000	0.3686666667

TABLE A.1: Atom positions in paraelectric LiNbO_3

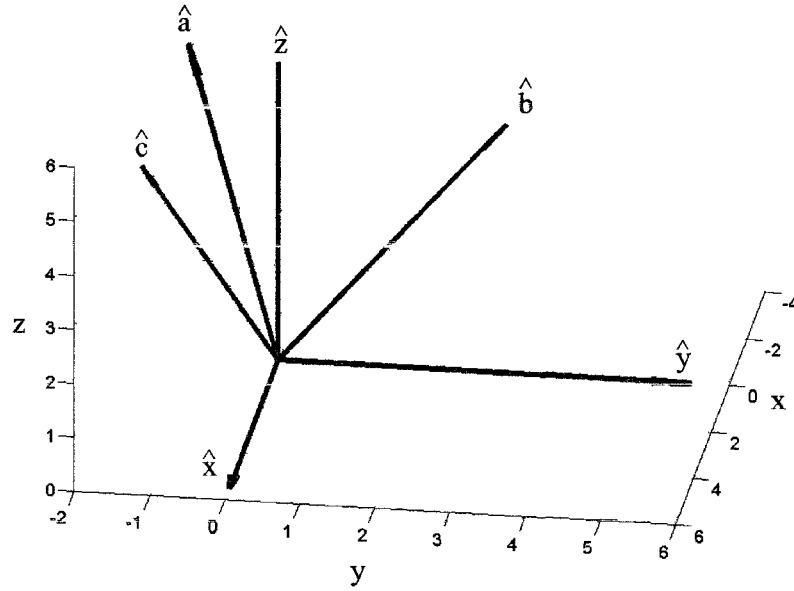


FIG. A.2: The basis vectors of the paraelectric form of LiNiO_3

$$\hat{a}_{\text{ferro}} = 2.5999991470\hat{x} - 1.5011102070\hat{y} + 4.6243339730\hat{z} \quad (\text{A.2})$$

$$\hat{b}_{\text{ferro}} = 0.0000000000\hat{x} + 3.0022204140\hat{y} + 4.6243339730\hat{z}$$

$$\hat{c}_{\text{ferro}} = -2.5999991470\hat{x} - 1.5011102070\hat{y} + 4.6243339730\hat{z}$$

For both the paraelectric and ferroelectric states, the electric field gradient tensor was calculated at the location of each nucleus using several DFT codes with different levels of approximation, as well as the point-charge model. The DFT methods used include variants of the linearized augmented plane wave (LAPW) method [34], the Elk full-potential linearized augmented plane wave (Elk), and the Gauge Including Projector Augmented Waves approach [33] within the Quantum Espresso package (gipaw).

LAPW allows for several approximations of exchange and correlation, but makes no

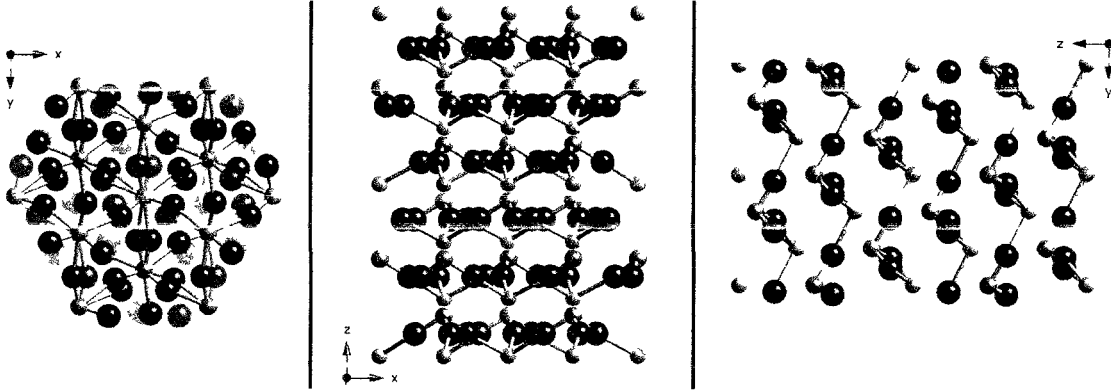


FIG A 3 The crystal structure of the ferroelectric form of LiNbO_3 along the $[001]$, $[010]$, and $[100]$ axes Niobium = Blue, Oxygen = Red, Lithium = Green [46]

Nucleus	\hat{a}	\hat{b}	\hat{c}
Li	0.28180000	0.28180000	0.28180000
Li	0.78180000	0.78180000	0.78180000
Nb	0.00000000	0.00000000	0.00000000
Nb	0.50000000	0.50000000	0.50000000
O	0.85856667	0.61136333	0.22037000
O	0.61136333	0.22037000	0.85856667
O	0.22037000	0.85856667	0.61136333
O	0.11136333	0.35856667	0.72037000
O	0.72037000	0.11136333	0.35856667
O	0.35856667	0.72037000	0.11136333

TABLE A.2: Atom positions in ferroelectric LiNbO_3

approximations with regards to the shape of the crystal potential, unlike other methods which may use a spherical approximation around each atom. The basis used for LAPW considers the crystal as two separate zones: spheres around each atom and the remaining region. The areas near the atoms are treated as a linear combination of atomic-like functions. The interstitial region is treated as a collection of planewaves.

The GIPAW method uses a pseudopotential approximation, which has been used with previous methods, but takes into account the difference in contributions from the core and valence electrons.

The full-potential augmented plane wave method used by Elk allows the potential to be of a general form, representing the full potential, as opposed to using a shape ap-

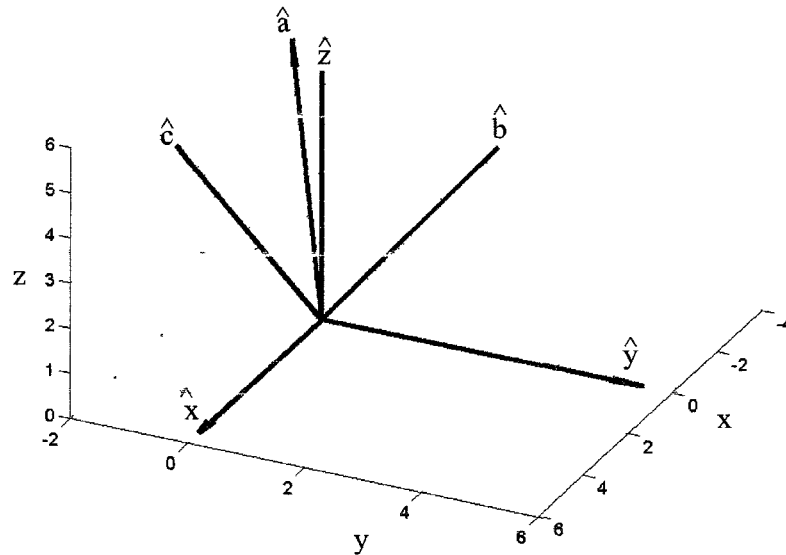


FIG. A.4: The basis vectors of the ferroelectric form of LiNiO_3

proximation (such as a muffin tin approximation) [47]. Using a full potential makes it possible to overcome the limitations of the basic LAPW method, which is accurate for close-packed metal systems, but less reliable for open semiconductor surfaces or other situations where highly accurate solutions to local density functional equations are required.

The resulting tensor components and asymmetry values are shown in Tables A.3 (paraelectric) and A.4 (ferroelectric). It is clear that the point-charge model is not good enough for providing exact values for the tensor components in these materials. The agreement between the different DFT methods is significantly better than the agreement between any one of them and the point-charge model. However, the point-charge model may be considered sufficient for the calculations performed in Chapter 4 on the $\text{Nd}_{\frac{2}{3}-x}\text{Li}_{3x}\text{TiO}_3$ materials. The values from the point-charge calculations do still provide at least an order of magnitude to the quadrupole interaction (which turns out to

Nucleus	Method	V_{zz}	V_{yy}	V_{xx}	η
Li	LAPW	-0.235	0.118	0.118	0
	Elk	-0.235	0.117	0.117	0
	gipaw	-0.201	0.100	0.100	0
	Point-charge	-0.050	0.025	0.025	0
Nb	LAPW	0.710	-0.355	-0.355	0
	Elk	0.694	-0.347	-0.347	0
	gipaw	0.678	-0.339	-0.339	0
	Point-charge	0.0026	-0.0013	-0.0013	0
O	LAPW	-0.720	0.484	0.236	0.35
	Elk	-0.881	0.553	0.328	0.26
	gipaw	-0.704	0.482	0.222	0.37
	Point-charge	-0.0507	0.0367	0.0141	0.44

TABLE A.3: EFG tensor components of atom sites in paraelectric LiNbO₃ (units are $\frac{V}{m^2} \times 10^{21}$)

Nucleus	Method	V_{zz}	V_{yy}	V_{xx}	η
Li	LAPW	-0.107	0.053	0.053	0
	Elk	-0.106	0.053	0.053	0
	gipaw	-0.090	0.045	0.045	0
	Point-charge	-0.0152	0.0074	0.0074	0
Nb	LAPW	-1.198	0.599	0.599	0
	Elk	-1.060	0.530	0.530	0
	gipaw	-1.179	0.589	0.589	0
	Point-charge	-0.0169	0.0085	0.0085	0
O	LAPW	1.519	-1.147	-0.372	0.51
	Elk	1.545	-1.241	-0.304	0.61
	gipaw	1.505	-1.105	-0.400	0.47
	Point-charge	0.0932	-0.0758	-0.0174	0.60

TABLE A.4: EFG tensor components of atom sites in ferroelectric LiNbO₃ (units are $\frac{V}{m^2} \times 10^{21}$)

be quite small in the case of $\text{Nd}_{\frac{2}{3}-x}\text{Li}_{3x}\text{TiO}_3$) as well as a reasonably accurate result for the symmetry properties of the structure. With the paramagnetic interaction in the $\text{Nd}_{\frac{2}{3}-x}\text{Li}_{3x}\text{TiO}_3$ materials being orders of magnitude larger than the estimated quadrupole interaction, the error in the EFG calculations due to the point-charge approximation is negligible in comparing the simulations to experimental results.

The primary source of the inaccuracy of the point-charge calculations is the covalent bonding present in these materials, which distorts the electron distribution. It has been shown in other studies that in the case of highly ionic materials, the point-charge model is much more successful. For example, Barton and Cashion used a point charge approximation to calculate the quadrupole splitting for Gd^{3+} in highly ionic gadolinium compounds and had agreement within 12% of experimental results [48]. Some of the error in this case was attributed to slight variations in the crystal structure due to variation in the temperature at which the crystal structure was determined (room temperature) and the temperature at which the spectra to determine the quadrupole splitting was performed (4.2 K).

While point-charge calculations are generally limited to ionic crystals, it has been shown that they can still be useful in some covalent systems. Dane Spearing examined the quadrupole tensor for oxygen in the highly covalent SiO_2 cristobalite compound using a point-charge approximation. The calculations produced values reasonably close to previous experimental results: $C_Q = 7.63$ MHz and $\eta = 0.20$ calculated using point charges, compared to the experimentally determined $C_Q = 5.3 \pm 0.1$ MHz and $\eta = 0.125 \pm 0.005$ [49]. While this agreement is still noticeably worse than the case of ionic materials, it does show that in covalent systems the point-charge calculation can still be a good starting point to get an approximate value.

APPENDIX B

Temperature Calibration Using Lead

Nitrate

When studying the temperature-dependence of an NMR spectrum, it is necessary to be able to determine the temperature of the sample. Chapter 3 discussed how variable temperature (VT) experiments are performed. To briefly summarize: these NMR experiments work by passing dry nitrogen gas through a heat exchanger where it is in close thermal contact with liquid nitrogen (at least in the case of experiments below room temperature). This cooled gas then enters the NMR probe, initially passing across a heating element. Temperature is monitored by a resistive sensor located near the sample, and an analog PID controller uses the sensor's resistance to vary the heater current so that the sensor output matches the user-specified set point.

It is important to note that the temperature is not actually monitored in the sample itself. In static experiments it is usually enough to use the observed "set" temperature from the sensor in the probe as the sample temperature. As long as enough time is allowed for the sample temperature to equilibrate before running an experiment, it will settle to the same temperature as the nitrogen VT gas. In some cases, there may be some minimal

heating from the rf field coils in the probe, particularly in larger diameter coils that require more power to produce a suitable rf field. In our situation, this effect is negligible except for multiple pulse sequences with high duty cycles.

In the case of a magic angle spinning experiment, the difference between the temperature observed by the sensor and the true sample temperature can be very large. As a result of the rotor spinning, frictional heating due to the spinner gas moving against the rotor will cause the sample temperature to rise. For a 30 kHz MAS experiment, this effect may be as large as 30 K. For this reason, it is necessary to calibrate the set temperature (the temperature monitored by the feedback controller) and the true sample temperature. It is also necessary to note that the calibration is probe and spin rate specific and may vary with different nitrogen VT gas flow rates, and spinner drive and bearing gas pressures.

The calibration method of choice is to utilize a sample with a very strong, well known, temperature-dependant chemical shift [6]. Depending on the material, the isotropic chemical shift of an MAS spectrum can be very easy to determine as a function of temperature. The sample used in this case was lead nitrate $[\text{Pb}(\text{NO}_3)_2]$, with the observed nucleus being ^{207}Pb . The isotropic chemical shift of lead nitrate has been thoroughly studied [6, 7]. It is also a very simple MAS spectrum to interpret since there is only a single site for the lead nucleus.

From previous studies [50], it has been shown that the isotropic chemical shift of ^{207}Pb varies with temperature according to the relation,

$$\delta'_0(T_{\text{real}}) = 0.666T_{\text{real}} + \delta_0. \quad (\text{B.1})$$

This provides the slope of the calibration line, by determining how much change in sample temperature occurs by a change in the set temperature.

Since the chemical shift values recorded are relative to a reference value and not absolute, it is necessary to find a fixed point in order to set the y-intercept of the calibration

line. For this we used deuterated stearic acid, $\text{CH}_3(\text{CH}_2)_{16}\text{COOH}$. Our sample of stearic acid has a freezing point of 69.6°C , determined outside the magnetic field with a mercury thermometer. Like most materials in NMR, the liquid state spectrum of stearic acid is significantly different from its solid state spectrum. The liquid state causes all of the spins to be motionally averaged, collapsing the spectrum to a single narrow peak in the frequency domain. In solid form, the spectrum takes the form of a traditional powder pattern. The observed nucleus in these experiments was deuterium. It is also very easy to see the difference between the two states by looking at the FID. When in the liquid state the FID has a significantly longer T_2 and a single narrow peak in the spectrum. Figure B.1 shows the difference in spectra between a frozen [Figure B.1(a)] and melted [Figure B.1(b)] sample.

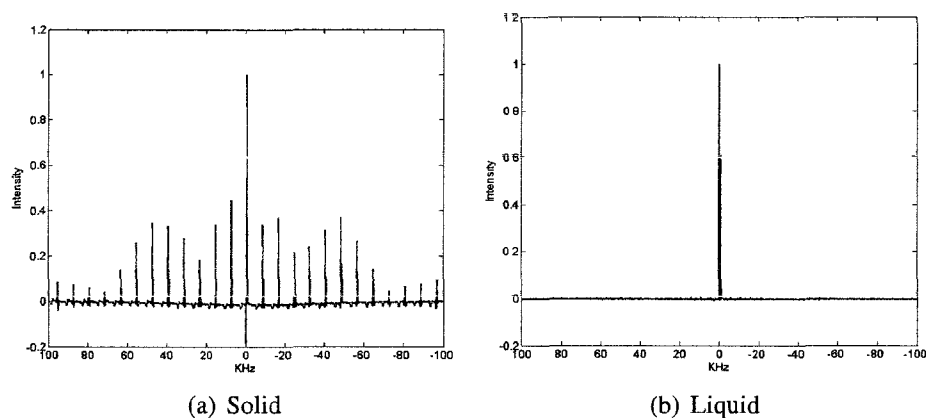


FIG. B.1: ^2H spectra of stearic acid below (a) and above (b) the freezing point of 69.6°C

The stearic acid sample was placed in the field with the temperature initially set well below the freezing point, and allowed to equilibrate for at least 15 minutes. A spectrum was acquired with the sample in the solid state. The temperature was then subsequently raised and allowed to stabilize for 15 minutes before acquiring another spectrum. This procedure was repeated until the spectrum changed significantly, signalling the melting of the sample. The temperature was then adjusted up and down in finer increments (being allowed to stabilize after each adjustment) so that the melting point (true sample temper-

Probe	Spin Rate(kHz)	m	b (K)
2.5 mm	20	0.960 ± 0.009	31.3 ± 2.3
	25	0.928 ± 0.006	52.3 ± 1.7
	30	0.917 ± 0.057	57 ± 18
4 mm	8	1.029 ± 0.011	10.48 ± 3.12

TABLE B.1: Temperature calibration for magic angle spinning experiments. $T_{real} = mT_{set} + b$

ature of 69.6°C) could be accurately determined.

Once the melting point of the stearic acid was determined, the sample was then removed and replaced with the lead nitrate sample. The sample was placed under identical conditions used to determine the melting point of the stearic acid. This includes the set temperature of the sample, the nitrogen gas flow rate, the heater power, and the spinning speed. Under these conditions, an NMR spectrum was acquired. The resulting isotropic chemical shift can then be used to determine a common reference for other lead nitrate experiments. This then provides the intercept point for the calibration line. The resulting calibration lines for several spin rates are shown in Figure B.2. Table B shows the parameters of each of the calibration lines. This temperature calibration was performed for the 2.5 mm probe in the 17.6 T field. Additionally, the 4 mm probe was calibrated for its use in the microwave ceramics study. The results of this are shown in Figure B.3. Since the stearic acid melting point is only used to determine a reference frequency for lead nitrate, it only needs to be determined for one set of conditions. The resulting lead nitrate chemical shift reference can then be used for all other lead nitrate spectra in the same field.

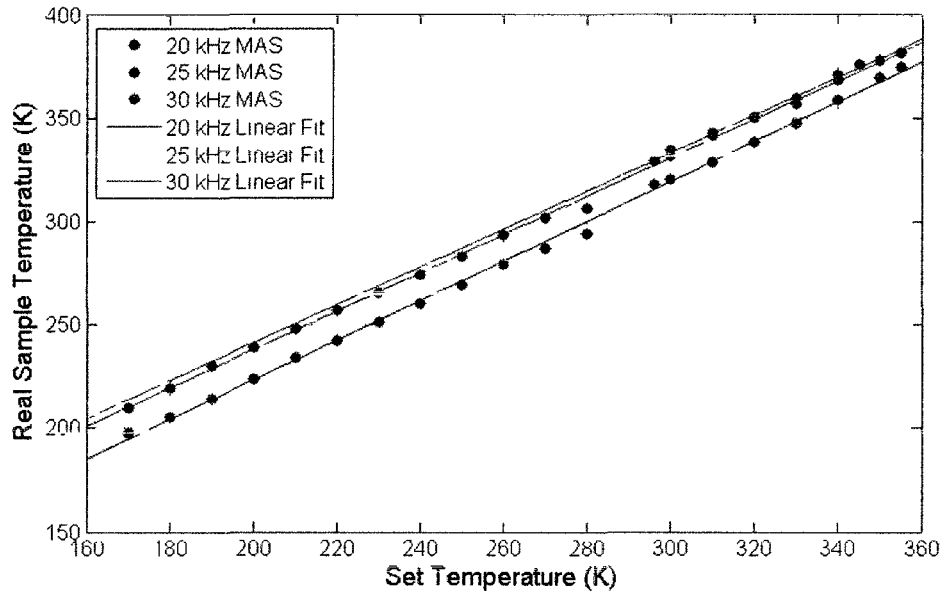


FIG. B.2. Temperature calibration for true sample temperature based on set temperature during magic angle spinning experiments in 2.5 mm probe for a variety of spinning speeds. The lines represent the linear fits for each spin rate.

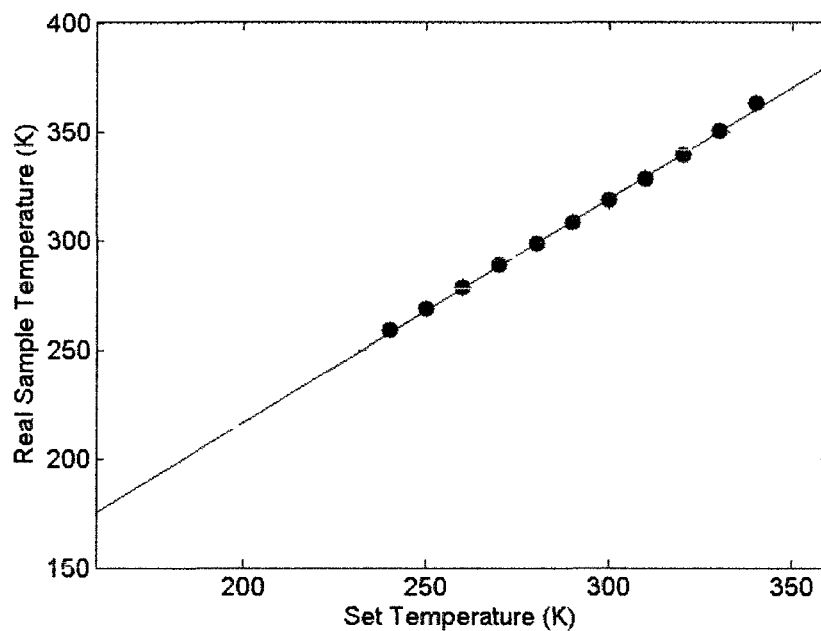


FIG. B.3. Temperature calibration for true sample temperature based on set temperature during magic angle spinning experiments in 4 mm probe at 8 kHz.

APPENDIX C

Nd_{0.58}Li_{0.25}TiO₃ Interaction Tensors

Tables C.1, C.2, and C.3 show the paramagnetic and quadrupole interaction tensors that result in the principal values previously shown in Table 4.1, producing the simulated line shape shown in Figure 4.10. Tables C.4 and C.5 list the C_Q and η_Q of each site resulting from point-charge calculations performed with the sites each moved 1.5 Å off-center in various directions.

Site Number	Paramagnetic Tensor (kHz)			Quadrupole Tensor (kHz)		
1	-65.2578	73.8206	26.162	-0.1461	-0.0016	-0.3744
	73.8206	42.4419	-6.8698	-0.0016	0.6786	0.0524
	26.162	-6.8698	165.1077	-0.3744	0.0524	-0.5325
2	-64.189	71.43	22.7391	-0.2898	-0.0396	-0.2328
	71.43	40.0076	-5.8833	-0.0396	0.4473	0.0113
	22.7391	-5.8833	162.1172	-0.2328	0.0113	-0.1575
3	-63.4499	69.6436	19.8125	-0.3005	0.0635	-0.1983
	69.6436	38.4119	-5.0247	0.0635	0.5453	0.0107
	19.8125	-5.0247	159.7418	-0.1983	0.0107	-0.2448
4	-62.1428	67.1565	17.0674	-0.1711	-0.0206	-0.0352
	67.1565	35.8611	-4.2344	-0.0206	0.1767	-0.0001
	17.0674	-4.2344	156.5579	-0.0352	-0.0001	-0.0056
5	-60.6398	64.5646	15.0155	0.1704	-0.0795	-0.1251
	64.5646	33.1324	-3.6099	-0.0795	0.013	0.0086
	15.0155	-3.6099	153.2077	-0.1251	0.0086	-0.1834
6	-59.1455	62.028	13.3415	0.5525	-0.0349	-0.6653
	62.028	30.503	-3.1204	-0.0349	-1.1059	-0.0275
	13.3415	-3.1204	149.9064	-0.6653	-0.0275	0.5533
7	-46.4578	38.6558	6.9473	-1.4077	0.4717	-0.0058
	38.6558	5.3642	-1.2159	0.4717	1.3615	0.0048
	6.9473	-1.2159	122.7961	-0.0058	0.0048	0.0463
8	-68.2966	74.2076	2.0864	-0.2027	0.2539	0.0261
	74.2076	42.4975	-0.5454	0.2539	0.1756	0.0455
	2.0864	-0.5454	168.2294	0.0261	0.0455	0.0271
9	-66.7252	71.8776	1.4187	-0.5499	-1.2751	0.0552
	71.8776	40.2467	-0.3592	-1.2751	0.5467	-0.0285
	1.4187	-0.3592	164.8503	0.0552	-0.0285	0.0031
10	-65.4282	69.9249	1.418	-0.8473	0.3579	0.0155
	69.9249	38.6243	-0.3496	0.3579	0.5968	-0.0041
	1.418	-0.3496	161.7913	0.0155	-0.0041	0.2505

TABLE C.1: Paramagnetic and quadrupolar tensors of each site for ${}^7\text{Li}$ in $\text{Nd}_{58}\text{Li}_{25}\text{TiO}_3$ (sample 2) at $T=331$ K. Site numbers refer to labels used in Figure 4.13

Site Number	Paramagnetic Tensor (kHz)			Quadrupole Tensor (kHz)		
11	-63.7474	67.4156	0.6808	-5.2911	-1.5419	0.0372
	67.4156	36.1141	-0.1502	-1.5419	3.298	0.068
	0.6808	-0.1502	158.2592	0.0372	0.068	1.9931
12	-61.8484	64.6515	0.7559	0.8013	-0.2779	-0.673
	64.6515	33.2441	-0.182	-0.2779	-1.1476	0.0355
	0.7559	-0.182	154.3972	-0.673	0.0355	0.3463
13	-48.1915	41.8255	0.008	-2.8551	-0.3226	0.0393
	41.8255	8.501	-0.0208	-0.3226	2.3489	0.0125
	0.008	-0.0208	126.5971	0.0393	0.0125	0.5062
14	-46.8764	38.649	-0.2001	-0.6868	-0.4802	0.0846
	38.649	5.3224	0.0411	-0.4802	0.9086	-0.0052
	-0.2001	0.0411	123.3095	0.0846	-0.0052	-0.2218
15	-66.1808	73.8697	-21.6798	11.5203	5.4923	-0.0276
	73.8697	42.3343	5.6825	5.4923	11.7895	2.4024
	-21.6798	5.6825	166.0594	-0.0276	2.4024	-23.3098
16	-64.9633	71.6946	-19.4873	-2.6084	0.6299	0.0239
	71.6946	40.4118	5.04	0.6299	1.8322	-0.1986
	-19.4873	5.04	162.8484	0.0239	-0.1986	0.7762
17	-63.779	69.5619	-17.4099	1.5542	0.2706	-0.0184
	69.5619	38.3598	4.4279	0.2706	-0.2499	-0.6031
	-17.4099	4.4279	159.917	-0.0184	-0.6031	-1.3044
18	-62.2205	66.849	-15.1686	-0.7311	0.4494	0.0055
	66.849	35.4538	3.78	0.4494	0.7309	0.0087
	-15.1686	3.78	156.4804	0.0055	0.0087	0.0002
19	-49.1721	44.6916	-7.3488	-3.0839	-1.1491	0.7248
	44.6916	11.4514	1.298	-1.1491	2.2114	-0.8352
	-7.3488	1.298	129.3142	0.7248	-0.8352	0.8725
20	-47.8661	41.8489	-7.034	-2.5685	-1.2035	-0.0423
	41.8489	8.4671	1.2091	-1.2035	2.227	-0.0339
	-7.034	1.2091	126.3279	-0.0423	-0.0339	0.3415

TABLE C.2: Paramagnetic and quadrupolar tensors of each site for ${}^7\text{Li}$ in $\text{Nd}_{58}\text{Li}_{25}\text{TiO}_3$ (sample 2) at $T=331$ K. Site numbers refer to labels used in Figure 4.13

Site Number	Paramagnetic Tensor (kHz)			Quadrupole Tensor (kHz)		
21	-46.5251	38.8154	-6.9724	0.0002	-0.0201	-0.0009
	38.8154	5.5044	1.206	-0.0201	-0.0008	0.0013
	-6.9724	1.206	122.9836	-0.0009	0.0013	0.0006
22	-47.3721	94.7305	119.9224	0.0437	0.1353	-0.1558
	94.7305	46.9843	-36.5463	0.1353	0.3713	0.0233
	119.9224	-36.5463	198.2252	-0.1558	0.0233	-0.4151
23	-46.0803	94.2325	120.2638	-0.0719	0.0425	-0.1216
	94.2325	47.7037	-36.6417	0.0425	0.3477	0.0137
	120.2638	-36.6417	195.3656	-0.1216	0.0137	-0.2758
24	-46.3315	93.6455	118.2916	-0.1068	-0.0289	-0.0999
	93.6455	47.5876	-35.9566	-0.0289	0.3165	0.0076
	118.2916	-35.9566	194.0106	-0.0999	0.0076	-0.2097
25	-43.6816	92.5072	119.5395	-0.1283	-0.0428	-0.0864
	92.5072	48.4116	-36.3722	-0.0428	0.3074	0.0042
	119.5395	-36.3722	188.9755	-0.0864	0.0042	-0.1791
26	-42.5728	92.4343	120.2589	-0.1389	0.0108	-0.0853
	92.4343	49.4986	-36.5501	0.0108	0.3045	0.0026
	120.2589	-36.5501	186.7428	-0.0853	0.0026	-0.1656
27	-41.9493	91.6188	119.4063	-0.1267	0.1144	-0.0712
	91.6188	49.5775	-36.2616	0.1144	0.2809	0.001
	119.4063	-36.2616	184.3941	-0.0712	0.001	-0.1542
28	-39.77	90.6815	120.3594	-0.0912	-0.1428	-0.0812
	90.6815	50.147	-36.5806	-0.1428	0.265	0.0004
	120.3594	-36.5806	180.3805	-0.0812	0.0004	-0.1738

TABLE C.3: Paramagnetic and quadrupolar tensors of each site for ${}^7\text{Li}$ in $\text{Nd}_{.58}\text{Li}_{.25}\text{TiO}_3$ (sample 2) at $T=331$ K. Site numbers refer to labels used in Figure 4.13

Site	x,y,z		x+1.5		x-1.5		y+1.5	
	C_Q	η_Q	C_Q	η_Q	C_Q	η_Q	C_Q	η_Q
1	-0.7731	0.4739	2.6065	0.2128	2.6828	0.0731	0.2596	0.2419
2	-0.418	0.4013	2.0365	0.2121	2.5537	0.137	-0.2579	0.9913
3	0.3885	0.5899	-3.7394	0.9259	2.5162	0.1966	-0.4466	0.9392
4	-0.1368	0.4402	2.3141	0.73	2.5213	0.239	0.4027	0.5663
5	0.3973	0.1895	7.8384	0.3352	2.5222	0.2681	-0.5507	0.6848
6	-0.6248	0.1827	-3.1798	0.7279	2.5612	0.3096	0.2964	0.6872
7	-1.5066	0.9105	-3.3164	0.9028	-42.5732	0.2283	106.5561	0.0842
8	-0.5656	0.4973	1.9029	0.0518	1.7144	0.4411	-0.5573	0.0861
9	-3.5128	0.249	-4.2276	0.8184	-3.2236	0.9721	0.7115	0.3647
10	-0.9968	0.2902	1.6254	0.421	-18.235	0.5947	-0.5331	0.1961
11	-6.0581	0.2925	-6.5525	0.4058	-11.6192	0.6131	0.2663	0.1996
12	-0.7214	0.5508	-1.8587	0.7039	-21.2594	0.6	0.179	0.7647
13	-2.8349	0.603	3.6087	0.5134	-92.1308	0.0856	256.2769	0.0362
14	0.9891	0.6705	2.3604	0.6674	-27.5215	0.3456	-5.9837	0.0383
15	-23.55	0.2253	3.2672	0.9132	2.9845	0.4849	0.8497	0.0578
16	-2.736	0.3506	0.7218	0.2125	32.9568	0.8418	-1.0662	0.1808
17	2.5697	0.1863	-3.1016	0.4695	3.7879	0.3682	-0.6226	0.4925
18	-0.9441	0.1895	-1.1543	0.8609	29.0932	0.3109	-0.5042	0.5336
19	-3.1864	0.25	2.9582	0.0102	-6.7178	0.1829	-1.827	0.5416
20	-3.0688	0.699	2.6753	0.5625	-15.2556	0.7229	-5.6611	0.2164
21	-0.2485	0.3019	3.2638	0.6636	-6.8223	0.1406	1.4788	0.6679
22	-0.4343	0.5395	2.6137	0.0533	0.193	0.5221	0.2125	0.0191
23	-0.2368	0.9739	2.4994	0.1437	0.1877	0.3408	-0.2373	0.5968
24	0.1922	0.6083	2.4546	0.2052	0.1601	0.9747	0.316	0.9215
25	0.1936	0.2604	2.4578	0.2383	-0.1624	0.6961	0.347	0.9073
26	0.2084	0.1053	2.4595	0.2777	-0.1542	0.4636	0.3674	0.9477
27	0.1934	0.142	2.4974	0.3349	-0.1299	0.2776	0.4394	0.8865
28	1.0201	0.1933	2.3632	0.3912	-0.3998	0.4606	-0.4076	0.7141

TABLE C.4: principal values of the quadrupole tensors for each site of ${}^7\text{Li}$ in $\text{Nd}_{58}\text{Li}_{25}\text{TiO}_3$ (sample 2) with displacements of 1.5 \AA in various directions relative to the on-site positions (x,y,z). C_Q listed in kHz. Site numbers refer to labels used in Figure 4.13. Additional displacements given in Table C.5

Site	y-1.5		z+1.5		z-1.5	
	C_Q	η_Q	C_Q	η_Q	C_Q	η_Q
1	-0.2393	0.4373	2.495	0.0308	2.0522	0.0538
2	0.3795	0.9458	2.3911	0.187	0.9245	0.3862
3	0.3735	0.8922	2.3185	0.2863	1.7185	0.4721
4	0.3824	0.9131	2.3548	0.2978	-3.0336	0.2901
5	0.3851	0.9521	2.2839	0.3603	-2.1755	0.3164
6	106.8192	0.0019	2.0874	0.4796	-44.1186	0.0467
7	1.1091	0.3827	-3.7067	0.1621	-3.8801	0.3415
8	0.5951	0.1481	2.8549	0.237	1.2472	0.2473
9	-1.9683	0.1487	2.998	0.5879	3.0369	0.7826
10	-0.3391	0.8257	2.7096	0.4649	-1.8597	0.2242
11	-0.7507	0.8028	2.6611	0.7481	-1.2429	0.0763
12	106.664	0.0019	2.1816	0.6257	-9.3152	0.355
13	2.3744	0.3809	-0.4755	0.5655	3.8686	0.1307
14	1.1518	0.3138	-21.1232	0.7141	0.9991	0.0703
15	-5.3785	0.0045	3.3796	0.4795	2.9165	0.0897
16	-0.3839	0.7293	2.8117	0.5014	1.1079	0.6244
17	-1.3915	0.9224	2.9553	0.6839	0.9567	0.7885
18	0.283	0.5242	2.1829	0.6393	-0.5696	0.3413
19	2.0491	0.0852	1.7399	0.7065	-3.5756	0.2923
20	0.5183	0.7802	-10.1802	0.2015	1.9889	0.4763
21	-2.6474	0.7205	2.1134	0.1103	-37.2511	0.0189
22	-0.2163	0.3622	1.0691	0.1147	0.9746	0.2071
23	0.3008	0.9486	0.9913	0.162	0.8612	0.0665
24	0.3399	0.888	0.9598	0.3282	0.8195	0.2241
25	0.3628	0.9228	0.934	0.3565	0.7782	0.2634
26	0.3873	0.9549	0.925	0.3966	0.7513	0.2899
27	-0.394	0.7938	0.8669	0.3959	0.672	0.3473
28	-0.3884	0.5799	0.8495	0.4191	0.6857	0.1881

TABLE C.5: principal values of the quadrupole tensors for each site of ${}^7\text{Li}$ in $\text{Nd}_{.58}\text{Li}_{.25}\text{TiO}_3$ (sample 2) with displacements of 1.5 Å in various directions relative to the on-site positions (x,y,z). C_Q listed in kHz. Site numbers refer to labels used in Figure 4.13. Additional displacements given in Table C.4

APPENDIX D

Matlab Source Code

This appendix contains some of the Matlab™ source code used in order to calculate the paramagnetic and quadrupolar interaction tensors using a point-charge approximation, as well as the simulation of NMR line shapes based on those tensors.

D.1 Simulation of Paramagnetic & Quadrupolar FID for Spin-3/2 Nucleus

The following section of code takes in a structure with NMR parameters, including the experiment parameters and the various tensor components. It then returns a simulated free induction decay. This can then be processed to produce a frequency-domain spectrum using the processing routines already present in EXPRESS [8]. This function can be used stand-alone, or as a custom module in the EXPRESS program. This function is for a spin-3/2 system and takes into account paramagnetic and first-order quadrupolar interactions, such as ${}^7\text{Li}$. A separate routine, with minor variations, was used to simulate spin-1 (${}^6\text{Li}$) systems. This function can handle multiple sites, but will solve them independently. There are no dynamics taken into account.

```

function FID=paramag(param)
%Function for calculating FID of Spin-3/2 paramagnetic systems
%Assumes there are no dynamics between sites
%Started 6-11-08

sites = param.sites_total; %Total number of independent sites
cq = 2000*pi*param.cq(1:sites); %Cq values
eta = param.eta(1:sites); %Quadrupole asymmetry parameters
etacsa = param.etacsa(1:sites); %Paramagnetic tensor asymmetry
w0 = 2*pi*param.w0; %Larmor frequency
dsigcsa = w0*param.dsigcsa(1:sites);
    %Anisotropy of paramagnetic tensor
diso = w0*param.diso(1:sites); %Isotropic shift
sr = 2*pi*1000*param.sr; %Spin Rate
beta_r = param.beta_r; %MAS angle

weight = param.wts(1:sites); %relative weights of sites

AnglesQ = param.oneangle;
AnglesC = param.oneanglecsa;

actualBeta = 180*acos(sqrt(1/3))/pi;
beta = (beta_r+actualBeta)*pi/180; % back to radians...

dwell = param.time*1e-6; %Dwell time

FID = zeros(1, param.nfid);
nfid=param.nfid;

Pinfo = gettiles(param.n,param.tiletype);
    %Get tiles for powder increments

```

```

NAVG = size(Pinfo,1);

%Construct Wigner Rotation Matrices
d = wignersmall(beta);
dA = d';
DQ = wigner(AnglesQ(1:sites,:)); %Quadrupole frame to PAS
DC = wigner(AnglesC(1:sites,:)); %Paramagnetic frame to PAS
wq = (2*pi*cq/6);

Vc = 1/3*[dsigcsa' .* etacsa' zeros(sites,1)
          2*dsigcsa' .* ones(sites,1)
          zeros(sites,1) dsigcsa' .* etacsa'] * DC;
          %Paramagnetic terms in PAS frame

Vq = [wq' .* eta' / 2 zeros(sites,1)
       sqrt(3/2) * wq' .* ones(sites,1)
       zeros(sites,1) wq' .* eta' / 2] * DQ; %Quadrupole terms

R2 = 0 * pi * 300;
      %Used to artificially add T2 decay to the resulting FID

for powIndex=1:NAVG
    D=wigner(Pinfo(powIndex,1:3));

    R2KR1 = ((-Vc-sqrt(6)*Vq)*D) .* [dA(3,1)*ones(sites,1)
                                     dA(3,2)*ones(sites,1)
                                     dA(3,3)*ones(sites,1) dA(3,4)*ones(sites,1)
                                     dA(3,5)*ones(sites,1)]; %1-2 transition

    R2KR2 = (-Vc*D) .* [dA(3,1)*ones(sites,1)
                       dA(3,2)*ones(sites,1)

```

```

        dA(3,3)*ones(sites,1) dA(3,4)*ones(sites,1)
        dA(3,5)*ones(sites,1)]; %2-3 transition

R2KR3 = ((-Vc+sqrt(6)*Vq)*D) .*[dA(3,1)*ones(sites,1)
        dA(3,2)*ones(sites,1)
        dA(3,3)*ones(sites,1) dA(3,4)*ones(sites,1)
        dA(3,5)*ones(sites,1)]; %3-4 transition

[ta,ya] = ode45(@dydtA,linspace(0,nfid*dwell,nfid+1),
        ones(sites,1));
[tb,yb] = ode45(@dydtB,linspace(0,nfid*dwell,nfid+1),
        ones(sites,1));
[tc,yc] = ode45(@dydtC,linspace(0,nfid*dwell,nfid+1),
        ones(sites,1));

for j=1:nfid
    for k=1:sites
        FID(j)=FID(j)+(weight(k)*(3*ya(j,k)+
            4*yb(j,k)+3*yc(j,k)))*
            Pinfo(powIndex,4);
    end;
end

end %Powder loop

FID = FID(:) ;
%This ensures a column vector, required for proper post-processing

%=====
function dydtA = dydtA(t,y) %1-2 Transition
    R = R2KR1(:,1)*exp(-2*i*sr*t)+R2KR1(:,5)*exp(2*i*sr*t)+
        R2KR1(:,2)*exp(-1*i*sr*t)+

```

```

        R2KR1(:,4)*exp(1*i*sr*t)+R2KR1(:,3);
dydtA = i*(diso'+R).*y-R2.*y;
end
%=====
function dydtB = dydtB(t,y) %2-3 Transition (Central Transition)
    R = R2KR2(:,1)*exp(-2*i*sr*t)+R2KR2(:,5)*exp(2*i*sr*t)+
        R2KR2(:,2)*exp(-1*i*sr*t)+
        R2KR2(:,4)*exp(1*i*sr*t)+R2KR2(:,3);
    dydtB = i*(diso'+R).*y-R2.*y;
end
%=====
function dydtC = dydtC(t,y) %3-4 Transition
    R = R2KR3(:,1)*exp(-2*i*sr*t)+R2KR3(:,5)*exp(2*i*sr*t)+
        R2KR3(:,2)*exp(-1*i*sr*t)+
        R2KR3(:,4)*exp(1*i*sr*t)+R2KR3(:,3);
    dydtC = i*(diso'+R).*y-R2.*y;
end

end

```

D.2 Calculation of EFG at a Site Due to One Nucleus

This function determines the contribution to the electric field gradient at a specified x, y, z coordinate due to a single charge.

```

function EFG = EFGinteraction(x, y, z, Site)
%calculates the paramagnetic tensor interaction between
%'x, y, z' and 'Site'
%Site structure contains: x, y, z, charge, nucleus, spin, label

```

```

%position information should be in angstrom to start

T=zeros(3,3);

%Conversion from angstroms to meters is held until end
%to avoid Matlab floating point errors
dx = (x-Site.x);
dy = (y-Site.y);
dz = (z-Site.z);

r = sqrt(dx^2 + dy^2 + dz^2);

h = 6.626e-34; %Planck's constant (kg*M^2/s)
Q = -4.01e-30; %Quadrupole moment of Li7 (m^2)
e0 = 8.85419e-12; %epsilon-0 (F/m)
e = 1.60e-19; %electron charge (C)

C = r^(-2)*Site.charge*e/(4*pi*e0)*r^(-1); %(V/m^2)

T(1,1) = C*(dy^2 + dz^2 - 2*dx^2)*r^(-2);
T(1,2) = C*(-3*dx*dy)*r^(-2);
T(1,3) = C*(-3*dx*dz)*r^(-2);
T(2,1) = C*(T(1,2))*r^(-2);
T(2,2) = C*(dx^2 + dz^2 - 2*dy^2)*r^(-2);
T(2,3) = C*(-3*dy*dz)*r^(-2);
T(3,1) = C*(T(1,3))*r^(-2);
T(3,2) = C*(T(2,3))*r^(-2);
T(3,3) = C*(dx^2 + dy^2 - 2*dz^2)*r^(-2);

T = T*(e*Q/(h))/1000*10^(30); % (kHz)

```

```
EFG=T;
```

D.3 Calculation of Complete EFG Tensor

This function uses the previous one to determine the EFG tensor due to all nearby charges.

```
function EFG = CalcEFG(x, y, z, Sites, Range)
%Calculates the Electric Field Gradient tensor at location "x, y, z"
%nucleus 'Center' and all 'Sites' (excluding 'Center') no farther than
%'Range' away
%Site structure contains: x, y, z, charge, nucleus, spin, label

T = zeros(3,3); %Running total of EFG-tensor

TotalSites = length(Sites);

MaxR=1000000; %Maximum distance to be included in calculation
           %Set high just to makes sure everything is included
MinR=0.05; %Minimum distance to be included in calculation
           %To avoid counting interaction between an atom and itself
Flag=0; %=1 if site is to be ignored for whatever reason

Occupancy = 0.2947; %Occupancy of Sample 2 for Nd in mixed layer

for ii = 1:TotalSites

    Skip=0;
```



```
TempSite=Sites(ii);

%Find distance between Center and Site-ii
dx = TempSite.x - x;
dy = TempSite.y - y;
dz = TempSite.z - z;
r = sqrt(dx^2 + dy^2 + dz^2);

Dice=rand;

%"class" groups the Nd depending on whether they are
%partially occupied or not
if (TempSite.class==2 || TempSite.class==3)
    if Dice>Occupancy %Occupancy rate of site
        Skip = 1;
    end;
end;

if (r>MinR && r<=Range && Flag==0 && Skip==0)
    Ttemp = EFGinteraction(x, y, z,TempSite);
    T = T + Ttemp;
end;

end;

EFG = T;
```

D.4 Calculation of Paramagnetic Tensor Due to a Single Nucleus

This function works similarly to the single-site EFG calculation. It determines the contribution to the overall P-tensor due to a single nucleus. The function to calculate the total P-tensor for a given site is done similarly to the method used for the EFG tensor.

```
function P = interaction(Center, Site)
%calculates the paramagnetic tensor between 'Center' and 'Site'
%Site structure contains: x, y, z, charge, nucleus, spin, label

Para=zeros(3,3);

%g-tensor principle components:
%Real values are used outside this function
%so they can be varied later
%without needing to recalculate the entire tensor
xx = 1;
yy = 1;
zz = 1;

Beta = 9.274009e-24; % J/T
k = 1.38065e-23; % J/K
T = 300; % K
Spin=Site.spin;
%C=(Beta^2*Spin*(Spin+1))/(3*k*T);
C=1; %C is scaled outside this function

dx = Site.x - Center.x;
```

```

dy = Site.y - Center.y;
dz = Site.z - Center.z;

%Convert to spherical coordinates (with 'Center' as origin)
r = sqrt(dx^2 + dy^2 + dz^2);
S = sqrt(dx^2 + dy^2);
eta = acos(dz/r);
if r<0
    phi=pi - asin(dy/sqrt(S));
else
    phi=asin(dy/S);
end

Para(1,1) = xx^2 * (1 - 3 * sin(eta)^2 * cos(phi)^2) * (C/r^3);
Para(1,2) = xx^2 * (-3 * sin(eta)^2 * cos(phi) * sin(phi)) * (C/r^3);
Para(1,3) = xx^2 * (-3 * sin(eta) * cos(eta) * cos(phi)) * (C/r^3);
Para(2,1) = yy^2 * (-3 * sin(eta)^2 * cos(phi) * sin(phi)) * (C/r^3);
Para(2,2) = yy^2 * (1 - 3 * sin(eta)^2 * sin(phi)^2) * (C/r^3);
Para(2,3) = yy^2 * (-3 * sin(eta) * cos(eta) * sin(phi)) * (C/r^3);
Para(3,1) = zz^2 * (-3 * sin(eta) * cos(eta) * cos(phi)) * (C/r^3);
Para(3,2) = zz^2 * (-3 * sin(eta) * cos(eta) * sin(phi)) * (C/r^3);
Para(3,3) = zz^2 * (1 - 3 * cos(eta)^2) * (C/r^3);

P=Para;

```

BIBLIOGRAPHY

- [1] B. S. Guiton and P. K. Davies, "Nano-chessboard superlattices formed by spontaneous phase separation in oxides," *Nature Materials*, vol. 6, pp. 586–591, June 2007.
- [2] B. Guiton, H. Wu, and P. Davies, "Neutron powder diffraction of $(\text{Nd}_{7/12}\text{Li}_{1/4})\text{TiO}_3$ nano-checkerboard superlattices," *Chemistry of Materials*, vol. 20, no. 9, pp. 2860–2862, 2008.
- [3] P. Davies, A. Borisevich, and M. Thirumal, "Communicating with wireless perovskites: Cation order and zinc volatilization," *Journal of the European Ceramic Society*, vol. 23, no. 14, pp. 2461–2466, 2003.
- [4] A. Borisevich and P. Davies, " $\text{La}(\text{Li}_{1/3}\text{Ti}_{2/3})\text{O}_3$: a new 1: 2 ordered perovskite," *Journal of Solid State Chemistry*, vol. 170, no. 1, pp. 198–201, 2003.
- [5] A. Borisevich and P. Davies, "1: 2 cation order in a $(\text{Li}_{1/3}(\text{Nb}, \text{Ta})_{2/3})\text{O}_3$ microwave perovskites," *Applied physics letters*, vol. 84, no. 8, pp. 1347–1349, 2004.
- [6] J. Grutzner, K. Stewart, R. Wasylishen, M. Lumsden, C. Dybowski, and P. Beckmann, "A new mechanism for spin-lattice relaxation of heavy nuclei in the solid state: ^{207}Pb relaxation in lead nitrate," *Journal of the American Chemical Society*, vol. 123, no. 29, pp. 7094–7100, 2001.
- [7] P. J. de Castro, C. A. Maher, R. L. Vold, and G. L. Hoatson, "High field ^{207}Pb spin-lattice relaxation in solid lead nitrate and lead molybdate," *J. Chem. Phys.*, vol. 128, June 2008.
- [8] R. Vold and G. Hoatson, "Effects of jump dynamics on solid state nuclear magnetic resonance line shapes and spin relaxation times," *Journal of Magnetic Resonance*, vol. 198, no. 1, pp. 57–72, 2009.
- [9] M. J. Duer, *Introduction to Solid-State NMR Spectroscopy*. Oxford, UK: Blackwell Publishing, 2004.
- [10] J. Amoureux, C. Fernandez, and L. Frydman, "Optimized multiple-quantum magic-angle spinning nmr experiments on half-integer quadrupoles," *Chemical physics letters*, vol. 259, no. 3-4, pp. 347–355, 1996.

- [11] Z. Gan, "Satellite transition magic-angle spinning nuclear magnetic resonance spectroscopy of half-integer quadrupolar nuclei," *The Journal of Chemical Physics*, vol. 114, p. 10845, 2001.
- [12] A. Abragam, *Principles of Nuclear Magnetism*. USA: Oxford University Press, 1983.
- [13] C. P. Slichter, *Principles of Magnetic Resonance*. Springer-Verlag, 1990.
- [14] R. Ernst and W. Anderson, "Application of fourier transform spectroscopy to magnetic resonance," *Review of Scientific Instruments*, vol. 37, no. 1, pp. 93–102, 1966.
- [15] A. Schmidt and S. Vega, "The floquet theory of nuclear magnetic resonance spectroscopy of single spins and dipolar coupled spin pairs in rotating solids," *The Journal of chemical physics*, vol. 96, p. 2655, 1992.
- [16] E. Andrew, "Magic angle spinning in solid state nmr spectroscopy," *Philosophical Transactions of the Royal Society of London. Series A, Mathematical and Physical Sciences*, vol. 299, no. 1452, p. 505, 1981.
- [17] J. Herzfeld and A. Berger, "Sideband intensities in nmr spectra of samples spinning at the magic angle," *The Journal of Chemical Physics*, vol. 73, p. 6021, 1980.
- [18] U. Haeberlen, *High resolution NMR in solids: selective averaging*, vol. 1. Academic Press New York, 1976.
- [19] R. Harris, E. Becker, S. de Menezes, R. Goodfellow, and P. Granger, "Nmr nomenclature. nuclear spin properties and conventions for chemical shifts:(iupac recommendations 2001)," *Pure and applied chemistry*, vol. 73, no. 11, pp. 1795–1818, 2001.
- [20] O. Dmitrenko, S. Bai, P. Beckmann, S. van Bramer, A. Vega, and C. Dybowski, "The relationship between ^{207}Pb nmr chemical shift and solid-state structure in Pb (ii) compounds," *The Journal of Physical Chemistry A*, vol. 112, no. 14, pp. 3046–3052, 2008.
- [21] A. Nayeem and J. Yesinowski, "Calculation of magic-angle spinning nuclear magnetic resonance spectra of paramagnetic solids," *J. Chem. Phys.*, vol. 89, 1988.
- [22] N. Bloembergen, "Fine structure of the magnetic resonance line of protons in $\text{CuSO}_4 \cdot 5\text{H}_2\text{O}$," *Physica*, vol. 19, pp. 95–112, February 1950.
- [23] D. Mao, E. Walter, H. Krakauer, and Z. Wu, "Structural dependence of electric field gradients in $\text{Pb}(\text{Zr}_{1-x}\text{Ti}_x)_2\text{O}_7$ from first principles," *Physical Review B*, vol. 76, no. 1, p. 014105, 2007.
- [24] E. Fukushima and S. Roeder, *Experimental pulse NMR: a nuts and bolts approach*. Addison-Wesley Pub. Co., Advanced Book Program, 1981.

- [25] E. L. Hahn and D. E. Maxwell, "Spin echo measurements of nuclear spin coupling in molecules," *Phys. Rev.*, vol. 88, pp. 1070–1084, Dec 1952.
- [26] S. Meiboom and D. Gill, "Modified spin-echo method for measuring nuclear relaxation times," *Review of Scientific Instruments*, vol. 29, no. 8, pp. 688–691, 1958.
- [27] M. Maricq and J. Waugh, "Nmr in rotating solids," *The Journal of Chemical Physics*, vol. 70, p. 3300, 1979.
- [28] L. Cahill, R. Chapman, C. Kirby, and G. Goward, "The challenge of paramagnetism in two-dimensional 6, 7 Li exchange nmr," *Applied Magnetic Resonance*, vol. 32, no. 4, pp. 565–581, 2007.
- [29] B. Biospin, 2009. Private Communication.
- [30] C. Joseph, G. Varghese, and M. Ittyachen, "Magnetic moment and susceptibility measurements of mixed rare earth oxalate crystals," *Crystal Research and Technology*, vol. 31, no. 1, pp. 127–130, 1996.
- [31] J. Lock, "The magnetic susceptibilities of lanthanum, cerium, praseodymium, neodymium and samarium, from 1.5 k to 300 k," *Proceedings of the Physical Society. Section B*, vol. 70, p. 566, 1957.
- [32] D. Brink and G. Satchler, *Angular momentum*. Clarendon Press Oxford, 1962.
- [33] C. Pickard and F. Mauri, "All-electron magnetic response with pseudopotentials: Nmr chemical shifts," *Physical Review B*, vol. 63, no. 24, p. 245101, 2001.
- [34] O. Andersen, "Linear methods in band theory," *Physical Review B*, vol. 12, no. 8, p. 3060, 1975.
- [35] R. Elliott and K. Stevens, "The magnetic properties of certain rare-earth ethyl sulphates," *Proceedings of the Royal Society of London. Series A. Mathematical and Physical Sciences*, vol. 219, no. 1138, p. 387, 1953.
- [36] J. Daniels, "The effect of interactions in a paramagnetic on the entropy and susceptibility," *Proceedings of the Physical Society. Section A*, vol. 66, p. 673, 1953.
- [37] M. Sommariva and M. Catti, "Neutron diffraction study of quenched $\text{Li}_{0.3}\text{La}_{0.567}\text{TiO}_3$ lithium ion conducting perovskite," *Chemistry of materials*, vol. 18, no. 9, pp. 2411–2417, 2006.
- [38] R. Vold, G. Hoatson, L. Vugmeyster, D. Ostrovsky, and P. De Castro, "Solid state deuteron relaxation time anisotropy measured with multiple echo acquisition," *Physical Chemistry Chemical Physics*, vol. 11, no. 32, pp. 7008–7012, 2009.
- [39] L. Mueller, "Tensors and rotations in nmr," *Concepts in Magnetic Resonance Part A*, vol. 38, no. 5, pp. 221–235, 2011.

- [40] D. L. Pechkis, G. Hoatson, and R. L. Vold, "⁷Li and ⁹³Nb spectroscopy of high dielectric perovskite polycrystalline materials." Presented as a poster at Experimental NMR Conference (ENC), *.
- [41] S. Ashbrook and S. Wimperis, "Satellite-transition mas nmr of spin $i=3/2, 5/2, 7/2,$ and $9/2$ nuclei: sensitivity, resolution, and practical implementation," *Journal of Magnetic Resonance*, vol. 156, no. 2, pp. 269–281, 2002.
- [42] Z. Gan, "Isotropic nmr spectra of half-integer quadrupolar nuclei using satellite transitions and magic-angle spinning," *Journal of the American Chemical Society*, vol. 122, no. 13, pp. 3242–3243, 2000.
- [43] J. Trebosc, J. Amoureux, and Z. Gan, "Comparison of high-resolution solid-state nmr mpmas and stmas methods for half-integer quadrupolar nuclei," *Solid State Nuclear Magnetic Resonance*, vol. 31, no. 1, pp. 1–9, 2007.
- [44] D. Zhou, *Multinuclear NMR Studies of Relaxor Ferroelectrics*. PhD thesis, The College of William and Mary, 2003.
- [45] I. Hung, J. Trébosc, G. Hoatson, R. Vold, J. Amoureux, and Z. Gan, "Q-shear transformation for mpmas and stmas nmr spectra," *Journal of Magnetic Resonance*, vol. 201, no. 1, pp. 81–86, 2009.
- [46] H. Boysen and F. Altorfer, "A neutron powder investigation of the high-temperature structure and phase transition in *LiNbO₃*," *Acta Crystallographica Section B: Structural Science*, vol. 50, no. 4, pp. 405–414, 1994.
- [47] E. Wimmer, H. Krakauer, M. Weinert, and A. Freeman, "Full-potential self-consistent linearized-augmented-plane-wave method for calculating the electronic structure of molecules and surfaces: O₂ molecule," *Physical Review B*, vol. 24, no. 2, p. 864, 1981.
- [48] W. Barton and J. Cashion, "Electric-field gradients in ionic gadolinium compounds," *Journal of Physics C: Solid State Physics*, vol. 12, p. 2897, 1979.
- [49] D. Spearing, "ptchg: a fortran program for point-charge calculations of electric field gradients (efgs)," *Computers & Geosciences*, vol. 20, no. 4, pp. 615–624, 1994.
- [50] P. Beckmann and C. Dybowski, "A thermometer for nonspinning solid-state nmr spectroscopy," *Journal of Magnetic Resonance*, vol. 146, no. 2, pp. 379–380, 2000.

VITA

Christopher Andrew Maher

Christopher Andrew Maher was born on September 13, 1982 in Portsmouth, New Hampshire. He received his B.S. in Physics, along with a minor in Computer Science, from the University of New Hampshire in 2005. He then obtained an M.S. in Physics from the College of William and Mary in 2007, followed by a Ph.D. in physics in January of 2012.